DIGITAL RESTORATION OF DISPERSION-DEGRADED IMAGES FROM A LIQUID CRYSTAL OPTICAL PHASED ARRAY

Thesis

Submitted to

Graduate Engineering & Research

School of Engineering

UNIVERSITY OF DAYTON

In Partial Fulfillment of the Requirements for

The Degree

Master of Science in Electro-Optics

by

Ronald James Broessel

UNIVERSITY OF DAYTON

Dayton, Ohio

August 1995

UNIVERSITY OF DAYTON ROESCH LIBRARY

:SIS

96 02999

DIGITAL RESTORATION OF DISPERSION-DEGRADED IMAGES FROM A LIQUID CRYSTAL OPTICAL PHASED ARRAY

Approved by:

Vince Dominic, Ph.D.
Assistant Professor
Advisory Committee, Chairperson

Russell C. Hardie, Ph.D.
Assistant Professor
Advisory Committee, Member

Edward A. Watson, Ph.D.
Senior Scientist
Advisory Committee, Member

Donald L. Moon, Ph.D.
Associate Dean
Graduate Engineering Programs
and Research
School of Engineering

Joseph Lestingi, D. Eng., P.E.
Dean
School of Engineering

ABSTRACT

DIGITAL RESTORATION OF DISPERSION-DEGRADED IMAGES FROM A LIQUID CRYSTAL OPTICAL PHASED ARRAY

Name: Broessel, Ronald James
University of Dayton

Advisor: Dr. Vince Dominic

Liquid crystal arrays represent one of the first practical technologies capable of steering light by electronic control only. Such devices are used to non-mechanically steer the field of view of a broadband imaging sensor. Unfortunately, dispersion degrades the image quality by smearing out details in the image and by introducing multiple diffraction orders (echoes) at the detector plane. Methods are presented to compensate for these unwanted effects and thus digitally restore and enhance the broadband images obtained with the beam steerer. The Beam-Propagation Method (*BPM*) is used to find the wavelength-dependent impulse response from which the appropriate Wiener filter coefficients are derived. When training data is available, filter coefficients are improved with the adaptive Least Mean Square (*LMS*) algorithm. Restored images are presented that demonstrate the capabilities of this technique as a function of changing steering conditions including bandwidth (or wavelength) and steer angle. The ability of the filtering algorithms to restore images captured

with slight changes in bandwidth and blackbody emission characteristics, as compared to the original training data, is also demonstrated. Several different error measurements are employed to determine level of enhancement.

ACKNOWLEDGMENTS

My deepest thanks go to my faculty advisor, Dr. Vince Dominic, for his motivation and inspiration and for showing me that quality of research is more important than quantity. I would also like to thank the other members of my thesis committee, Dr. Russ Hardie and Dr. Ed Watson, for their instructive guidance and for providing a variety of useful insights to the problems investigated in this thesis. My thanks to Larry Barnes for his assistance in the lab and for answering enough technical questions to qualify him for Electro-optics Jeopardy. I greatly appreciate the management of USAF Wright Laboratory and Technology/Scientific Services, Inc., and Dr. Mohammad Karim for providing an excellent learning environment which made this research possible. This work was performed under Air Force contract number F33601-95-D-J010.

Special thanks also go to the Department of Physics and Astronomy faculty at the University of Wisconsin - Eau Claire for providing me with the technical knowledge and skills necessary to choose any path I desired.

This work is dedicated to my family and to my fiancée for their love and support which had to reach over many a mile.

TABLE OF CONTENTS

LIST OF FIGURES

LIST OF TABLES

CHAPTER 1

Introduction

Optical beam steering has many interesting industrial and military applications including laser radar systems, laser beam scanning, pointing stabilization, microscanning, *etc.*[1-5] Mechanical beam steering technology (based on mirrors) allows rapid, large-angle deflection and scanning of optical beams but fails to meet some of the higher resolution performance requirements for steering large diameter diffraction-limited laser radar beams.[1,5,6] Typical mechanical systems used today perform steering/scanning in the range of milliradians with steering accuracy in microradians. Beam steering devices using liquid crystal technology have been developed which can steer in the microradian range with nanoradian accuracy.[7] These devices represent one of the first practical technologies capable of providing accurate, agile, and inertialess beam steering using electronic control only. Such devices eliminate the need for bulky, complex mechanical systems thus reducing weight and increasing reliability. The liquid-crystal beam steerer borrows microwave radar

concepts to implement random access, non-mechanical beam steering with optical phased arrays.[8]

1.1 Background

A nematic liquid crystal beam steering device provides a linearly increasing optical phase delay (*OPD*) across its aperture, thus steering light just like a prism. The outgoing beam tilts because its phase front is advanced on one side of the aperture and delayed on the opposite side. In a nematic liquid-crystal beam steerer the *OPD* is controlled by an applied electric field which realigns birefringent liquid crystals. A typical liquid crystal steering cell consists of two transparent substrates and a 1 to 50 μm thick layer of E7 nematic liquid crystal, the thickness depending on the wavelength of incident light λ. The layer must be thick enough to allow a given incident wavelength to experience at least a 2π phase shift propagating through it. The substrates are initially prepared to give preferential alignment to the molecules next to the surface, which then aligns the entire cell volume. The surface of one substrate, typically indium tin oxide[7], is photolithographically patterned with transparent, conducting, striped electrodes, spaced at the desired phase shifter array positions. The other substrate is coated with a uniform transparent ground plate. Applying a voltage between an electrode and the ground plate creates a single phase shifter in the liquid crystal volume (shown in Figure 1.1).

In the absence of an applied voltage, an input optical beam polarized parallel to the plane of incidence sees the maximum index of refraction n_e, or the extraordinary index of the liquid crystal molecules. When the voltage applied to an electrode exceeds the threshold voltage, the cigar-shaped molecules will begin to rotate, partially aligning themselves with the applied field and reducing the effective index of refraction. Once the saturation voltage is reached, the input beam will see a minimum index of refraction, which is approximately equal to n_o, or the ordinary index of refraction. By altering the voltage applied to a series of electrodes, the spatial variation of the *OPD* can be manipulated. Monotonically

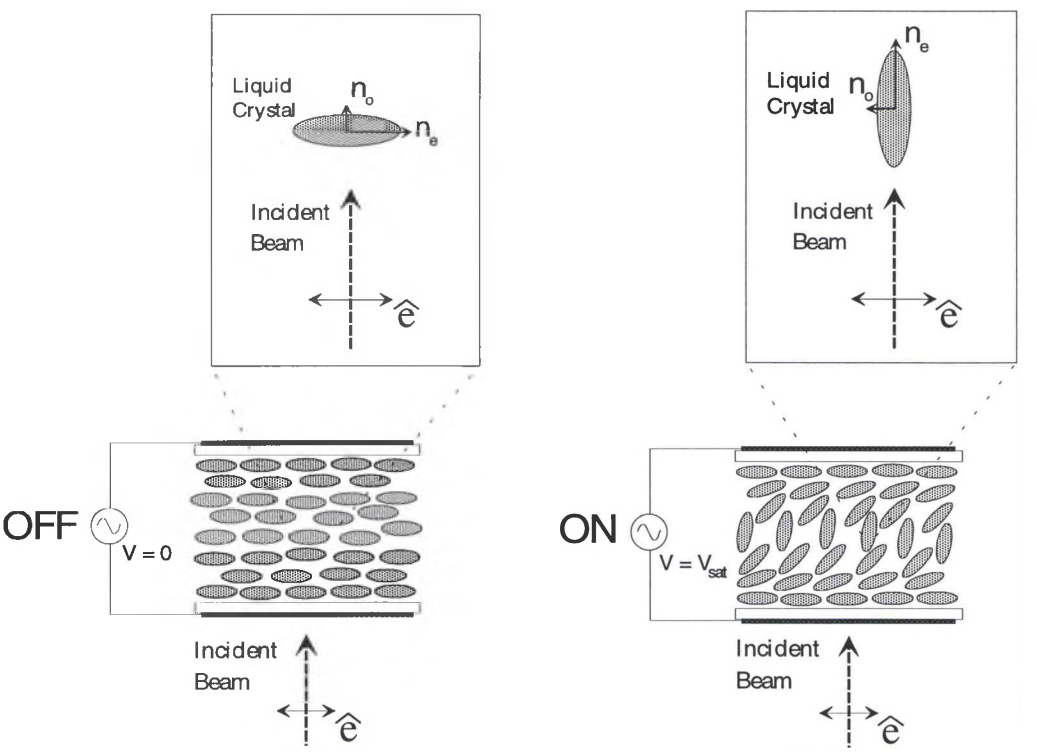

Figure 1.1) *Liquid crystal alignment for a single phase shifter element, (Left) zero applied voltage and (Right) saturation voltage applied. Here $\hat{e}$ denotes the optical polarization vector.* ***Note:*** *The crystal molecules located next to the substrate surface are shown to remain unaffected by the applied voltage because of surface tension.*

increasing the voltages across the device aperture (Figure 1.2) creates a phase profile resembling that of a prism. For a prism, the thickness T varies linearly across the aperture (direction x) yielding

$$OPD(x) = \frac{2\pi}{\lambda} n\,\delta T(x) , \tag{1.1}$$

where $\delta T(x)$ is the varying thickness. For the liquid crystal beam steerer the differential refractive index $\delta n(x) = n_e - n(x)$ varies linearly across the aperture yielding

$$OPD(x,\lambda) = \frac{2\pi}{\lambda} \delta n(x)\, T , \tag{1.2}$$

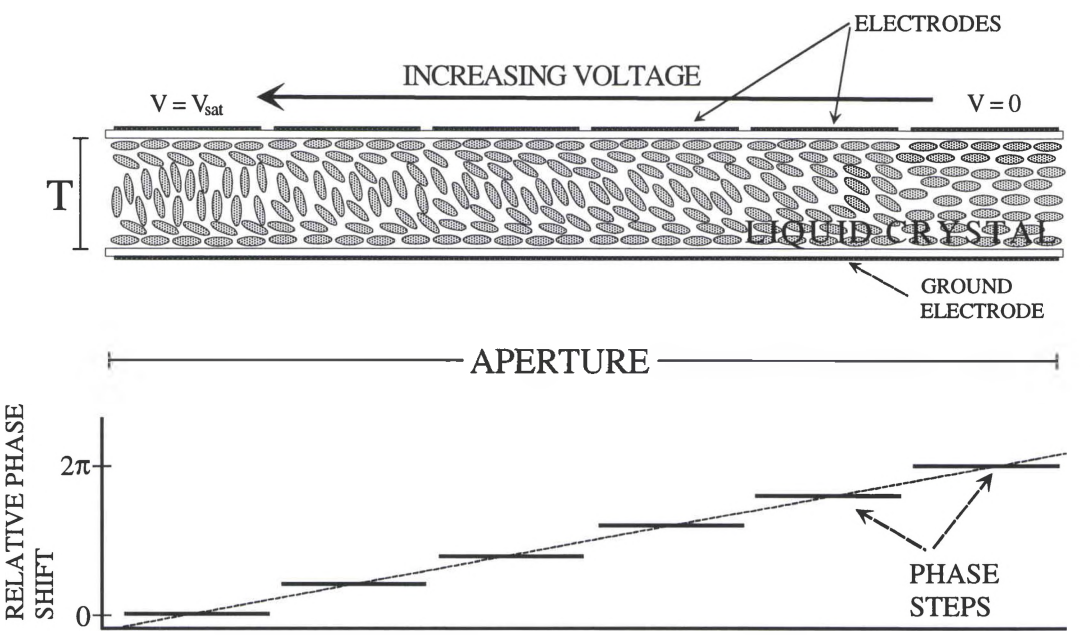

Figure 1.2) *Example of a multiple phase shifting element liquid crystal cell used to create a linearly increasing phase profile. The crystal molecules located next to the substrate surface are shown to remain unaffected by the applied voltage because of surface tension. (The identical effect is seen in Figure 1.1).*

where $n(x)$ is described by:

$$\frac{1}{n^2(\theta(x))} = \frac{\cos^2(\theta(x))}{n_o^2} + \frac{\sin^2(\theta(x))}{n_e^2} \quad . \tag{1.2a}$$

Here θ is the angle between the propagation direction of the incident optical beam and the director of the liquid crystal molecule. The dependence of θ on x can be seen in Fig. 1.2, where the rotation of the crystal molecules varies across the aperture. The differential index δn varies nonlinearly with the control voltage[9] and is at most equal to the birefringence Δn of the liquid crystal ($\cong 0.2$ in the mid-visible for E7).[10]

A prism-like phase profile steers all the incident energy at the design wavelength λ_{design} to the desired angle. However, as the wavelength shifts away from λ_{design} the steering angle of a prism changes according to

$$\theta_{\lambda_{probe}} = \theta_{\lambda_{design}} \frac{\Delta n(\lambda_{probe})}{\Delta n(\lambda_{design})} \quad , \tag{1.3}$$

for small steering angles. Material dispersion thus alters the steering angle for wavelengths other than λ_{design}. The material dispersion is described by

$$\Delta n(\lambda(nm)) = G\frac{\lambda^2\lambda_*^2}{\lambda^2 - \lambda_*^2} \quad , \tag{1.4}$$

where G = 3.06×10^{-6} and $\lambda_* = 250$ nm for the E7 liquid crystals in the device[10]. This equation is valid for wavelengths from the visible out through the near IR. For the mid to far IR wavelengths the equation reduces to ($\lambda >> \lambda_*$)

$$\Delta n = G\lambda_*^2 . \qquad (1.4a)$$

Unfortunately, devices with the prism-like *OPD* profiles shown in Figure 1.3(a) cannot be used because they are too thick and therefore too slow. For example, to steer 5 μm light to 0.024° using a linearly increasing phase ramp across an entire 4 cm device aperture requires a crystal layer ≅ 112 μm thick. Since the liquid-crystal re-alignment time t_R is proportional to the square of the layer thickness T[8,10,11]

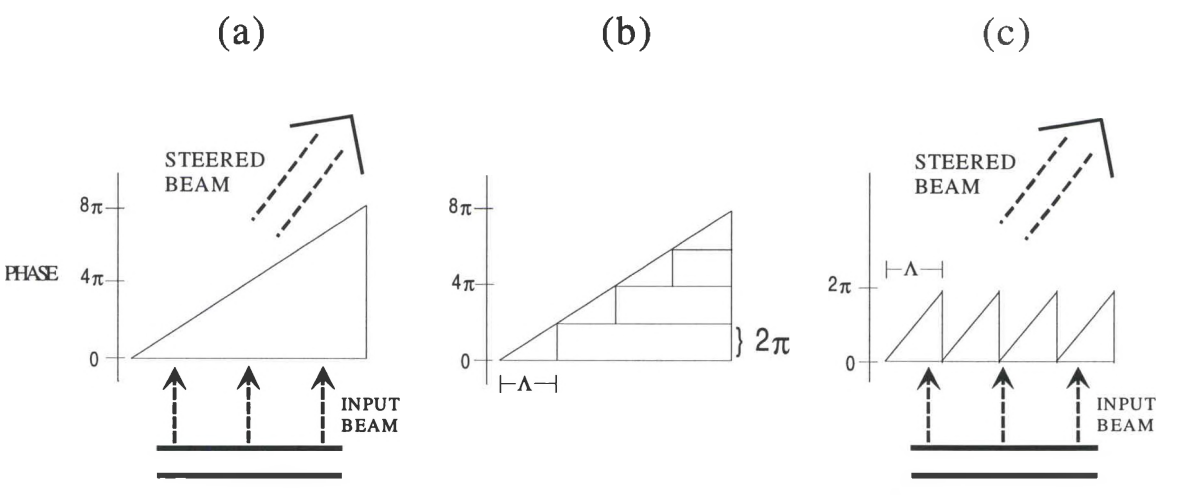

Figure 1.3) *Phase profile of beam steering device: (a) full prism-like phase across aperture, (b) decomposition of phase by removal of 2π phase steps, (c) resulting phase ramps resemble that of a blazed diffraction grating.*

$$t_R = \frac{\gamma_1 T^2}{K_{11}\pi^2}, \tag{1.5}$$

where γ_1 is the rotational viscosity and K_{11} is the corresponding elastic constant, such a device would have a re-alignment time of approximately 1.21 sec, making it impractically slow for laser radar applications.[1-3,5] A typical value for the ratio of γ_1/K_{11} for E7 liquid crystal is given by Wu[10] to be ≅ 0.949 ms(μm)$^{-2}$. The thickness of the liquid-crystal layer is greatly reduced by subtracting out regions of 2π phase from the original profile. Multiples of 2π are indistinguishable and do not affect the propagation of the beam at the design wavelength. The new phase profile resembles a blazed diffraction grating, seen in Figure 1.3(c). This phase-reset profile reduces the thickness of the crystal layer to ≅ 7 μm which gives reasonably fast switching times of 4-5 ms. One of the first devices demonstrated achieved a switching speed of approximately 2 ms for a 4 μm thick layer of liquid crystal.[7] A thinner device also allows higher spatial resolution in electrode addressing which reduces the effects of fringing fields, increasing the device steering efficiency.[7] Unfortunately the phase structure described above significantly degrades steered wavelengths which do not experience a 2π phase shift.

1.2 Broad-band Imaging Problem

The diffraction-grating nature of the phase profile introduces trouble when steering broadband radiation because the 2π phase resets are correct at only one wavelength.[1-3,5] Wavelengths other than λ_{design} have an incorrect phase shift ($\neq 2\pi$) at the resets. The resultant grating dispersion produces a smeared and echoed version of the original scene at the detector plane due to both the multiple grating orders (m in Eqn. 1.6) and wavelength-dependent smearing (λ in Eqn. 1.6) related by

$$\sin\theta = m\frac{\lambda}{\Lambda}, \tag{1.6}$$

where Λ is the phase ramp reset distance or ramp period and θ is the steer angle.

The grating orders and smearing effects can also be demonstrated by an analytical model of the beam steering device. The transmission function of a 1-D device can be expressed by the following:[2]

$$T(x) = \left[b(x) * \frac{1}{\Lambda} comb\left(\frac{x}{\Lambda}\right) \right] a\left(\frac{x}{W}\right), \tag{1.7}$$

where $b(x)$ is the blaze profile across a single ramp (period) and $a(x/W)$ describes the aperture, or size of the beam steerer. The comb function is described by:[5,12]

$$comb(x) = \sum_{n=-\infty}^{\infty} \delta(x-n) \ . \tag{1.7a}$$

The transmitted field can now be described using Fraunhofer diffraction theory, which is valid in this case since the device-to-detector plane distance z is, in general, large enough to satisfy the following condition:[12,13]

$$z >> \frac{k(W/2)^2_{\max}}{2} \ , \tag{1.8}$$

where W is the width of the device aperture and $k = 2\pi/\lambda$ is the magnitude of the wave vector in air. Assuming an incident plane wave, the field at the detector can be described by the Fraunhofer diffraction equation:[12,13]

$$T(x') = \frac{e^{ikz} e^{\frac{ikx'^2}{2z}}}{i\lambda z} \int_{-\infty}^{\infty} T(x) e^{\frac{-i2\pi}{\lambda z} x'x} dx \ . \tag{1.9}$$

Ignoring the terms in front of the integral for the moment yields:

$$T(x') \propto \mathcal{FT}\{T(x)\}\Big|_{x'=x/\lambda z} = \left[B\left(\frac{x'}{\lambda z}\right) comb\left(\frac{\Lambda x'}{\lambda z}\right) \right] * A\left(\frac{Wx'}{\lambda z}\right) , \tag{1.10}$$

where $\mathcal{FT}$ represents the Fourier Transform. It can now be observed from Eqn. 1.10 that the field at the detector plane is characterized by a periodic transmission function which results in the diffracted beam having many orders or modes. The location and magnitude of each mode is described by {comb} and by {B}, respectively, both of which are dependent on the wavelength λ.[2] With

this in mind the far-field intensity measured at the detector plane can be described by

$$I_T(x') \propto \left[\left\{B\left(\frac{x'}{\lambda z}\right) comb\left(\frac{\Lambda x'}{\lambda z}\right)\right\} * A\left(\frac{Wx'}{\lambda z}\right)\right]^2, \tag{1.11}$$

which is characterized by similar periodic transmission and weighting functions.

Solving explicitly for this intensity yields an equation which is a function of two different sinc^2 functions:

$$I_T(x') \propto \sum_{j=-\infty}^{\infty} \text{sinc}^2\left\{\left(\frac{x'}{z} - j\frac{\lambda_{probe}}{\Lambda}\right)\frac{W}{\lambda_{probe}}\right\} \text{sinc}^2\left\{\pi\left(\frac{\Delta n_{probe}\lambda_{design}}{\Delta n_{design}\lambda_{probe}} - j\right)\right\} \tag{1.12}$$

where the first represents the diffraction orders and the second is the envelope function. Equation 1.12 is examined in Figure 1.4 as a function of two different wavelengths: the blaze design wavelength and a probe wavelength. At a probe wavelength equal to the design wavelength, $\lambda_{design} = 550\,\text{nm}$, the zeroes of the

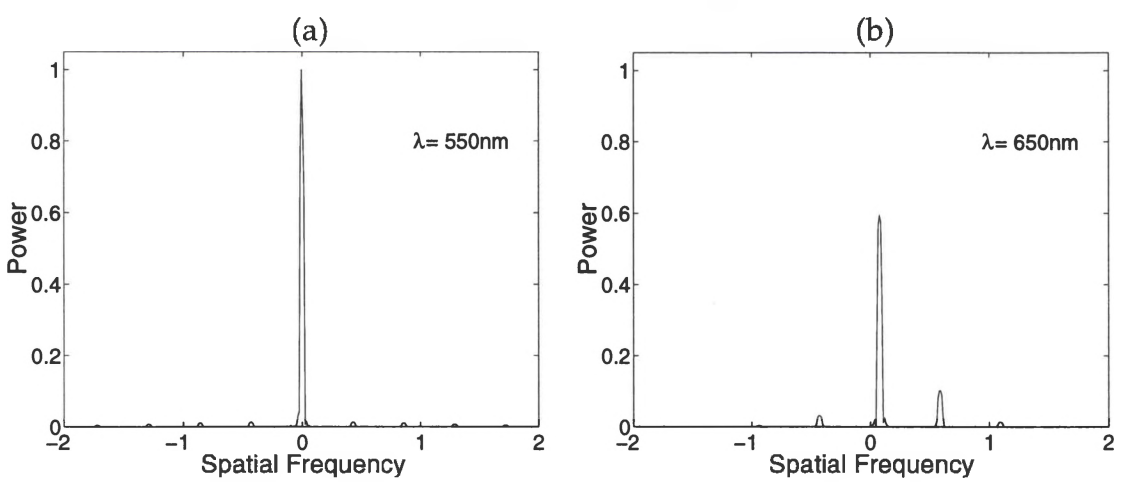

Figure 1.4) *The resulting intensity pattern for the analytic solution for both the (a) design wavelength of 550 nm and (b) a probe wavelength of 650 nm.*

weighting (envelope) function are aligned with the peaks of the diffraction orders. This results in a cancellation of all of the peaks except for one (Figure 1.4(a)). At a different probe wavelength, $\lambda_{probe} = 650\,\text{nm}$, the envelope function is shifted with respect to the diffraction orders, which are also shifted due to the probe wavelength. The result is a far-field pattern with extra bumps, or echoes, and a main peak which has a lower intensity (Figure 1.4(b)).

1.3 Image Restoration Solution

Compensation for the degradations introduced into the steered broad-band field of view involves the process of post-detection image restoration. Image restoration, which is the process of minimizing the known degradations in an image,[14] is difficult due to the combination of degradation mechanisms. For the beam steering apparatus the worst degradations are blurring, caused by material and grating dispersion, and echoing, caused by multiple diffraction orders. An example of this image degradation is shown below in Figure 1.5. A spoke target, illuminated with a band-limited white light source (400-700 nm), is then propagated through the beam steering device during the *off* condition (unsteered) and *on* condition (steered). To undo image degradations, such as those displayed in Fig. 1.5, a beam-propagation model (*BPM*) is developed to provide a good estimate of the beam steerer impulse response as a function of wavelength. Based on this, the Wiener filter impulse response for image

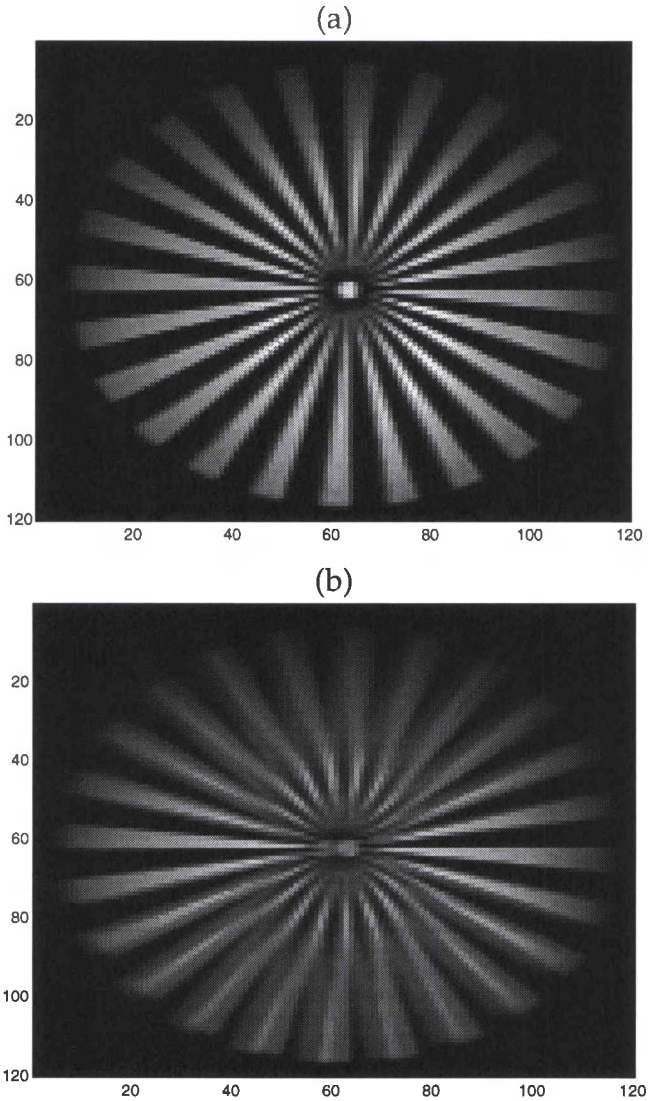

Figure 1.5) *Example of (a) unsteered and (b) steered spoke target illuminated with a broad-band (400-700 nm) white light source through the liquid crystal beam steering device.*

restoration is found. The Wiener filter gives the best mean-square estimate of the original object[14] when applied to the corrupted image and can accommodate the presence of additive noise in images. Unfortunately, the noise and signal statistics must be known or estimated because the optimal Wiener filter requires the noise-to-signal power spectral density ratio. This information is often difficult to obtain *a priori* and therefore a spectrally flat noise-to-signal ratio is

inserted into the Wiener filter. In addition, when "training data" is available for the device (knowledge of the steered *and* unsteered images), the Least Mean Square (*LMS*) adaptive algorithm is used to improve the image restoration filter. The *LMS* algorithm is the simplest and most widely used algorithm for adjusting the weights in a linear adaptive system.[15] Thus, the restoration application makes efficient use of a train of standard algorithms: *BPM* → Wiener Filter → *LMS*, as summarized in Table 1.1 below.

Table 1.1) *Summary of the image restoration algorithm.*

1) Find the BPM model impulse response
2) Estimate the signal statistics and calculate the Wiener filter
3) If training data exists, refine the filter with the LMS algorithm

We would like to use this image restoration algorithm to compute filters for an entire range of field conditions including steer angle, bandwidth, and scene information (spectral emission). Since the device may eventually be used to steer a large field of view, it may not be possible to capture a desired, unsteered version of each steered image. Thus we require a set of filters to be computed beforehand, possibly using data captured in the laboratory or during a test flight. This set of filters can then be stored in a data "bank" and called upon when the corresponding steering conditions arise. Each of the algorithms listed in Table 1 is described in detail before presenting narrow- and broad-band image restoration results. The beam propagation method is described in Chapter 2 and

the Wiener and LMS filtering algorithms are described in Chapter 3. Theoretical and experimental results are then presented for both narrow spectral band and broad spectral band data in Chapters 4 and 5, respectively.

CHAPTER 2

Beam-Propagation Method (Theoretical Modeling)

One of the most robust and efficient methods for analyzing diffraction problems is the well-known beam-propagation method (*BPM*).[16-19] The *BPM* is quite general and can model optical beam propagation through scattering and distorting media such as the atmosphere, optical fibers, volume holographic elements, grating lenses, spatial light modulators, *etc*. The *BPM* can also be used to model the behavior of an optical beam through a liquid crystal beam steering device.

2.1 Numerical Model

The *BPM* simplifies the problem of an optical beam propagating through a given distorting media by splitting the problem into two parts: propagation and modulation. Propagation is a term used to describe how the angular spectrum of the optical wave changes as it moves through a homogeneous medium. By decomposing the incident beam into a set of plane waves traveling at different angles, a mathematical description can be developed which completely describes

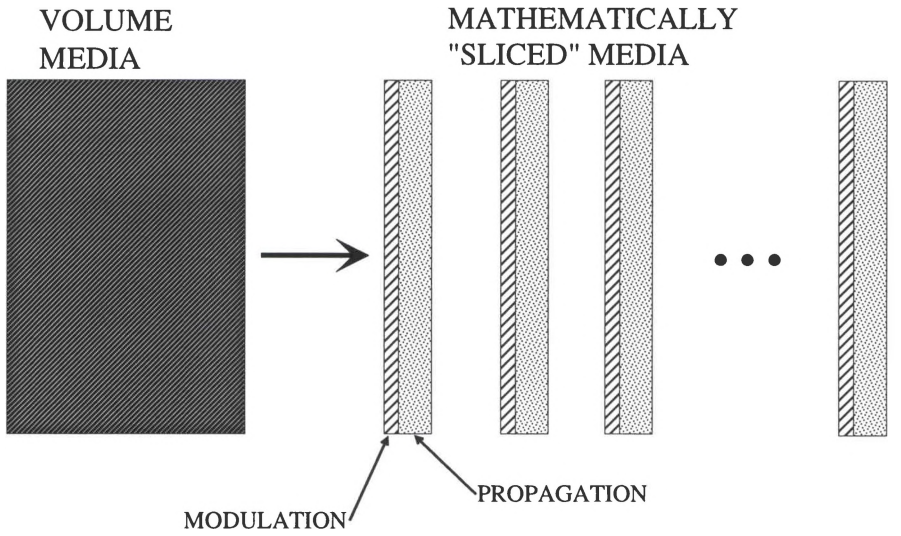

Figure 2.1) *Effect of mathematically breaking up the volume media (grating) into several thin slices with modulation and propagation processes performed on each single slice.*

the propagation of the waves at the different angles. Modulation is a term which describes the transverse spatial variation of the absorption and/or index of refraction. The absorption and index of refraction represent amplitude modulation and phase modulation, respectively, of the near-field optical wave.

The BPM requires the volume distorting media to be "sliced" into a given number of layers (Figure 2.1), with the propagation and modulation processes performed on each slice. The propagation of an optical beam through the liquid crystal steering device is modeled by angular spectrum propagation over a distance Δz through a homogeneous liquid crystal medium with a constant background index of refraction (no modulation). Modulation is modeled by a phase change based on the index of refraction of the liquid crystals over the same Δz (no diffraction). For a incident light beam traveling in the z direction, assume

the beam is composed of a slowly varying envelope function, A, and rapidly varying exponential phase function:

$$A_T(x,z) = A(x,z)e^{ikz} \quad , \tag{2.1}$$

where $k = 2\pi n/\lambda$ is the magnitude of the wave vector in the media. Note that only one transverse spatial coordinate, x, is needed to describe the incident beam for a one-dimensional steering device. If Equation 2.1 is to represent an optical wave, it must satisfy the time-independent scalar wave equation in a charge-free *homogeneous* medium, or Helmholz equation[12]

$$\nabla^2 A_T + k^2 A_T = 0 \quad , \tag{2.2}$$

where $\nabla^2 = \frac{\partial^2}{\partial x^2} + \frac{\partial^2}{\partial z^2}$. Placing A_T into the above equation yields:

$$\frac{\partial^2 A}{\partial z^2} e^{ikz} + 2ik\frac{\partial A}{\partial z} e^{ikz} + \frac{\partial^2 A}{\partial x^2} e^{ikz} = 0 \quad . \tag{2.3}$$

This expression can be simplified further by assuming that the envelope function, A, varies slowly as it moves along z, or $2ik\frac{\partial A}{\partial z} >> \frac{\partial^2 A}{\partial z^2}$. This simplification is true if the change in A is very small compared to the magnitude of A, over a propagation distance of approximately one wavelength. The result gives a relationship between the propagation of an optical wave (left hand side

of Eqn. 2.4) and the diffraction of an optical wave:

$$2ik\frac{\partial A}{\partial z} = \frac{\partial^2 A}{\partial x^2} \ , \tag{2.4}$$

which tells how the beam spreads out, or diffracts, as it propagates in the z-direction. This equation is analogous to the temporal diffraction of an optical beam where the optical pulse lengthens in time as it propagates.

Since the liquid crystal beam steering device represents a periodic grating in the x-direction with spatial extent X_{max}, the slowly varying envelope function can be sampled at a discrete set of NX points,

$$x_\ell = \frac{\ell\, X_{max}}{NX}, \quad \text{for } \ell = 0 \rightarrow NX - 1 \ , \tag{2.5}$$

thus decomposing the light field into a discrete set of plane waves:

$$A(x,z) = \sum_{\ell=-\frac{NX}{2}}^{\frac{NX}{2}-1} \mathbf{A}_\ell(z) e^{i2\pi\ell x / X_{max}} \ . \tag{2.6}$$

This decomposition represents the definition of the inverse Fourier transform of A. The function $\mathbf{A}_\ell$ is thus a weighting function for each of the plane wave components constructing A. Each plane wave component, index ℓ, has a corresponding spatial frequency $f_\ell = \ell / X_{max}$ (from Eqn. 2.6), traveling at angle

$$\theta_\ell = \lambda f_\ell = \ell \frac{\lambda}{X_{\max}} \quad . \tag{2.7}$$

The propagation solution for these spatial frequencies can now be found by putting the expression derived for *A(x,z)* (Eqn. 2.6) into the diffraction equation derived earlier (Eqn. 2.4), this yields:

$$2ik \frac{\partial \mathbf{A}_\ell}{\partial z} = -\left(\frac{2\pi \ell}{X_{\max}} \right)^2 \mathbf{A}_\ell \quad . \tag{2.8}$$

where the common exponential terms divide out. Solving this equation for $\mathbf{A}_\ell$ shows that the spatial frequencies of the incident optical beam propagate according to

$$\mathbf{A}_\ell(z + \Delta z) = \mathbf{A}_\ell(z) e^{i\pi(\Delta z/\lambda)\theta_\ell^2} \quad . \tag{2.9}$$

In the *absence* of modulation effects the slowly-varying amplitude function is Fourier transformed at its current position (z), multiplied by a complex phase factor, and then inverse Fourier transformed back to get the amplitude at the new plane ($z+\Delta z$). Each plane-wave component travels at a slightly different angle, given by Equation 2.7, so that after traversing a slice of material Δz thick the angular components accumulate different optical phases (Eqn. 2.9). This portion of the *BPM* is computationally efficient because it involves only two FFT operations and one complex multiplication per slice.

The modulation aspect of the problem is examined by imagining that if the slices of the medium are thin enough, then the beam shape will not change much in crossing a slice. After allowing the beam to cross the first half of the slice without modulation effects (using Eqn. 2.9), the diffraction problem is ignored thus allowing only modulation effects via the following simple multiplication in real space

$$A(x,z+\Delta z) \;=\; e^{-\alpha(x)\,\Delta z/2}\; e^{i\,2\pi n(x)\,\Delta z/\lambda}\; A(x,z)\;, \qquad (2.10)$$

where $\alpha(x)$ is the intensity attenuation coefficient and $n(x)$ is the refractive index. The full *BPM* solution consists of alternating between Eqn. 2.9 (propagation) and Eqn. 2.10 (modulation) using a series of Fast Fourier Transforms. For the case of the liquid crystal beam steerer, the amplitude modulation factor is 1 because the liquid crystals do not exhibit any absorption characteristics the visible spectrum.

The *BPM* solution has the added advantage that a near- and far-field description of the beam is available at each slice throughout the propagation.[18] Note that both effects (diffraction & modulation) occur simultaneously in the actual propagation but the two effects are separated within the thin slices for tractable calculation. The *BPM* model will closely approximate the actual solution as the slices of the liquid crystal cell are made thinner.

2.2 Optical Phase Delay

The phase profile across the beam steering device is ideally composed of a set of linear phase ramps climbing to 2π optical phase delay (*OPD*) and then resetting to zero (shown in Fig. 1.3). This spatially-dependent phase profile is inserted into the modulate function (Eqn. 2.10) of the *BPM* . Phase ramps designed to give 2π resets at λ_{design} are altered at other wavelengths λ_{probe} according to[20]

$$OPD(x;\lambda_{probe}) = \frac{\lambda_{design}}{\lambda_{probe}} \frac{\Delta n(\lambda_{probe})}{\Delta n(\lambda_{design})} OPD(x;\lambda_{design}) , \qquad (2.11)$$

where the dispersion of Δn in the visible is approximated by Equation 1.4. The phase resets occur at the same transverse locations (x) but now the *OPD* is not necessarily 2π at the reset resulting in diffraction-grating dispersion for wavelengths other than λ_{design}. This simple *BPM* model of the beam steering device is found to accurately predict the impulse response throughout the visible spectrum as a function of the *OPD*.[21]

2.3 Comparison of BPM vs. Experiment

In this section the accuracy of the *BPM* to predict narrow spectral band and broad spectral band steered results in the visible spectrum is examined. Comparisons are made between experimental images taken with the steering

device and the equivalent numerical simulations produced by the *BPM*. The computer code for the *BPM* can be found in Appendix A. It is important to note that the accuracy of the *BPM* to correctly predict the behavior of the steering device is based on how well it's results correspond to experimental data. It is difficult to associate a numerical value, such as mean squared error (*MSE*), to the accuracy because there is not a baseline value with which to compare. Diffraction order magnitude and position, therefore, determine the viability of the *BPM* model, and it is shown that the model works quite well. The remainder of this chapter is devoted to visual and numerical comparisons between the *BPM* model and experimental data, both narrow- and broad-band.

The main concern in using the numerical standard of mean square error to measure accuracy lies in the spatial DC component of the experimental data that is very difficult to model. The DC component present in the images is due largely to a background detector signal (radiation). To avoid altering the experimental data by removing the DC component, other measurement criteria are used which measure the relative magnitude and position of the model and experimental steered results. These criteria include magnitude ratios involving the unsteered peak, steered peak, and diffraction sidelobes and the far-field (angular) spacing of the sidelobes. With these measurements a more concise comparison can be made between the model and experiment.

To characterize the response of the beam steering device, an imaging system is constructed which is used to image both steered and unsteered targets using either narrow- or broad-band illumination (Figure 2.2). To acquire the narrow-band images a circular variable interference filter is used as the SPECTRAL FILTER in Figure 2.2. Rotating this filter tunes its passband over the entire visible spectrum with a bandwidth of ±8-15 nm. The SPECTRAL FILTER for the broadband images consists of a low pass and a high pass filter, producing a bandpass filter of 400-700 nm. A single 25 μm slit is inserted as the target which acts like a narrow bar target. This type of target, which is the effective light source seen by the steering system, is very easy to propagate with the *BPM* model.

The first results examined consist of six various narrow-band probe wavelengths incident on the single slit. The light is then propagated through a beam steering device designed for a wavelength of 543 nm and a steer angle of

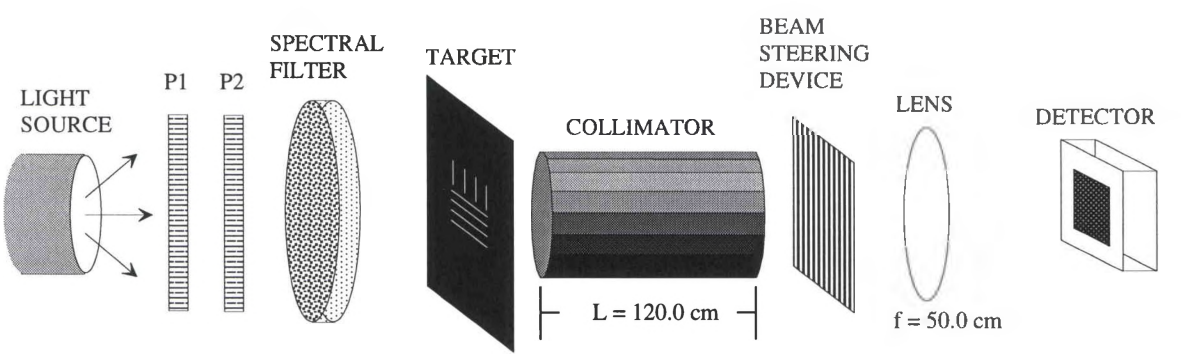

Figure 2.2) *Imaging system using the broadband beam steerer to steer the field of view. P1 and P2 are sheet polarizers that insure the light polarization lies along the director of the liquid crystals and adjust the total transmittance into the detector. The device steers in the horizontal direction.*

Table 2.1) *Ratio of the steered peak magnitude to that of the unsteered peak. The percent difference between the BPM and experiment is given.*

θ_{steer}=0.024°	λ					
	435 nm	488 nm	543 nm	596 nm	639 nm	681 nm
BPM	0.424	0.756	0.882	0.864	0.813	0.751
Experiment	0.462	0.736	0.934	0.950	0.818	0.630
% Difference	8.4%	2.7%	5.8%	9.7%	0.5%	17.6%

0.024°. Each of the steered results for the six probe wavelengths is shown in Figure 2.3, both *BPM* and experimental. Table 2.1 shows a ratio of the steered peak magnitude to the unsteered peak magnitude at each of the six wavelengths. The percent difference between the two results is also calculated and is observed to be quite small. Inaccuracies in the theoretical prediction are a result of the approximate phase profile inserted into the *BPM* which attempts to model actual device behavior. The phase ramps inserted into the *BPM* are altered from the ideal linear ramps to best match the steered data from the device.[21] The phase profile of the liquid crystal device is an extremely important factor since it may change from one device to the next and it may change from day to day with a given device. This makes it difficult to model the phase profile without a phase image of a real device.

A ratio of the largest secondary diffraction order (sidelobe) magnitude to

Table 2.2) *Ratio of the largest sidelobe magnitude to that of the steered peak. The percent difference between the BPM and experiment is given. Note that the largest sidelobe in the experimental images was the same as that in the BPM predictions.*

θ_{steer}=0.024°	λ					
	435 nm	488 nm	543 nm	596 nm	639 nm	681 nm
BPM	0.838	0.145	0.037	0.030	0.039	0.051
Experiment	0.833	0.101	0.042	0.050	0.058	0.076
%Difference	0.3%	17.7%	6.9%	25.1%	19.2%	19.9%

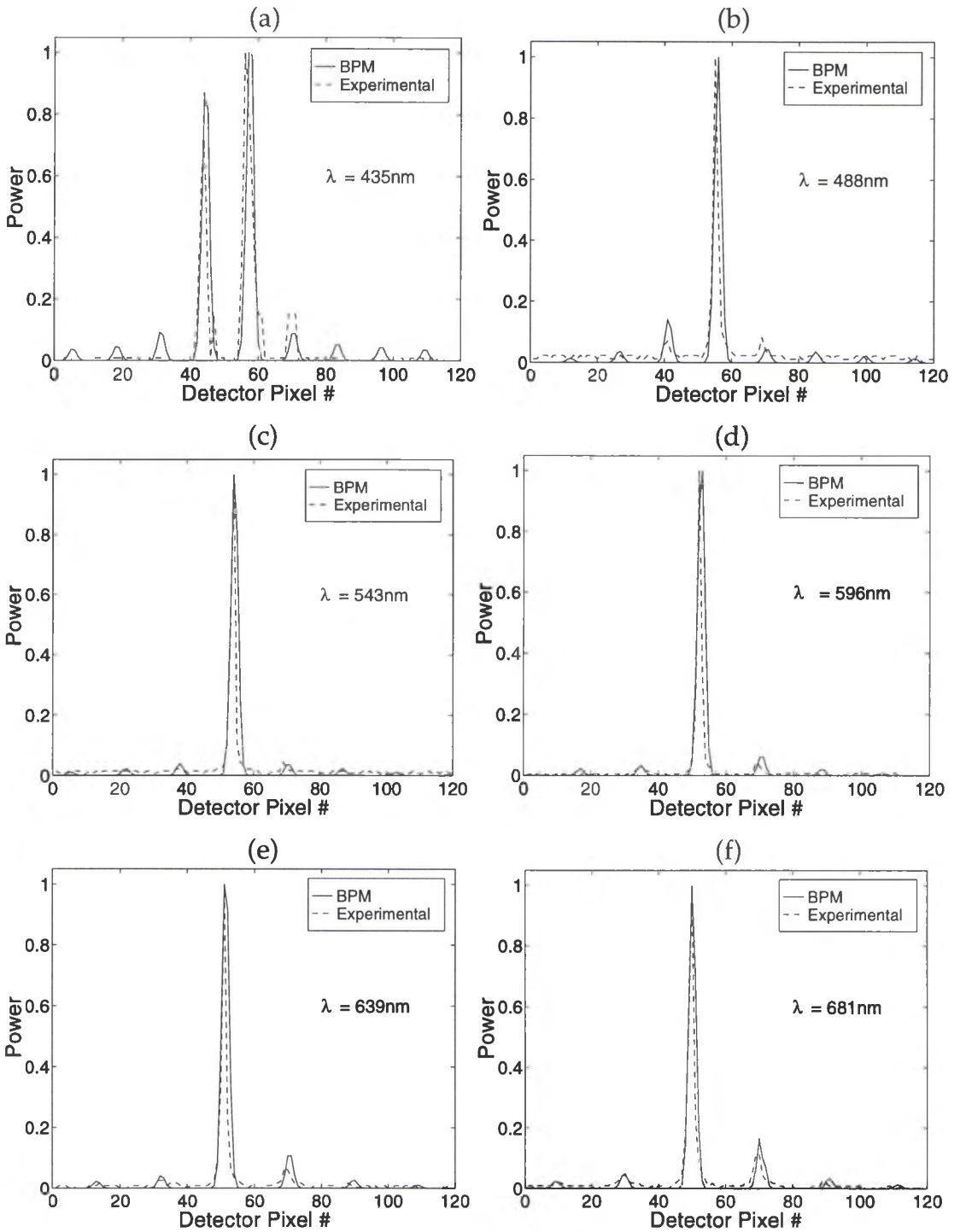

Figure 2.3) *Comparison of narrow-band steered 1-D single slit, BPM model and experimental. Results are shown for six different probe wavelengths steered using a device with the 2π phase shift set for a wavelength of 543 nm. Wavelengths of (a) 435 nm, (b) 488 nm, (c) 543 nm, (d) 596 nm, (e) 639 nm, (f) 681 nm, are steered to an angle of 0.024°. Numerical measurements for these results are found in Tables 2.1, 2.2, and 2.3.*

Table 2.3) *Separation (in detector array pixels) of the largest sidelobe and the steered peak. The percent difference is given. It is important to note that due to the limited resolution of the CCD detector, a peak position can only be measured to an accuracy of about one-half pixel. Therefore, a zero percent difference in the pixel positions does not necessarily indicate that the peaks lie exactly at the same position.*

θ_{steer}=0.024°	λ					
	435 nm	488 nm	543 nm	596 nm	639 nm	681 nm
BPM	12.0	13.0	14.0	15.0	16.0	17.0
Experiment	12.0	14.0	16.5	17.5	18.0	20.5
% Difference	0.0%	3.7%	8.2%	7.7%	5.9%	9.3%

the steered peak magnitude was also measured. The results, presented in Table 2.2, also show a close correspondence of the model to the experimental results.

Finally, a measurement is made of the far-field spacing of the steered peak and the largest sidelobe. The results in Table 2.3 are given in numbers of detector array pixels, each of which corresponds to 0.0015° in angular space. Note again the close correspondence between the model and experiment. It is important to note that the data measurements made for a steer angle of 0.024° were also repeated for other steer angles: 0.018°, 0.012°, 0.006°, 0.002°. Similar percent difference values were found for the same three measurements over the range of steer angles. This indicates that the performance of the model remains reasonably constant versus steer angle. Additional narrow-band characterizations have been performed by Carney, *et al.*[21]

Broad-band results presented here involve the 400-700 nm bandwidth of the visible spectrum. The device design wavelength for this data remains the same as that of the narrow-band data above: 543 nm. Four different bandwidths are

examined and compared to the model using the same three measurements made on the narrow-band data set. These bandwidths are: 400-700 nm, 450-650 nm, 500-600 nm, and 600-700 nm. The size of these bandwidths was limited by the available (Corion) highpass and lowpass filters. Figure 2.4 shows the single slit steered to 0.024° for each of the four bandwidths. Note the relatively small amount of grating and material dispersion smearing as the bandwidth changes.

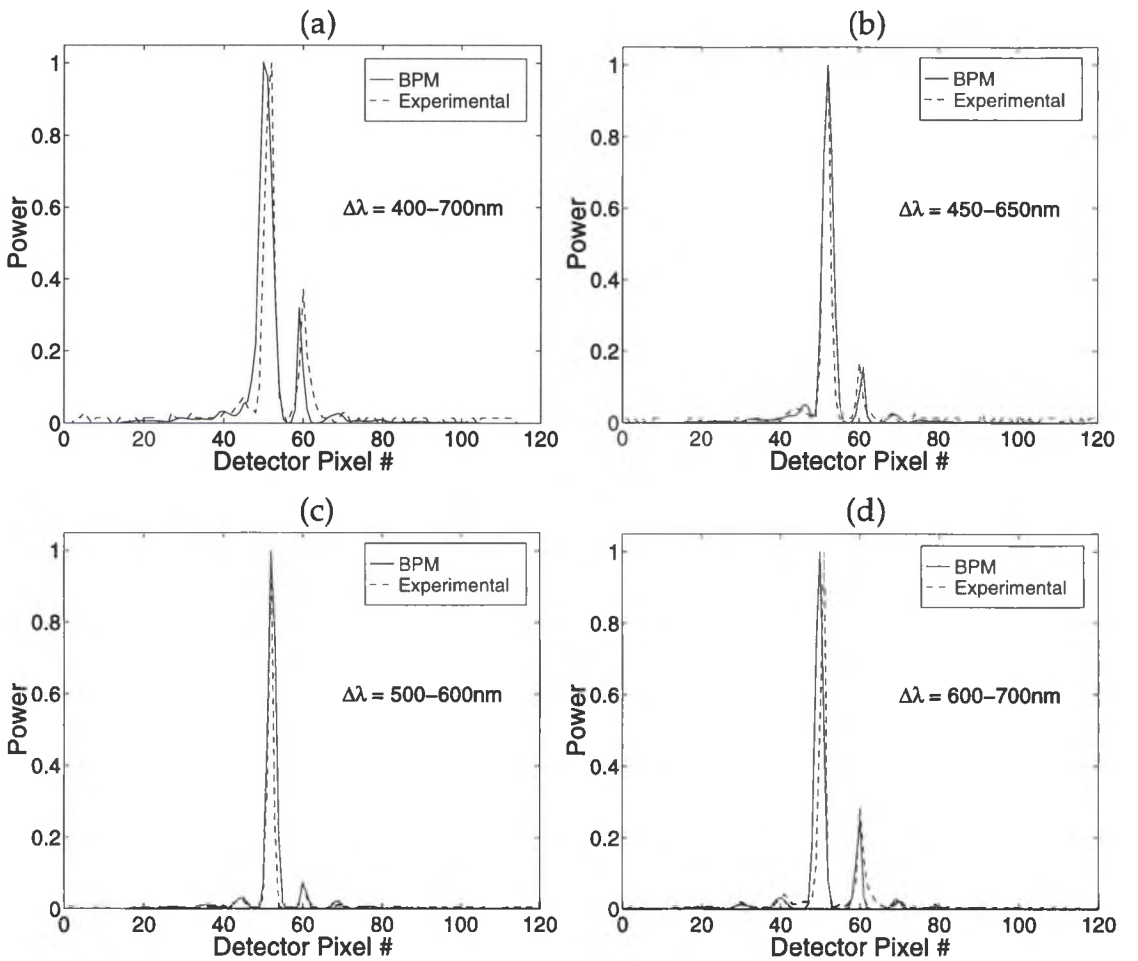

Figure 2.4) *Comparison of broad-band steered 1-D single slit, BPM model and experimental. Four different bandwidths are steered using a device with the 2π phase shift set for a wavelength of 543 nm. Bandwidths of (a) 400-700 nm, (b) 450-650 nm, (c) 500-600 nm, (d) 600-700 nm, are steered to an angle of 0.024°. Numerical measurements for these results are found in Tables 2.4, 2.5, and 2.6.*

Table 2.4) *Ratio of the steered peak magnitude to that of the unsteered peak. The percent difference between the BPM and experiment is given.*

θ_{steer}=0.024°	$\Delta\lambda$			
	400-700 nm	450-650 nm	500-600 nm	600-700 nm
BPM	0.484	0.614	0.797	0.724
Experiment	0.338	0.431	0.763	0.691
% Difference	17.8%	17.5%	2.2%	2.3%

This effect is a result of the relatively large beam width, or spot size propagated through the imaging system which dominates over the smearing effect. To predict the broad-band response from the *BPM*, a set of single wavelength responses was calculated and then incoherently superimposed to give an approximate broad-band response. Each of the superimposed wavelengths propagated by the *BPM* had approximately the same spot size as the broad-band slit: $\cong 0.009°$. The effect of the spot size on broad-band model predictions is examined in Chapter 5.

To begin the broad-band comparisons the ratio of the steered peak magnitude to the unsteered peak magnitude is measured at each of the four bandwidths. The percent difference between the two results is calculated and is presented in Table 2.4. Note that the steered peak of the model has a larger magnitude with respect to the unsteered peak for each of the four bandwidths. This is largely due to the phase profile inaccuracies and also the noise sources in the experimental set-up which are not included in the model. Noise introduced by the detector nonlinearities, background radiation, and random particles (dust) will all contribute to the total noise but are very hard to model.

A ratio of the largest secondary diffraction order (sidelobe) magnitude to the steered peak magnitude was also measured. These results, presented in Table 2.5, also show a close correspondence of the model to the experimental

Table 2.5) *Ratio of the largest sidelobe magnitude to that of the steered peak. The percent difference between the BPM and experiment is given.*

θ_{steer}=0.024°	Δλ			
	400-700 nm	450-650 nm	500-600 nm	600-700 nm
BPM	0.016	0.033	0.026	0.025
Experiment	0.029	0.022	0.028	0.033
% Difference	28.5%	19.5%	2.8%	14.0%

results. The final measurement is the far-field spacing of the steered peak to the largest sidelobe. The results in Table 2.6 are given in numbers of detector array pixels, each of which corresponds to 0.003° in angular space. Close correspondence can again be seen between the model and experiment. It is important to note that these measurements were also made for steer angles of 0.018°, 0.012°, and 0.006°. Similar percent difference values were found for these three measurements over the range of steer angles. This again indicates that the performance of the model remains reasonably constant versus steer angle.

Table 2.6) *Separation (in detector array pixels) of the largest sidelobe and the steered peak. The percent difference is given. Note again that due to the limited detector resolution, the accuracy of peak position is limited to about one-half pixel.*

θ_{steer}=0.024°	Δλ			
	400-700 nm	450-650 nm	500-600 nm	600-700 nm
BPM	5	9	9	10
Experiment	6	8	8	10
% Difference	9.1%	5.9%	5.9%	0.0%

2.4 Conclusion

Examining the results in this chapter as well as other work[21] indicate that the Beam Propagation Method is an excellent method of modeling the behavior of the beam steering device. It provides a method of estimating the response of the steering system (including lenses, detector resolution, etc...) which can be used to help restore dispersion degraded images. This response can be used by the image restoration algorithms in Chapter 3 to estimate the optimal filter coefficients used in image restoration of both narrow- and broad-band degraded images. It is important to note, however, that the accuracy of the *BPM* is limited by the accuracy of the phase profile and the noise statistics which are present in the imaging system. The performance of the *BPM* can conceivably be improved by measuring the phase profile of a real device and incorporating the result into the prediction model.

CHAPTER 3

Restoration Algorithms

In this chapter, methods of restoring the severe image degradations introduced by the beam steering device are described. Recalling Figures 2.3 and 2.4 it can be seen that the steering device acts like a diffraction grating to all wavelengths not equal to the given device design wavelength. Steered optical beams experience smearing and echoing effects as a result of material and grating dispersion. To correct for these effects a mathematical model is first developed to describe the degradation process. Depending on the availability of degraded and desired (unsteered) test data, one or both of the filtering algorithms is then used to compute optimal correction coefficients.

3.1 Wiener Filtering Algorithm

To begin restoring the degradations found in the steered images, the imaging system is modeled as a discrete linear system so that the degraded image $g(m)$ is expressed as a linear convolution of the object $f(l)$ and the

wavelength dependent point spread function (*PSF*) of the beam steering device $h(m)$

$$g(m) = \sum_{l=-\infty}^{\infty} h(m-l)f(l) \ . \tag{3.1}$$

A common solution method for finding the object is the inverse filter.[14,15,22] The inverse filter is readily derived by taking the Fourier transform of the image $g(m)$ and solving for $F(\omega)$, yielding

$$F(\omega) = \frac{1}{H(\omega)} G(\omega) \ . \tag{3.2}$$

Thus the inverse filter frequency $H^I(\omega)$ response is defined by:

$$H^I(\omega) \ = \ \frac{1}{H(\omega)} \ . \tag{3.3}$$

A simple inverse filter, however, is not a very good model of the imaging system due to its instability, or sensitivity to noise. Since noise is present in the system and cannot be avoided an alternate filtering method must be employed: the Wiener filter. The Wiener filter presents a method of restoring degraded images in the presence of noise as well as blur.[14] This filtering method gives the best linear estimate $\hat{f}(m)$ of the object $f(m)$ such that the mean square error (*MSE*) ζ_e

$$\zeta_e = E\left\{\left[f(m) - \hat{f}(m)\right]^2\right\} \tag{3.4}$$

between the estimate and the object is minimized.

To compute the Wiener Filter, a more accurate model for the imaging system pictured in Figure 2.2 must be created. This is done by placing a term into the system model of Equation 3.1 representing the additive noise present in the imaging system:

$$g(m) = \sum_{l=-\infty}^{\infty} h(m-l) \cdot f(l) \; + \; \eta(m) \; , \tag{3.5}$$

where $\eta(m)$ is assumed to be a stationary noise sequence uncorrelated with the object $f(l)$. Minimizing the *MSE* between the original object and the filter estimate, considering the additive noise term, gives the frequency response of the optimal restoration filter, or infinite impulse response (IIR) Wiener filter[14]

$$H^W(\omega) \; = \; \frac{H^*(\omega) S_{ff}(\omega)}{|H(\omega)|^2 S_{ff}(\omega) + S_{\eta\eta}(\omega)} \; = \; \frac{1}{\mathrm{H}(\omega)} \cdot \frac{|H(\omega)|^2}{|H(\omega)|^2 + S_{\eta\eta}(\omega) / S_{ff}(\omega)} \; , \tag{3.6}$$

where S_{ff} and $S_{\eta\eta}$ are the power spectral densities of the object and noise, respectively. Since it is difficult to approximate the power spectrum of the noise and signal, a constant (Γ) that represents an average noise to signal ratio is often substituted. This simplification gives the well known form of the Wiener filter used in calculations[14,15,22]

$$H^{W}(\omega) \approx \frac{1}{\mathrm{H}(\omega)} \cdot \frac{|H(\omega)|^2}{|H(\omega)|^2 + \Gamma} . \qquad (3.7)$$

The IIR Wiener filter is implemented in our system by first truncating the discrete Fourier transform of a spatially sampled beam steerer *PSF*. After this result is placed in Eqn. 3.7, an inverse discrete Fourier transform of the frequency sampled Wiener filter H^{W} is taken and the truncated result gives our spatial domain Wiener filter coefficients.

To accommodate effects such as noise and detector nonlinearities that contribute to the steering behavior which are not taken into account by the *BPM* model and the Wiener filter, the *LMS* adaptive algorithm is utilized. The *LMS* algorithm can adapt to specific signal and noise statistics in a training sequence.

3.2 *LMS* Algorithm

The *LMS* algorithm applies the finite impulse response (FIR) Wiener filter to the system input (steered image) and adjusts its internal parameters (filter weights) to produce an estimate which best approximates the desired output (unsteered image).[15,22-25] Note that the *LMS* algorithm is not universally applicable and can only be used as an adaptive linear combiner (Figure 3.1) where the input (degraded result) and the desired response are given.[24]

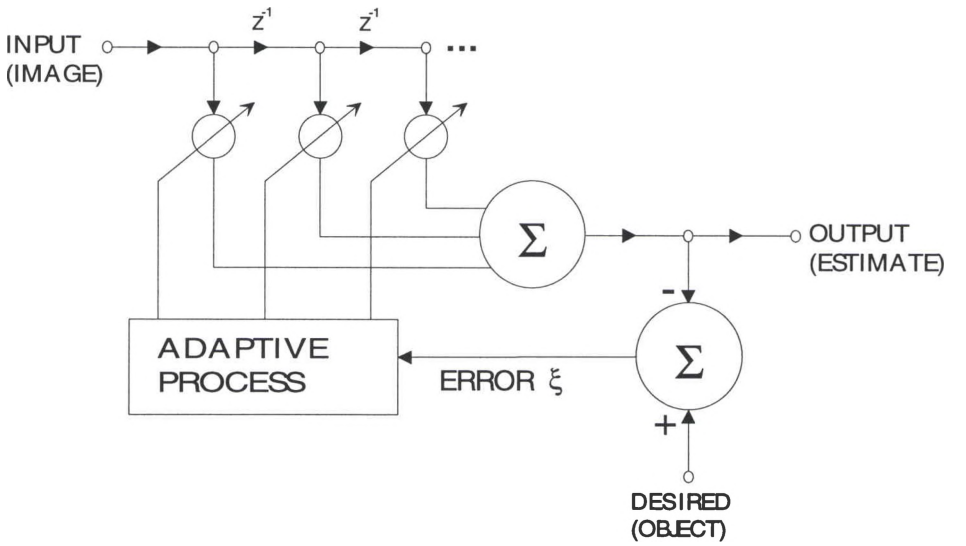

Figure 3.1) *Block diagram of an adaptive linear combiner. The input represents each detector sample of the degraded, steered image. The output is a result of each input sample multiplied by an adaptive filter coefficient. The error is then found between the filter output and the desired unsteered image. The error is then used to compute new filter coefficients for the next adaptation step.*[23,24]

Let us consider the input (image) sequence $\{g(m)\}$ and the desired (object) sequence $\{f(m)\}$ consisting of $N+1$ samples from the detector array where m is a point in the sequence. Let $\mathbf{g}(m)$ be an observation vector containing samples spanned by a moving window that passes across the input sequence. Specifically this vector is denoted:

$$\mathbf{g}(m) = [g(m-L) \ \ldots \ g(m) \ \ldots \ g(m+L)]^T \ . \tag{3.8}$$

Note that the steered sequence $\{g(m)\}$ is padded with L zeros at each end of the sequence allowing each filter coefficient to multiply each image point as it is convolved with the image. This gives each coefficient a chance to train on each

image point thus giving the most robust filter. The filter output is expressed at each position m as the product of the observation vector and the filter weights:

$$\hat{f}(m) = \mathbf{W}^{\mathrm{T}}\mathbf{g}(m) \ , \tag{3.9}$$

where $\mathbf{W}$ is a $2L+1$ length vector of filter weights:

$$\mathbf{W} = [W(0) \ \ W(1) \ \ \ldots \ \ W(2L)] \ . \tag{3.9a}$$

The length of the filter weight vector was typically chosen so that it extended across the entire steered image and thus the degradations. This allows the filter coefficients to span the entire steered image at one time and thus adapt to all of the degradations. From the expression for the filter output, the estimation error between the filter output and the desired signal $f(m)$ is

$$\xi(m) \ = f(m) - \hat{f}(m) \ = \ f(m) - \mathbf{W}^{\mathrm{T}}\mathbf{g}(m) \ . \tag{3.10}$$

The mean square error between the filter output and the desired signal is now found using Equation 3.4. Squaring ξ(m) to obtain the instantaneous squared error and taking the expected value of the expression yields

$$E\{\xi^2(m)\} = E\{f^2(m)\} + \mathbf{W}E\{\mathbf{g}^{\mathrm{T}}(m)\ \mathbf{g}(m)\}\mathbf{W}^{\mathrm{T}} - 2E\{f(m)\ g^{T}(m)\}\mathbf{W}^{\mathrm{T}} \ . \tag{3.11}$$

Assuming the signals are wide sense stationary, the expression for the mean square error (MSE) can be reduced to a more compact form using the input

image auto-correlation matrix R and a cross-correlation vector P of the original and the image, both of which are real:[15]

$$MSE \equiv \zeta_e = E[\xi^2(m)] = E[f^2(m)] + \mathrm{W\,R\,W^T} - 2\mathrm{P\,W^T} \ . \qquad (3.12)$$

The mean square error is a quadratic function of the filter weights that can be pictured as a concave parabolic surface. It has a single fixed minimum point that is readily found using gradient descent techniques.[15] The gradient method adapts the weight vector to seek the minimum of the quadratic performance surface which represents the minimum mean square error and thus gives the optimal filter weights. The gradient of the *MSE* performance surface, ζ_e, is found by differentiating the *MSE* with respect to the filter weights giving

$$\nabla = 2\mathrm{RW} - 2\mathrm{P} \ . \qquad (3.13)$$

To obtain the minimum *MSE*, the above equation is set to zero and a solution is found for the optimal weight vector, W^{opt}, (assuming R is a nonsingular matrix)[14,15,23]

$$\mathrm{W}^{opt} = \mathrm{R}^{-1}\mathrm{P} \ , \qquad (3.14)$$

which is the Wiener-Hopf equation (FIR Wiener) in matrix form.[14,15]

The *LMS* algorithm presents a simple method for descending the performance surface assuming training data exists without explicitly calculating R and P. Actually solving for R would be very difficult due to the large number

of weights and the required inversion of the subsequently large matrix. This lengthy inversion process would also have to be repeated for each new filter. Assuming the square of the estimation error, ξ^2, is an estimate of the *MSE*, a gradient estimate vector can be found at each position m by differentiating ξ^2 with respect to the filter weights:

$$\hat{\nabla}(m) = \begin{bmatrix} \frac{\partial \xi^2(m)}{\partial W(0)} \\ \frac{\partial \xi^2(m)}{\partial W(1)} \\ \vdots \\ \frac{\partial \xi^2(m)}{\partial W(2L)} \end{bmatrix} = 2\xi(\mathrm{m}) \begin{bmatrix} \frac{\partial \xi(m)}{\partial W(0)} \\ \frac{\partial \xi(m)}{\partial W(1)} \\ \vdots \\ \frac{\partial \xi(m)}{\partial W(2L)} \end{bmatrix} = -2\xi(m)\, g(m) \quad . \tag{3.15}$$

The *LMS* adaptive algorithm uses this estimate of the gradient to adjust the weights according to:

$$\mathbf{W}(m+1) = \mathbf{W}(m) + \mu(-\hat{\nabla}(m)) \quad , \tag{3.16}$$

which then reduces to the applicable form[15]

$$\mathbf{W}(m+1) = \mathbf{W}(m) + 2\mu\, \xi(m)\, \mathbf{g}(m) \quad , \tag{3.17}$$

where μ regulates the speed and stability of the adaptation process. This filter is implemented by first computing the error between the filter estimate and the desired image at position m. The error is then multiplied by 2μ, the product of which multiplies the image vector function of m given by Eqn. 3.8. This total product is then added to the filter weight vector at point m to give the new,

updated weight vector for point *m+1*. The choice of μ, therefore, is very important. If it is set too large the filter weights will diverge from the optimum values and if it is set too small the convergence will be extremely slow. Figure 3.2 shows two examples of a filter coefficient 'learning curves'. A learning curve

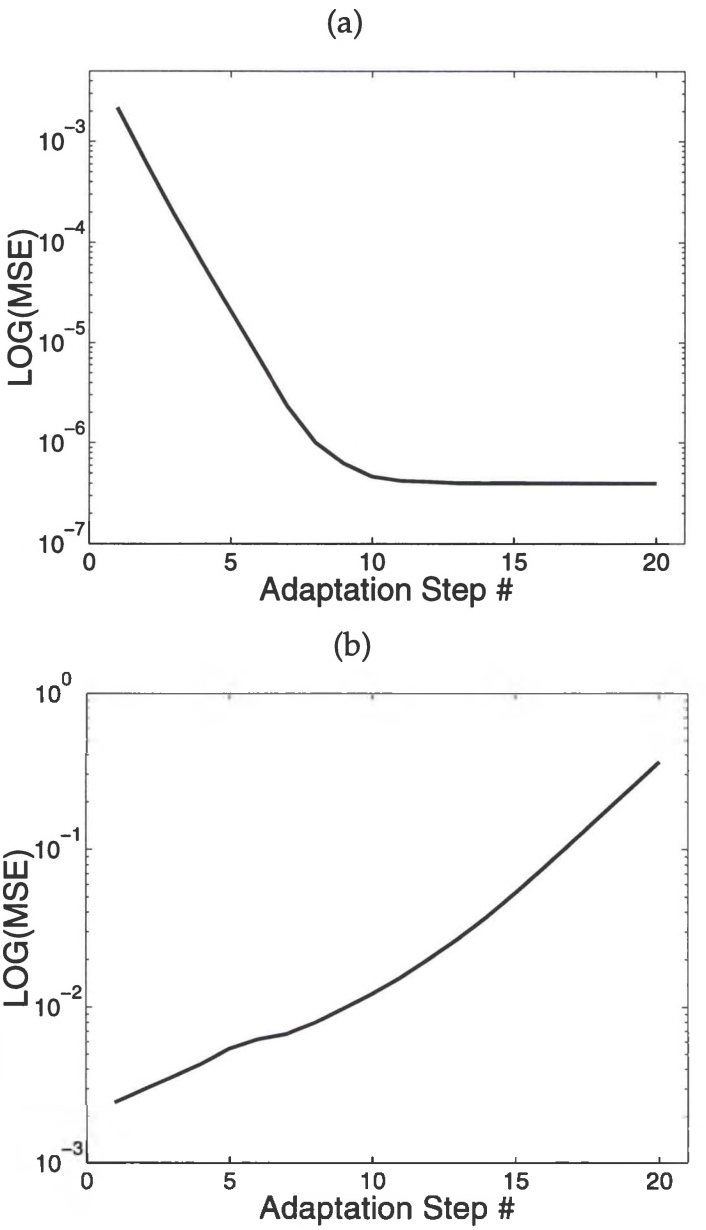

Figure 3.2) *An example of a learning curve for the narrow-band experimental data shown in Figure 4.1 using (a) an optimal choice for the gain factor: 1.0, and (b) a gain factor chosen too large: 1.75. The MSE is measured between the filter estimate and the desired image.*

shows how the value of the *MSE* changes versus iteration (gradient) step. The learning curve in Fig. 3.2(a) is a result of choosing an optimal gain factor μ: fast convergence to minimum *MSE*. If the gain factor is chosen too large, the result is a rapidly diverging *MSE* (Fig. 3.2(b)). There is a method discussed in the literature (see refs. 15,22-25) which can be used to compute a convergence range for the gain factor for a given application In our case, however, trial and error has been found to be the fastest and most useful method. Typical values for the gain factor used for the calculations in this thesis fall in the range of 1.0 to $1x10^{-4}$. Using Eqn. 3.17, the *LMS* algorithm has the advantage of being implemented without squaring, averaging, or differentiation.

3.3 Review of Filtering Process

The *BPM* model developed in Chapter 2 is used to provide an estimate of the beam steerer's finite impulse response (*FIR*). Using the impulse response, samples of either the frequency or spatial domain optimal Wiener filter coefficients can be computed. These filter coefficients have the ability to undo any degradations in the degraded images produced by the *BPM* model. The Wiener filter coefficients, however, are computed using a *constant* noise-to-signal statistic (Γ in Equation 3.7) due to the complexity of noise processes. Since there are various noise factors present in the experimentally degraded images *and*

phase profile inaccuracies in the *BPM* model, the restoration performance of the Wiener filter coefficients on experimental images is limited.

The Wiener filter coefficients, however, can be used as the initial weights for the *LMS* algorithm and reduce the adaptation steps necessary for the *LMS* to achieve minimum mean square error. The *LMS* filter has the advantage over the Wiener filter of being able to adjust each of the filter coefficients as differences are observed between the degraded and desired images. The *LMS* algorithm, however, requires a desired and an degraded training sequence to further adapt the initial Wiener filter coefficients. This limits the use of the *LMS* algorithm to situations where a degraded and desired image are available for training purposes. For the relatively small steer angles studied here, the degraded and desired (unsteered) images contain common information that is used for the training data. In the event that the device is used to steer an entire broad-band field of view, the corresponding desired image may be of an entirely different field of view. This would require the *LMS* filter coefficients to be computed using alternate information, possibly from an impulse response measured in the lab. The characteristics and restoration ability of these filter designs are demonstrated in the following chapters. Computer code can be found for both the Wiener and *LMS* filters in Appendix B.

Chapter 4

Narrow-band Filtering

In this chapter the filtering algorithms are characterized by examining the filter performance on narrow spectral band data. Filter characterization is performed using results from both the *BPM* model and laboratory (experimental) measurements of the beam steering device with comparisons made when applicable. To quantify the behavior of the filtering algorithms there are several different error metrics. The chapter begins with a detailed description of the methods of error measurement.

4.1 Error Metrics

To begin the task of filter performance characterization, methods must first be developed to measure deviations between the filter estimate and the desired result. For the beam steering images, the desired result is typically the unsteered image shifted to the position of the steered image. Due to the small steer angles examined, however, there is no new information steered into the field of view

and so the desired image used in these calculations is the original unsteered image, unshifted.

A complete description of the deviations requires several different forms of error measurement. One of the most commonly used forms of error measurement is that of mean squared error (*MSE*). However, it was discovered that very large values of *MSE* could be computed for visually good filter estimates. The reasons for these large values of *MSE* originate from the relative magnitude and position of certain filter estimates with respect to the desired result. For example, if the filter estimate peak is not located at the exact detector array position of the desired image peak, a large value of *MSE* will be measured. Offsets in the peak positions as small as one or two detector array elements can increase the value of *MSE* by a factor of 10^2. A smaller but equally important effect on the *MSE* is produced when there are large differences between the peak magnitudes of the estimate and the desired result. Since filter operation is based on placing diffraction order energy back at the position of the main steered peak, the amount of this restored energy will vary versus wavelength and/or bandwidth (see Figs. 2.3, 2.4 for example). Different sets of filter coefficients, therefore, place different amounts of energy at the position of the main peak. Quite often a filter estimate is obtained which has a larger (or smaller) peak magnitude than that of the desired result, thus drastically increasing to the *MSE*. To compensate for the possible misconceptions given by the standard

measurement of *MSE* there will be two additional *MSE*-type measurements reported which give a more complete description of the reconstruction deviations. The first of these involves measuring the *MSE after* the peak of the filter estimate has been shifted to the position of the desired peak. This places the filter estimate in the correct output position, if necessary, before the standard *MSE* is measured. The error measure will be referred to as the shifted, mean square error (*SMSE*). The amount of shift between the peak of the estimate and that of the desired is also used as a performance measure. The final error measurement involves normalizing the *shifted* filter estimate and the desired output before the *MSE* is measured. This error measure, referred to as the normalized, shifted mean square error (*NSMSE*), nullifies any magnitude difference between the desired and estimate peak and effectively measures the shape difference between the estimate and the desired. Only differences in the peak and diffraction order width and the magnitude of the diffraction orders will contribute significantly to this error.

To complete the set of performance characterizations a magnitude ratio measurement will be made of the largest remaining sidelobe in the filter estimate to the peak of the filter estimate. This measurement, which is similar to the sidelobe ratio measured in Chapter 2 (Table 2.5), is used to see how effectively a filter can transfer energy from the diffraction orders back into the main peak. The performance ability of the filtering algorithm will be described using these

measurements for both narrow- and broad-band data. It is important to note that one or more of these measurements may not offer significant insight into the filter performance in certain circumstances and thus will not always be reported.

4.2 Theoretical and Experimental Results

In this section, filter performance on narrow-band data, both theoretical and experimental, is examined. Experimental measurements are obtained by placing a 25 μm single slit target in the set-up shown in Figure 2.2. The degraded, steered image of the slit (for a given steer angle and probe wavelength) is used to approximate the response of the beam steering device. Several examples of beam steerer responses are presented to show the effects of grating order dispersion. Figures 4.1 and 4.2 show examples of narrow-band data (degraded and desired) based on different probe wavelength and steer angle, respectively. The data represents a single horizontal slice taken out of the original two-dimensional (2-D) desired and degraded images. The degraded signals show grating-order echoes because the phase profile was blazed for 543 nm and not the other wavelengths. This means that the 2π phase resets (seen in Figure 1.3) are designed for $\lambda = 543$ nm. The relatively low steering efficiencies at the non-design wavelengths require that the restoration process place the sidelobe energy back into the main steered peak. Material dispersion, which would cause additional smearing of the steered, degraded peaks, is absent because the radiation is narrow-band. Restored versions of the degraded single slits in

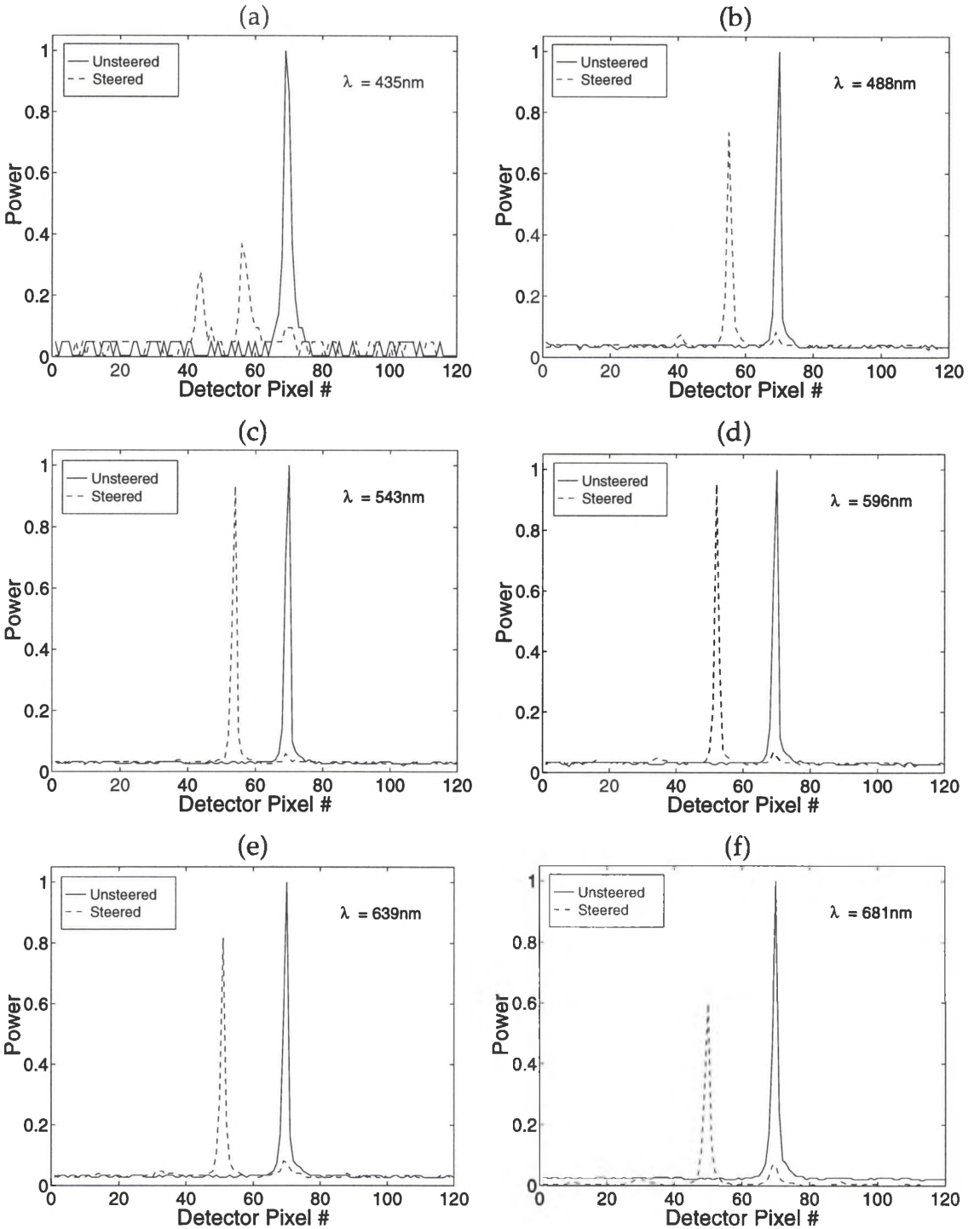

Figure 4.1) *Comparison of narrow-band steered and unsteered 1-D single slit. Results are shown for six different probe wavelengths. The device design wavelength is 543 nm which indicates that the 2π phase resets are designed for λ = 543 nm. Wavelengths of (a) 435 nm, (b) 488 nm, (c) 543 nm, (d) 596 nm, (e) 639 nm, (f) 681 nm, are steered to an angle of 0.024°. Filter restorations of the steered results are presented in Figures 4.3 and 4.4.*

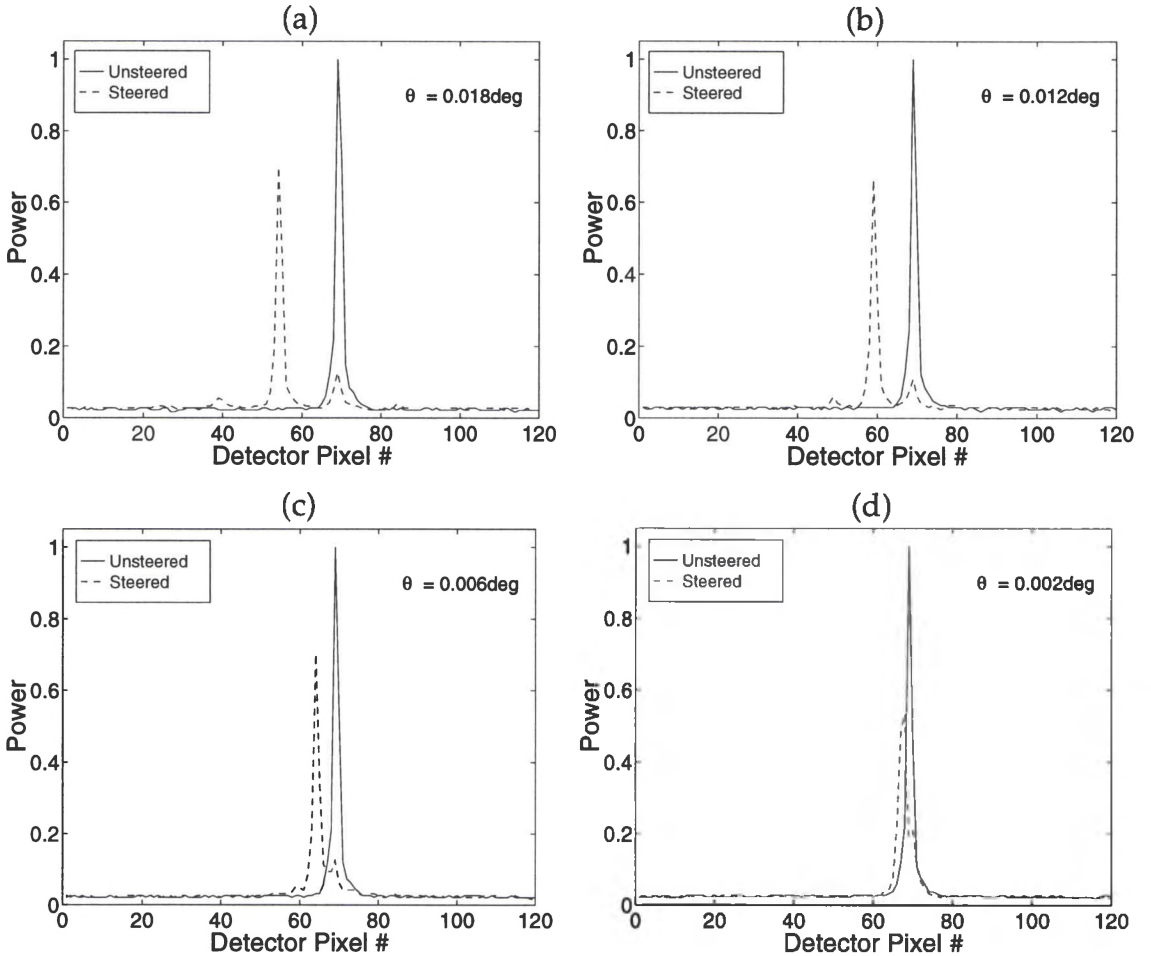

Figure 4.2) *Comparison of narrow-band steered and unsteered 1-D single slit. Results are shown for a probe wavelength of 681 nm steered to four different angles. The steering device was designed for a wavelength of 543 nm. Steer angles of (a) 0.018°, (b) 0.012°, (c) 0.006°, (d) 0.002° are shown. The case of this probe wavelength steered to 0.024° is found in Fig. 4.1(f). Filter restorations are presented in Figures 4.5 and 4.6.*

Figure 4.1 are presented in Figures 4.3 and 4.4. Restorations of the steered single slits in Figure 4.2 are presented in Figures 4.5 and 4.6. The second set of restorations for each set of single slit data (Figs. 4.4 and 4.6) are plotted on a logarithmic scale to give increased detail at the lower magnitude values. The degraded images are restored with both the *LMS* filter coefficients and the Wiener filter coefficients. The *LMS* coefficients are derived from degraded and

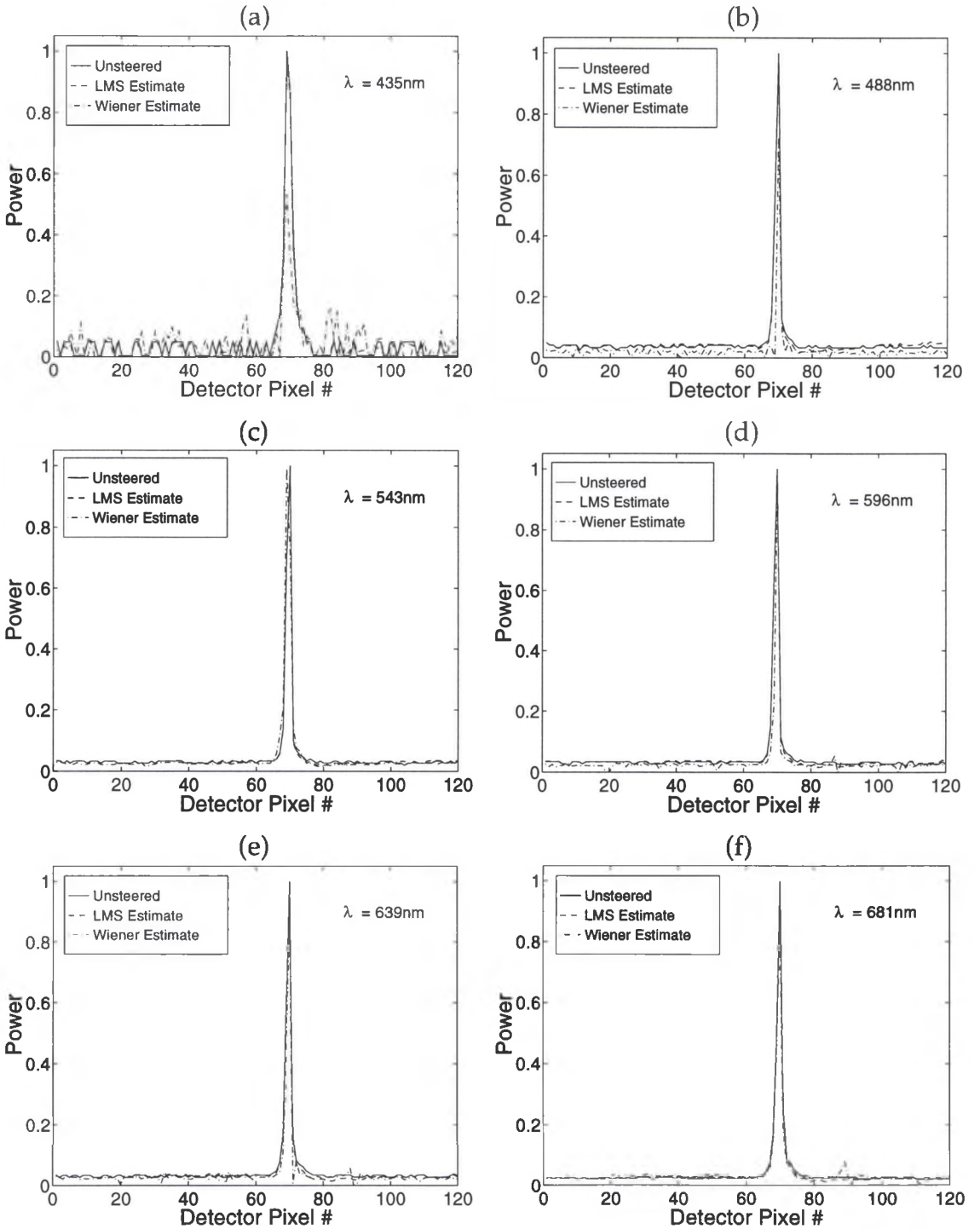

Figure 4.3) *Narrow-band restorations of a steered 1-D single slit. Results are shown for both the LMS filter and the Wiener filter at six different probe wavelengths. Restorations are shown for wavelengths of (a) 435 nm, (b) 488 nm, (c) 543 nm, (d) 596 nm, (e) 639 nm, (f) 681 nm. The original slit was steered to 0.024° for each case. Measurements of MSE are given in Table 4.1. Note that the LMS estimate is almost indistinguishable from the unsteered data in all of the graphs above.*

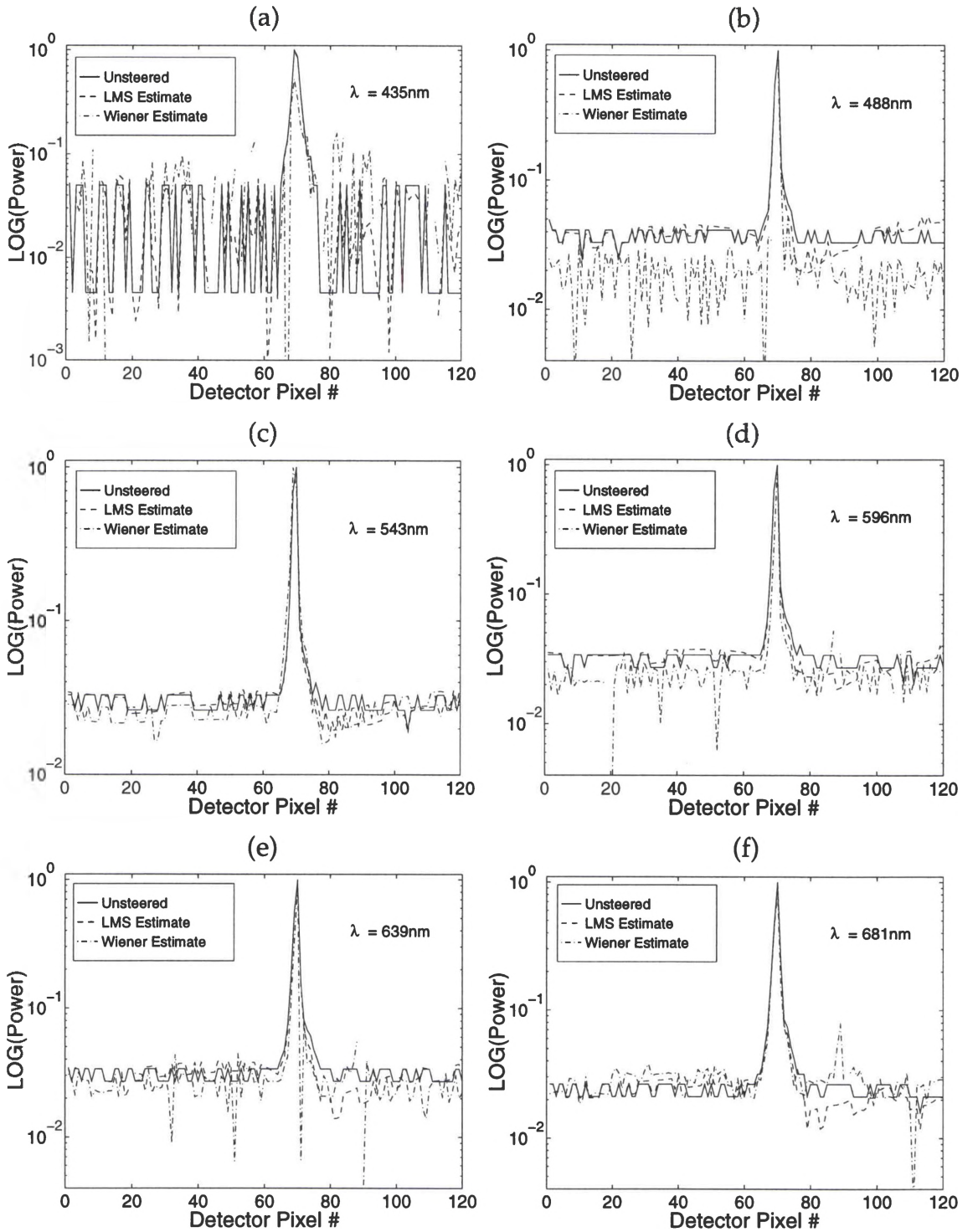

Figure 4.4) *Narrow-band restorations of a steered 1-D single slit. Results are plotted using a logarithmic scale to show greater detail in the lower magnitudes. Restorations are shown for both the LMS filter and the Wiener filter at six different probe wavelengths: (a) 435 nm, (b) 488 nm, (c) 543 nm, (d) 596 nm, (e) 639 nm, (f) 681 nm. The device design wavelength is 543 nm.*

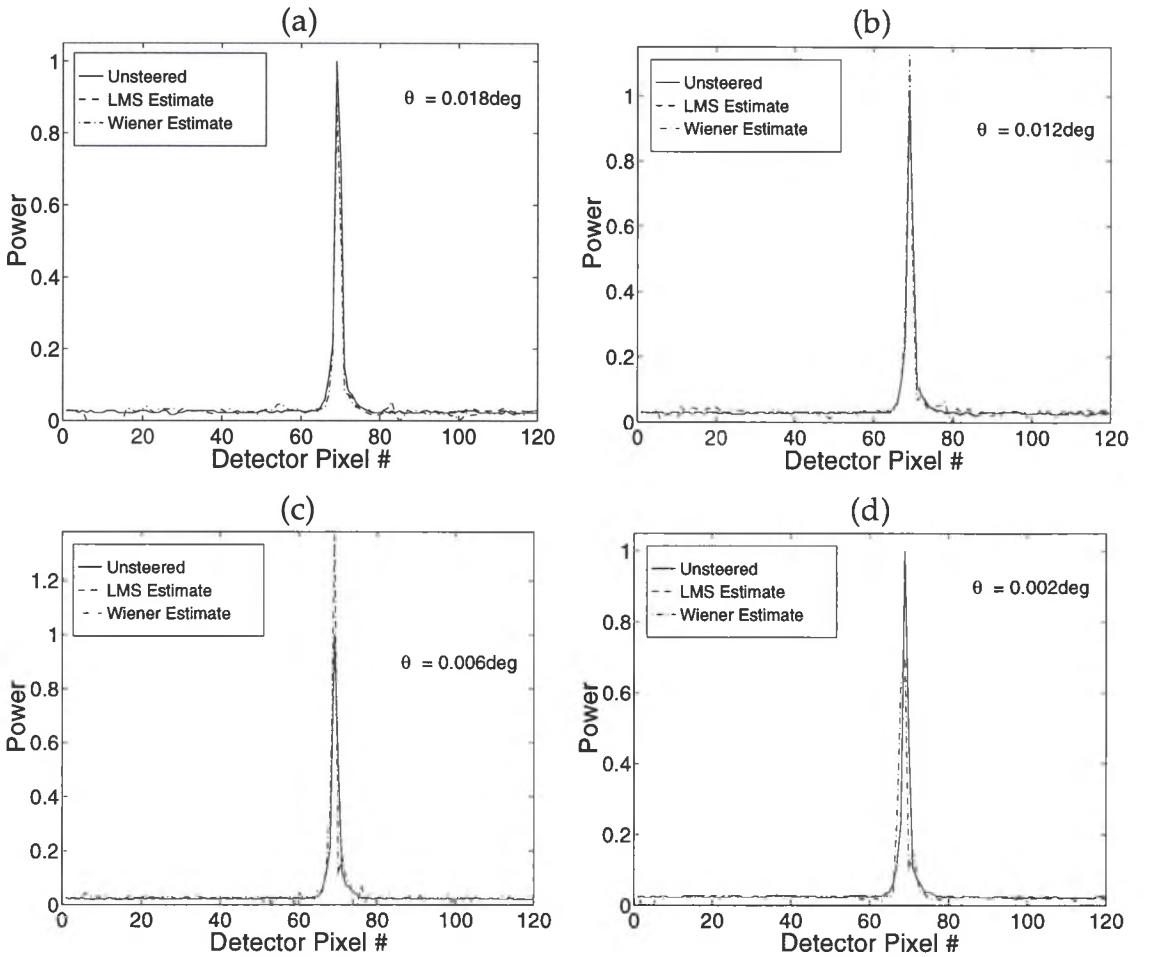

Figure 4.5) *Narrow-band restorations of a steered 1-D single slit. Results are shown for both the LMS filter and the Wiener filter for the 681 nm probe wavelength steered to four different steer angles. Restorations are shown for steer angles of (a) 0.018°, (b) 0.012°, (c) 0.006°, (d) 0.002°. The restoration for this wavelength steered to 0.024° is found in Fig. 4.3(f). Measurements of MSE are given in Table 4.2.*

desired data while the Wiener coefficients are derived from a degraded response generated by the *BPM*. For the degraded and desired (2-D) experimental images, the *LMS* filtering algorithm uses the desired image as the desired result and minimizes the error between it and the filter estimate. To make the filter more robust, the amount of training data is increased by forming long vectors from multiple 1-D slices of the degraded and desired images. Training data could also

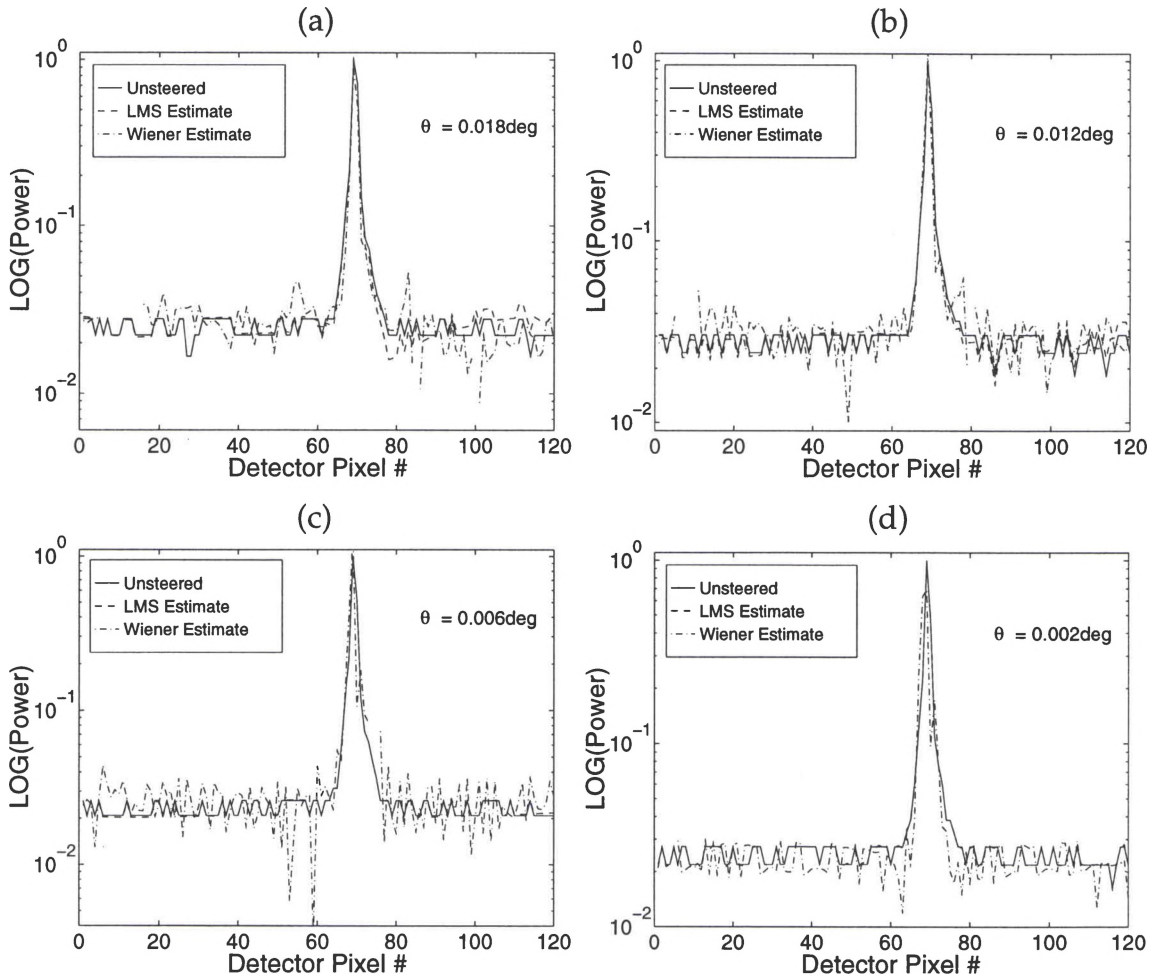

Figure 4.6) *Narrow-band restorations of a steered 1-D single slit. Results are plotted using a logarithmic scale to show greater detail in the lower magnitudes. Results are shown for both the LMS filter and the Wiener filter for a 681 nm probe wavelength steered to four different steer angles. Restorations are shown for steer angles of (a) 0.018°, (b) 0.012°, (c) 0.006°, (d) 0.002°. The restoration for this wavelength steered to 0.024° is found in Fig. 4.4(f).*

be formed by averaging several of the 1-D slices, however, this would result in the partial loss of the statistical noise properties contained in each slice. The multiple vectors represent a larger sample from which the filter coefficients adapt in the presence of statistical variations such as detector nonlinearities and noise. It is the lack of an accurate phase profile and these detector nonlinearities

and noise which are not modeled using the *BPM*, that cause the Wiener filter performance to fall below that of the *LMS*.

Table 4.1 numerically compares the performance of the two restoration filters to the initial error between the degraded and desired peak. The results correspond to the data shown in Fig. 4.3 where a degraded narrow-band probe

Table 4.1) *Filter restoration (Improvement) measurements for the narrow-band single slit image restorations shown in Figure 4.3. The* Improvement Ratio *is a ratio of the baseline mean square error (MSE) to the MSE of the filter estimate. A value greater than one indicates improvement.*

		Improvement Ratio	
λ (nm)	θ_{steer} (°)	LMS Filter	Wiener Filter
435	0.024	131.3	1.3
488	0.024	51.1	0.6
543	0.024	514.5	4.5
596	0.024	85.0	1.25
639	0.024	28.0	1.2
681	0.024	66.8	4.0

wavelength is restored. Note that even though the amount of improvement by the *LMS* filter varies greatly versus wavelength the estimate is visually excellent (Fig. 4.3) for each wavelength. The *Improvement Ratio* is a ratio of the baseline mean square error (*MSE*) between the degraded and desired image to the *MSE* of the filter estimate. An improvement ratio greater that one indicates the filter has done some improvement, while a value less than one indicates that the filter is adding more degradations than it is removing. Keep in mind, however, that the drawbacks of using *MSE* as an error measure also appear in the improvement ratio. For example, if a comparison is made between the degraded image in Figure 4.1(b) and the Wiener filter restoration in Figure 4.3(b), it is observed that

the filter effectively gets rid of the two main sidelobes in the degraded image yet only has an improvement factor of 0.6. Note that before the error between the degraded and the desired (unsteered) data is measured, the degraded image is shifted to the position of the desired image. This shift will effectively 'undo' the steering and align the two images allowing a *baseline MSE* to be measured. The results in Table 4.1 show the excellent restoration ability of the *LMS* algorithm. Wiener filter performance, though inferior to the *LMS*, does offer slight improvement in the estimate when compared to the initial baseline error.

Table 4.2 demonstrates a similar trend in the restoration ability of each filter versus steer angle. The only noticeable difference is the ability of the *LMS* algorithm to perform increasingly better restoration as the steer angle is decreased. This is due in part to the smaller angular spread of the diffraction order energy as the steer angle is decreased. This phenomena can also be attributed to the finite resolution of the CCD detector used to capture the images. As the steer angle decreases, the far-field diffraction orders move closer to the main steered peak (Fig. 4.2) until a point is reached ($\cong 0.007°$) where they appear

Table 4.2) *Filter restoration (Improvement) measurements for the narrow-band single slit image restoration in Figure 4.5 based on a variable steer angle. The baseline value is the MSE between the steered and unsteered.*

Wavelength	Steer Angle	**Improvement Ratio**	
λ (nm)	θ_{steer} (°)	LMS Filter	Wiener Filter
681	0.024	66.8	4.0
681	0.018	133.1	2.7
681	0.012	323.5	1.9
681	0.006	9190.0	0.4
681	0.002	13700.0	0.9

to blend together with the main peak. At this point, the degraded images appear to contain more of a smearing or spreading effect compared to a sidelobe echoing effect at the detector. The *LMS* filter coefficients can adapt to this smearing effect much quicker, and with fewer significant coefficients. Since all the restoration filters used on Figs. 4.1 and 4.2 were computed using the same step size ($\mu = 1.0$ in Equation 3.22), number of filter coefficients (401), and number of adaptation steps (200), the *LMS* filter coefficients derived for the smaller steer angles will reach a better performance level given the above constraints. A graphical description of the LMS filter improvement ratio versus both probe wavelength and steer angle is shown in Figure 4.7. The inferior performance of Wiener filter is a result of both real-life imperfections in the device's phase profile which are not present in the idealized *BPM* model and the noise to signal ratio power constant in the Wiener filter equation. The noise to signal power constant (Γ in

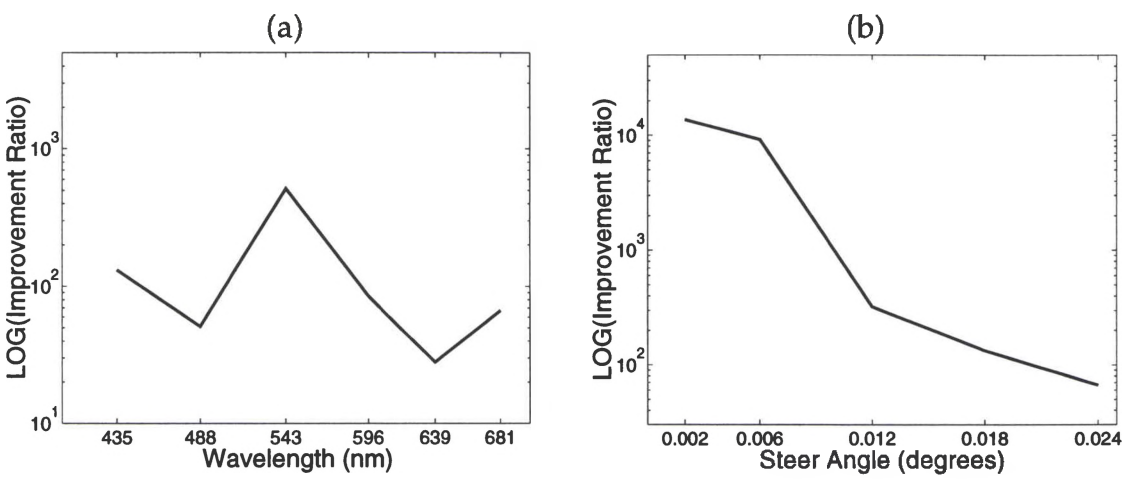

Figure 4.7) *Graphical view of LMS filter improvement versus (a) probe wavelength and (b) steer angle. Numerical results are found in Tables 4.1 and 4.2 respectively.*

Equation 3.12), which is an approximation to the noise and signal statistics, is found by measuring the total power and the variance in a 'dark' part of the experimental image. The term 'dark' refers to a portion of the detector not exposed directly to incident light and thus measures only background radiation. The variance is effectively the noise power in that portion of the image and the total power is then the noise power plus signal power. Signal power is then found by subtracting the noise from the total, giving a noise to signal ratio of approximately 0.001 for the experimental narrow-band images. Since the value of the noise to signal ratio is small, there is little difference between the Wiener filter coefficients computed using Equation 3.12 and the inverse filter result in Equation 3.2. This small ratio is due to the controlled laboratory conditions in which the images were captured.

Figure 4.8 shows the similarities between the Wiener filter coefficients derived from the *BPM* model and the optimal *LMS* filter coefficients found with the experimental training data. The *BPM*-derived filters give an improved starting point for the *LMS* algorithm, thus reducing the number of adaptation steps. It is often unnecessary, however, in the case of single slit data, to begin with the Wiener filter coefficients due to the small number of adaptation steps needed by the *LMS* algorithm. The single slit images examined here, both narrow-band and broad-band, do not include a significant amount of noise because of the controlled laboratory conditions in which they were measured.

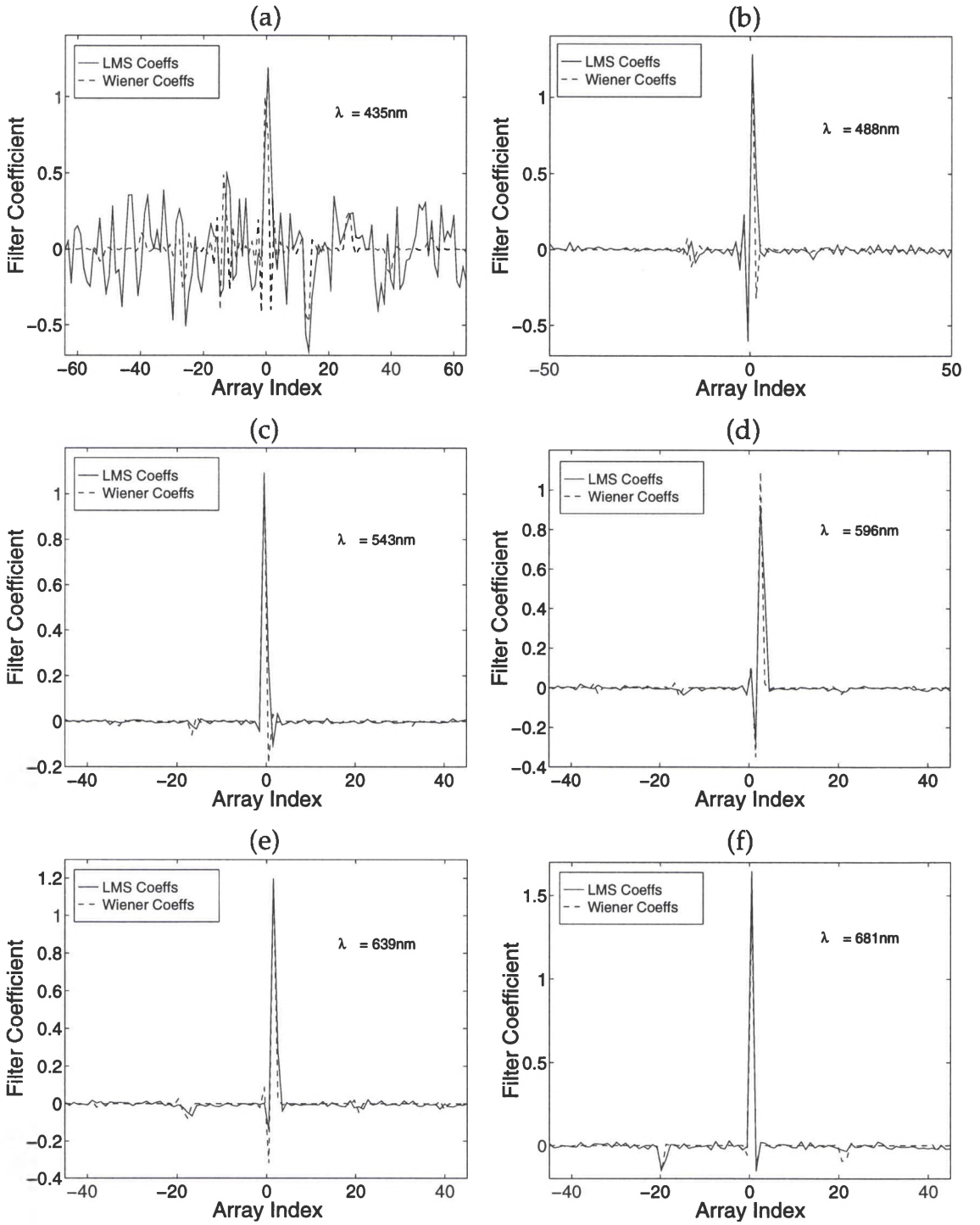

Figure 4.8) *Each plot shows the optimized LMS filter coefficients and Wiener filter impulse response coefficients for one of six probe wavelengths: (a) 435 nm, (b) 488 nm, (c) 543 nm, (d) 596 nm, (e) 639 nm, (f) 681 nm. The LMS coefficients are derived from the experimental data. The Wiener filter impulse response is derived from BPM model using a noise to signal constant of 0.001. The filter coefficients are computed for data originally steered to 0.024°.*

The small steer angles examined (0.002° - 0.024°) also give results which typically show small amounts of unwanted diffraction order energy. For these reasons the *LMS* algorithm can adapt to a greater degree of improvement in a shorter amount of time using fewer coefficients for steered images with less degradations. Improvements in the *MSE* of the restoration, as compared to baseline measurements, of 10^2 can be obtained in as few as 10 to 15 adaptation steps.

To further test the ability of the *BPM* to accurately predict impulse responses of the beam steering device, it is used to model 682 nm light steered using a phase ramp designed for λ=543 nm. The impulse responses were computed for light steered to a range of different steer angles (0.002° - 0.024°). The Wiener filter coefficients are calculated from the impulse response at each steer angle and then compared to *LMS* filter coefficients computed using measured, experimental data. The *LMS* and Wiener filter coefficients are shown in Figure 4.9 for six of the sixteen steer angles examined. Note that the primary features of the filter coefficients displayed in Figures 4.8 and 4.9 are a central lobe corresponding to the main steered peak and two negative lobes corresponding to the largest diffraction orders (see Figs. 4.1 and 4.2). When steering to smaller angles the reset spacing Λ increases. Equation 1.6 then implies that the angular spacing between grating orders will decrease and thus reduce the peak-to-echo

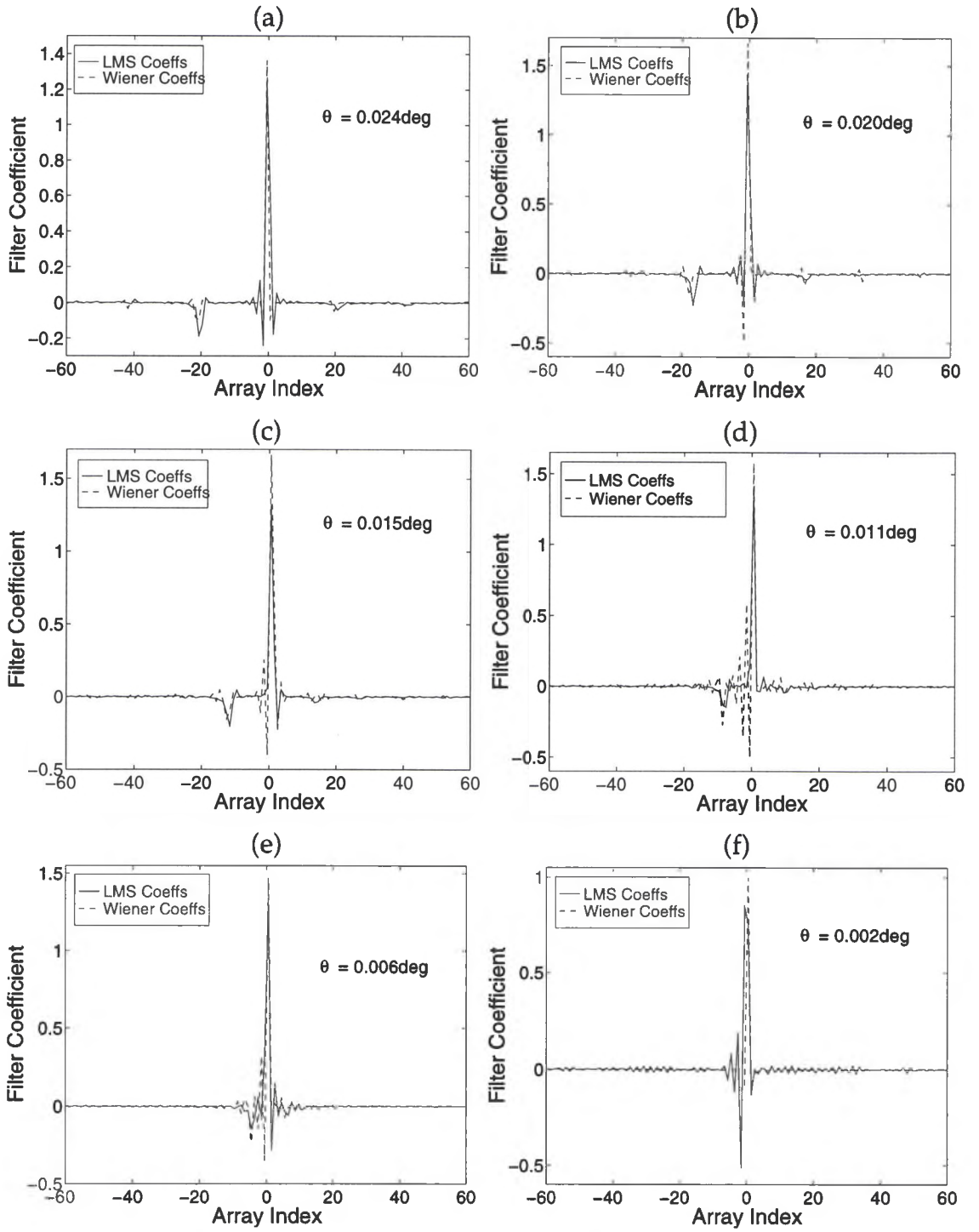

Figure 4.9) *Each plot shows the optimized LMS filter coefficients and Wiener filter impulse response coefficients for one of six steer angles: (a) 0.024°, (b) 0.020°, (c) 0.015°, (d) 0.011°, (e) 0.006°, (f) 0.002°. These are measured for a probe wavelength of 682 nm with a design wavelength of 543 nm. The LMS coefficients are derived from the experimental data. The Wiener filter impulse response is derived from BPM model.*

separation in the far-field. This will reduce the spacing between the filter peak and each of the two main negative bumps (sidelobes). A comparison is made of the magnitude and position of these negative bumps in the *LMS* coefficients to those in the Wiener filter coefficients over the range of possible steer angles. Figure 4.10(top) shows excellent agreement between the peak to filter sidelobe separation distance in the *BPM*-derived Wiener coefficients and the experimentally determined *LMS* coefficients. If the sidelobe to filter peak

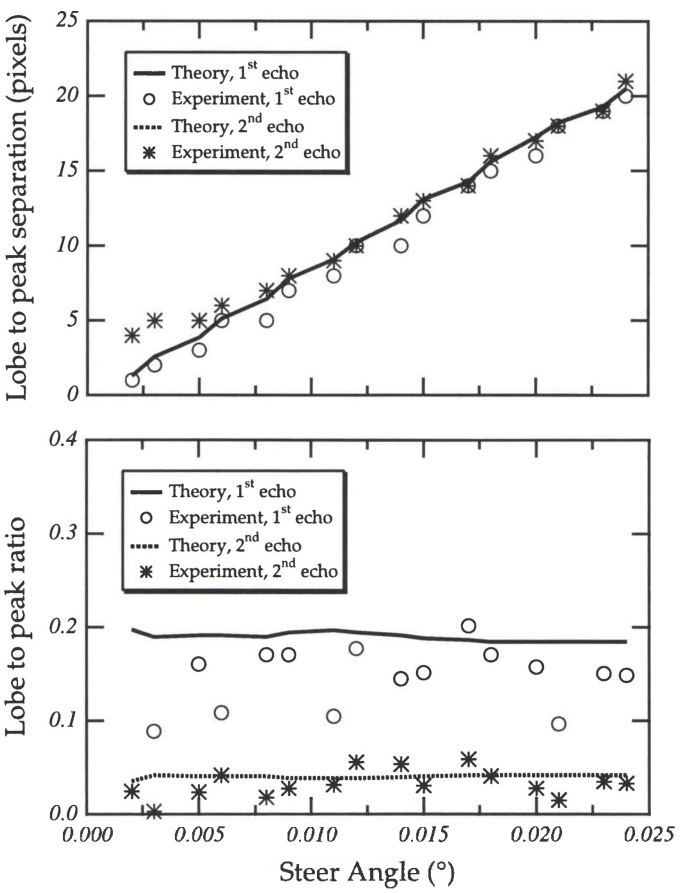

Figure 4.10) *(top) Peak-to-sidelobe filter coefficient separation in pixels and (bottom) sidelobe-to-peak filter coefficient ratio from the theoretical model and experimental measurements. Filter coefficients are computed for a 682 nm probe wavelength steered with a device designed for 543 nm. The probe wavelength was steered to sixteen different angles in the range of 0.002° - 0.024°. Filter coefficients for six of these angles are found in Figure 4.9.*

magnitude ratio is measured, reasonable agreement between theoretical model and experimental results is also obtained. It is important to note that these measurements are completely analogous to the measurements of peak-to-sidelobe separation distance and sidelobe-to-peak ratio made on the steered images in Chapter 2. These results further demonstrate the accuracy of the *BPM* in computing the impulse response of the beam steerer for different phase ramps.

4.3 Narrow-band Filter Robustness

The final test of the narrow spectral band filtering algorithm is a measurement of the *robustness* of the narrow-band filters. To measure how robust a filter is involves examining how the filter performs when applied to images degraded by different steering conditions (probe wavelength and/or steer angle). For the case of narrow-band data it is discovered that filter performance is definitely not robust. Attempting to restore a degraded steered image with filter coefficients derived on different steering conditions will often cause the filter output to contain more degradations than the original steered image. Changes in image data as small as 5 nm or 0.001° will require an entirely new set of filter coefficients for effective restoration. An example of this phenomena is shown using the filter coefficients in Fig. 4.9 based on a design wavelength of 543 nm, a probe wavelength of 682 nm, and sixteen different steer angles. The results in Figure 4.11(a,b) show how the MSE of the filter estimate varies as the steered data at each steer angle is restored with a filter designed for

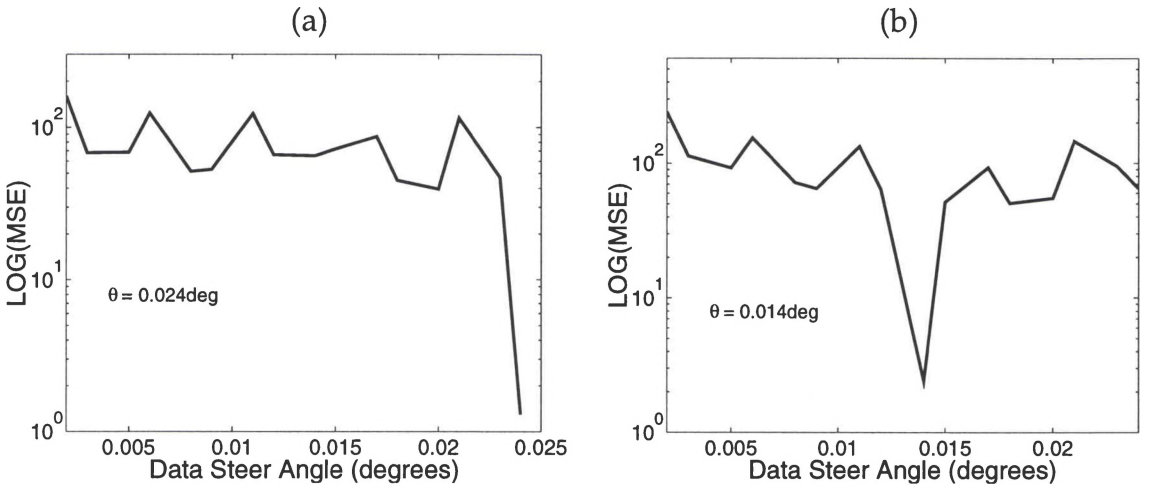

Figure 4.11) *(a) Filter restoration MSE of an optimal filter designed for a 682 nm probe wavelength steered to 0.024° through a device with the 2π phase resets designed for 543 nm. (b) Filter restoration MSE of an optimal filter designed for a 682 nm probe wavelength steered to 0.014° through a device with the 2π phase resets designed for 543 nm.*

0.024° and 0.014°, respectively. Several restoration examples are given in Figure 4.12 which demonstrate the behavior of the 0.014° filter on data steered to 0.012°, 0.014°, and 0.015°. Notice that attempting to restore data with a steer angle different by as little as 0.001° results in a sub-optimal restoration (Figure 4.12(d)). These results show that the restoration ability of a given narrow-band filter is almost strictly limited to the original data for which it was designed. This is due to the direct correlation between the filter coefficients and the relative positions of the diffraction orders. If a set of filter coefficients assumes there is diffraction order energy in a position where diffraction order energy does not exist, the filter will attempt to remove the nonexistent energy and thus fail to remove the true diffracted energy (Figure 4.12(b,c)).

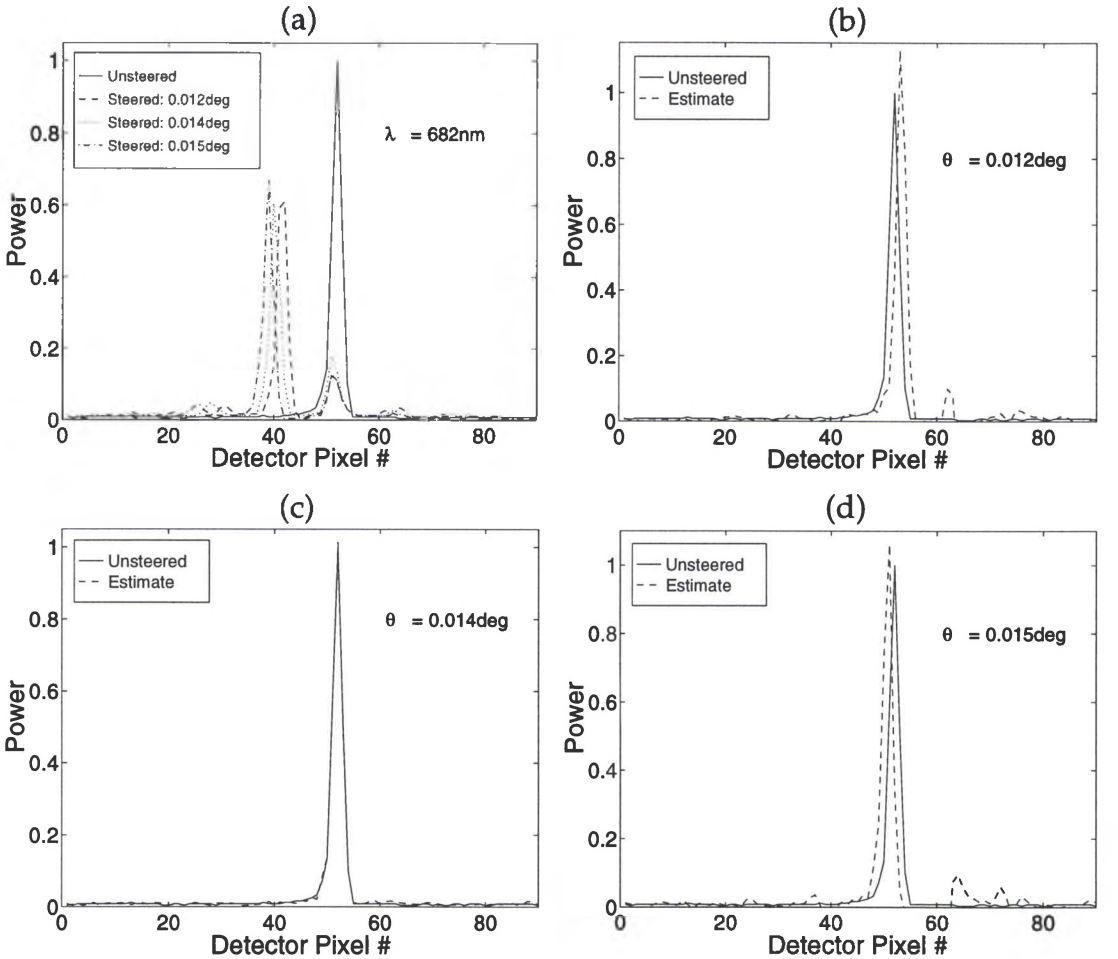

Figure 4.12) *Filter restoration example using filter coefficients derived from 682 nm probe wavelength steered to 0.014°. (a) Data steered to 0.012°, 0.014°, and 0.015° and an unsteered image. Restored results of (b) 0.012° (c) 0.014° (d) 0.015° steered data using a 0.014° filter.*

To repeat this analysis versus a changing wavelength, steered data and filter coefficients must be computed using the BPM model due to a lack of experimental data. This analysis is then repeated after changing the angular full-width at half-maximum (*FWHM*) of the original unsteered data. The *FWHM* of the unsteered slit, both experimental and theoretical, determines the number of detector pixels over which the steered and unsteered intensity patterns span. A very narrow unsteered intensity pattern (4 or 5 pixels) results is an equally

narrow steered intensity pattern. As a result, if the filter estimate is not located at the correct (unsteered) position a large value of *MSE* will be computed, even for shift errors as small as 1 or 2 pixels. If the *FWHM* of the unsteered intensity pattern is widened, the same filter estimate shifted by 1 or 2 pixels will slightly overlap the unsteered pattern resulting in a lower *MSE*. This behavior is demonstrated in Figure 4.13 where a filter developed for a probe wavelength of 650 nm is used to restore steered probe wavelengths between 500-700 nm at 10nm intervals. This data is modeled using a device with the 2π phase resets optimized for 543 nm. There is a factor of 10 difference between the FWHM of the "Thin FWHM" (0.001° angular FWHM) data and the "Thick FWHM" (0.01° angular FWHM) data. The analysis indicates that a difference in the peak *FWHM*

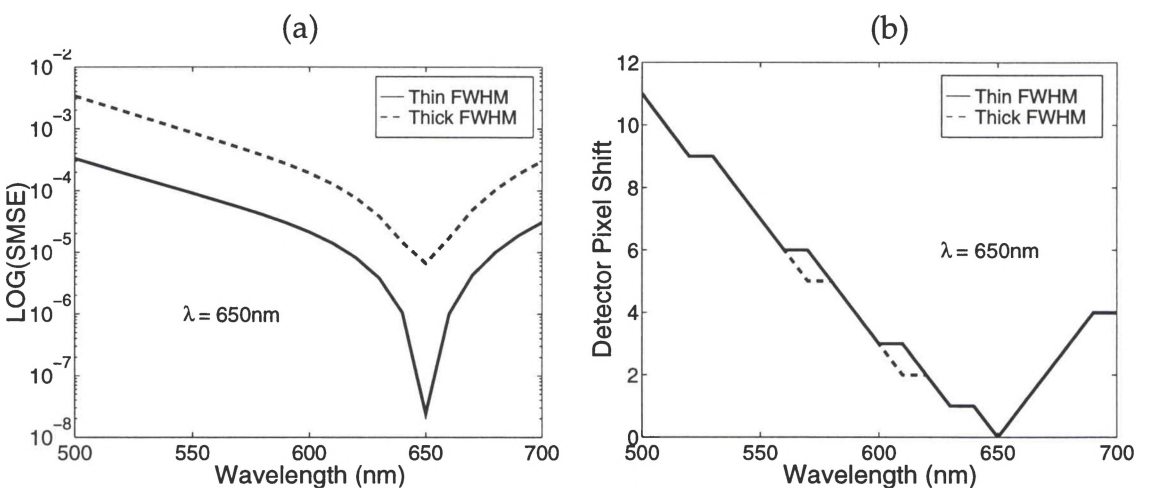

Figure 4.13) *(a) Filter restoration MSE of a filter designed for a probe wavelength of 650 nm used to restore steered results of probe wavelengths in the range 500-700 nm. (b) The pixel shift between the filter estimates and the unsteered data for two different values of FWHM. The data labeled "Thin FWHM" indicates the unsteered image has an angular FWHM of 0.001° and the data labeled "Thick FWHM" has an angular FWHM of 0.01°.*

of the data gives filters which appear more robust for the same amount of pixel shift (Fig. 4.13(b)). The fact remains, however, that quality narrow spectral band filter performance is limited to degraded images captured under identical steering conditions.

4.4 Conclusion

In this chapter, the image restoration ability of the Wiener Filter and the *LMS* adaptive filtering algorithm has been demonstrated on narrow spectral band data. The filtering algorithms effectively remove much of the grating dispersion introduced when steering a monochromatic beam of light with a liquid crystal beam steering device. Results show that *LMS* filter coefficients derived from experimental steered and unsteered images can remove a large portion of the diffraction order energy and place it at the position of the main peak. These filter restorations improve the image, compared to the uncorrected steered image, by reducing the *MSE* up to a factor of 10^3. Wiener filter coefficients derived from the *BPM* model did not appear to significantly improve on degraded images in terms of *MSE*, however, but did offer an excellent starting point from which the *LMS* coefficients could begin adaptation.

The results in this chapter also indicate that narrow-band image restoration filters are typically not robust. Though the filtering algorithms do perform very well on data with the corresponding steer angle and wavelength, they do not perform well in other situations due to the changing positions of the diffraction

orders. If the diffraction orders of a steered image are not at the position a given filter expects them to be, the diffraction orders in the steered image will not be restored. It was discovered that changing the steer angle or wavelength of the steered image by increments as small as 0.001° or 5 nm requires a completely new set of filter coefficients for successful restoration. In Chapter 5, however, it is demonstrated that broad-band restoration filters do exhibit some degree of robustness.

Chapter 5

Broad-band Filtering

In this chapter, filtering algorithm characterization is continued by examining the filter performance on broad spectral band data. These characterizations are of particular interest for broad-band field-of-view steering applications where the image degradation introduced by the dispersion of the non-design wavelengths becomes more severe. Each wavelength within the bandwidth will experience material and grating dispersion as the beam is propagated through the device, thus adding together to form a blurred (or smeared) and echoed image at the detector plane. The restoration filters, therefore, must compensate for the energy in the diffraction orders *and* the additional smearing introduced by the broad-band radiation.

5.1 Theoretical and Experiment Results

Impulse response characterizations of the *BPM* model and experimental results begin in this section by examining the restoration of a steered 25 μm single slit illuminated with a varying (visible) bandwidth of light. The accessible experimental bandwidths were limited by the available highpass and lowpass

filters. Measurements of experimental steered images are made using four different bandwidths: 400-700 nm, 450-650 nm, 500-600 nm, and 600-700nm. Degraded and desired images at these bandwidths are also predicted using the *BPM* model an incoherently adding together narrow-band results calculated at every 10 nm within the bandwidth which were individually weighted with a blackbody curve of the experimental white light source (2880 K). The desired (unsteered) and degraded (steered) *BPM* images are then used as training data for computing the theoretical *LMS* filter coefficients. To accurately create a broad-band model, the narrow-band degraded and desired images which are summed together have a finite spot size (angular *FWHM* of 0.05°). To compute the optimal set of filter coefficients, the *LMS* algorithm is used to compute the filter coefficients using the *BPM* data as training data. The effect of the spot size on theoretical broad-band modeling is examined later in the chapter.

Figures 5.1 and 5.2 show examples of experimental broad-band steered (degraded) and unsteered (desired) data based on different bandwidths and steer angles, respectively. This data represents a single horizontal slice taken out of the original 2-D steered and unsteered images. The steered results show both diffraction grating sidelobes and smearing. Smearing effects are one of the most

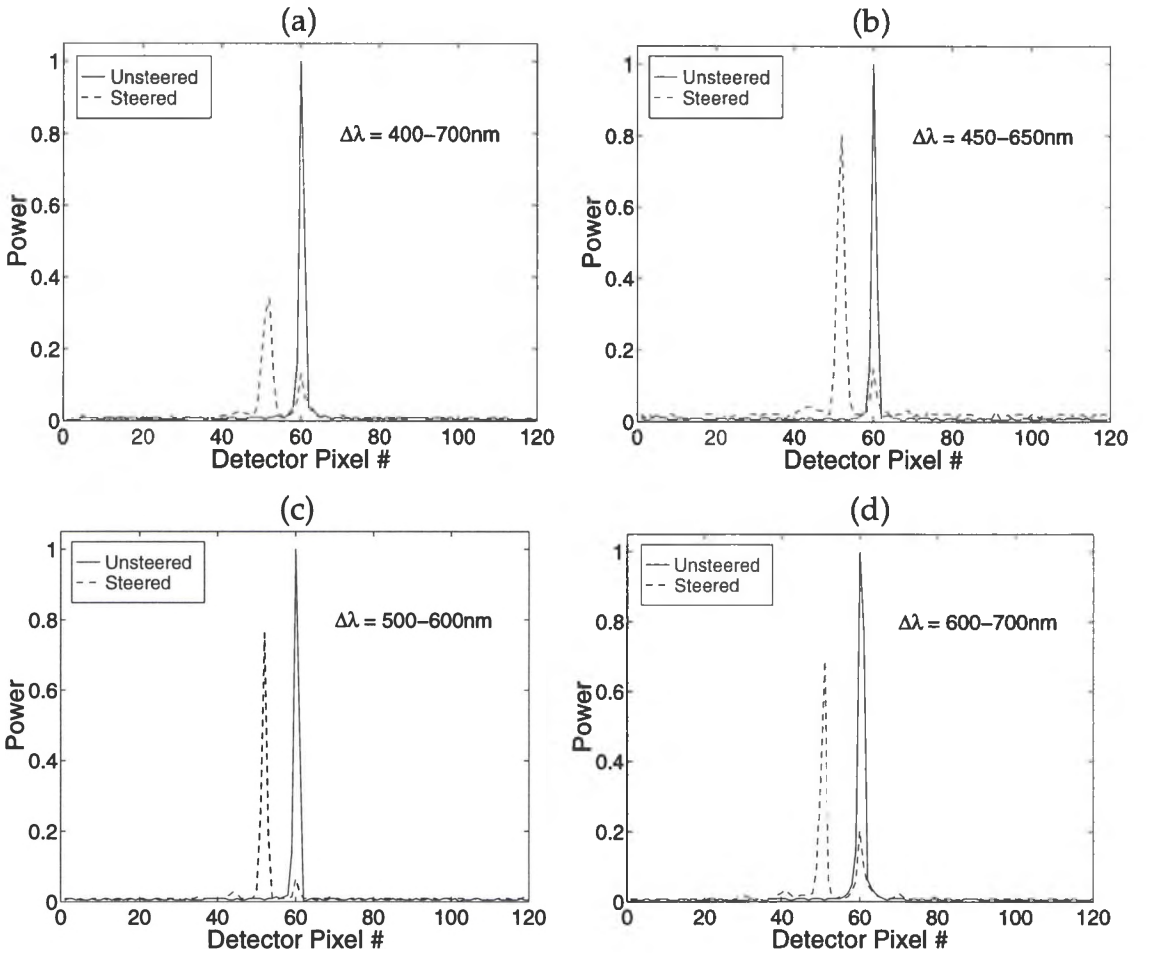

Figure 5.1) *Comparison of experimentally measured broad-band steered and unsteered, 1-D images of a single slit. Results are shown for four different bandwidths. Bandwidths of (a) 400-700 nm, (b) 450-650 nm, (c) 500-600 nm, (d) 600-700 nm, are steered to an angle of 0.024°. The design wavelength of the device was 543 nm. Filter restorations of the steered results are presented in Figures 5.3 and 5.4.*

notable differences between the narrow-band (Figs. 4.1 and 4.2) and broad-band steered images. Since each wavelength in the broad-band bandwidth is steered to a slightly different angle (Eqn. 1.6) and experiences a slightly different Δn (Eqn. 1.3), the steered peak appears to be smeared or widened when compared to the unsteered peak. This has a direct effect on the calculation of filter coefficients

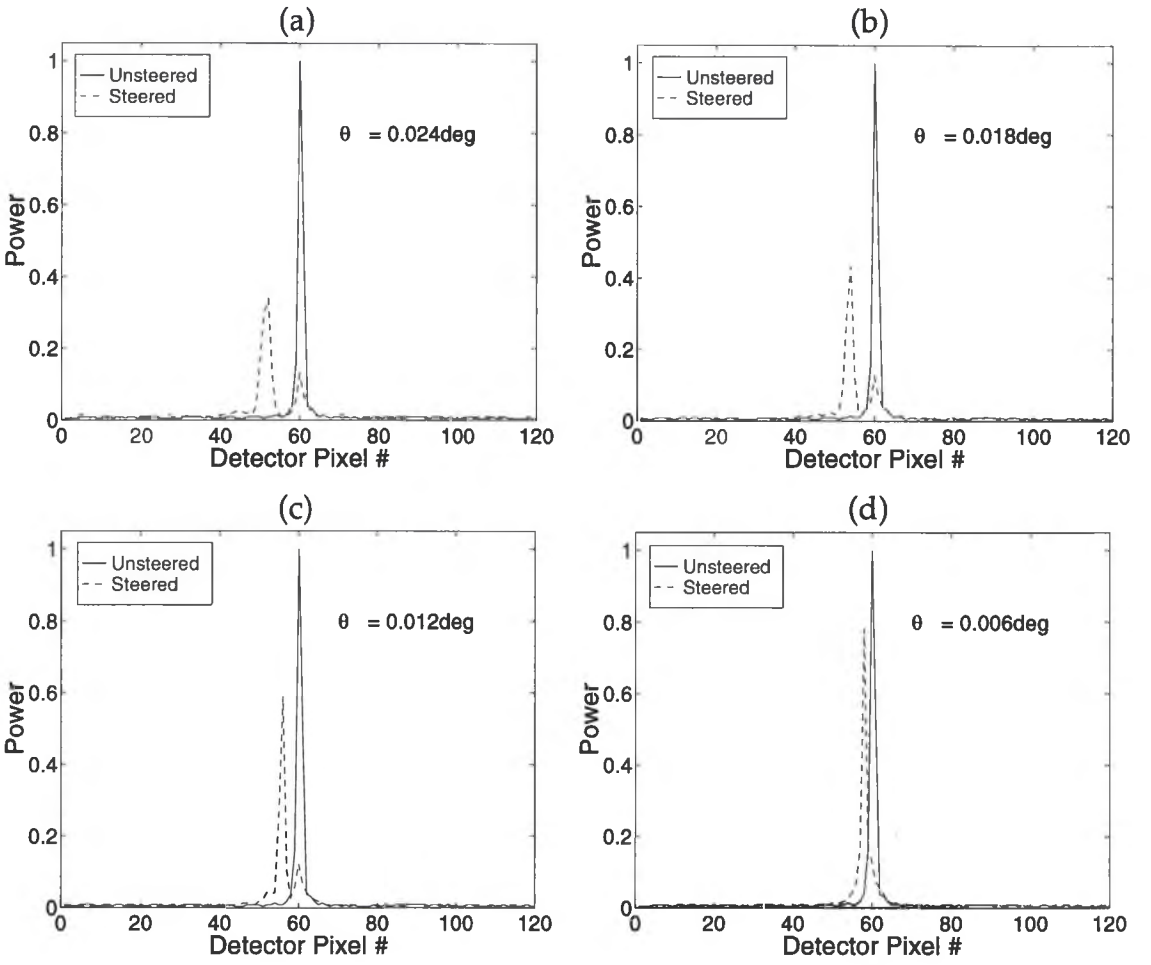

Figure 5.2) *Comparison of experimentally measured broad-band steered and unsteered, 1-D images of a single slit. Results are shown for a bandwidth of 400-700 nm steered to four (4) different angles. The steering device was designed for a wavelength of 543 nm. Steer angles of (a) 0.024°, (b) 0.018°, (c) 0.012°, (d) 0.006° are shown. Filter restorations are presented in Figures 5.5 and 5.6.*

as more significant (non-zero) coefficients are needed to restore the different degradations.

Filter restorations for the degraded, steered images in Figure 5.1 are given in Figures 5.3 and 5.4. The results in Fig. 5.4 are presented on a logarithmic scale to show the differences in the lower magnitudes. Restorations for the images in Figure 5.2 are given in Figures 5.5 and 5.6, the second of which again presents

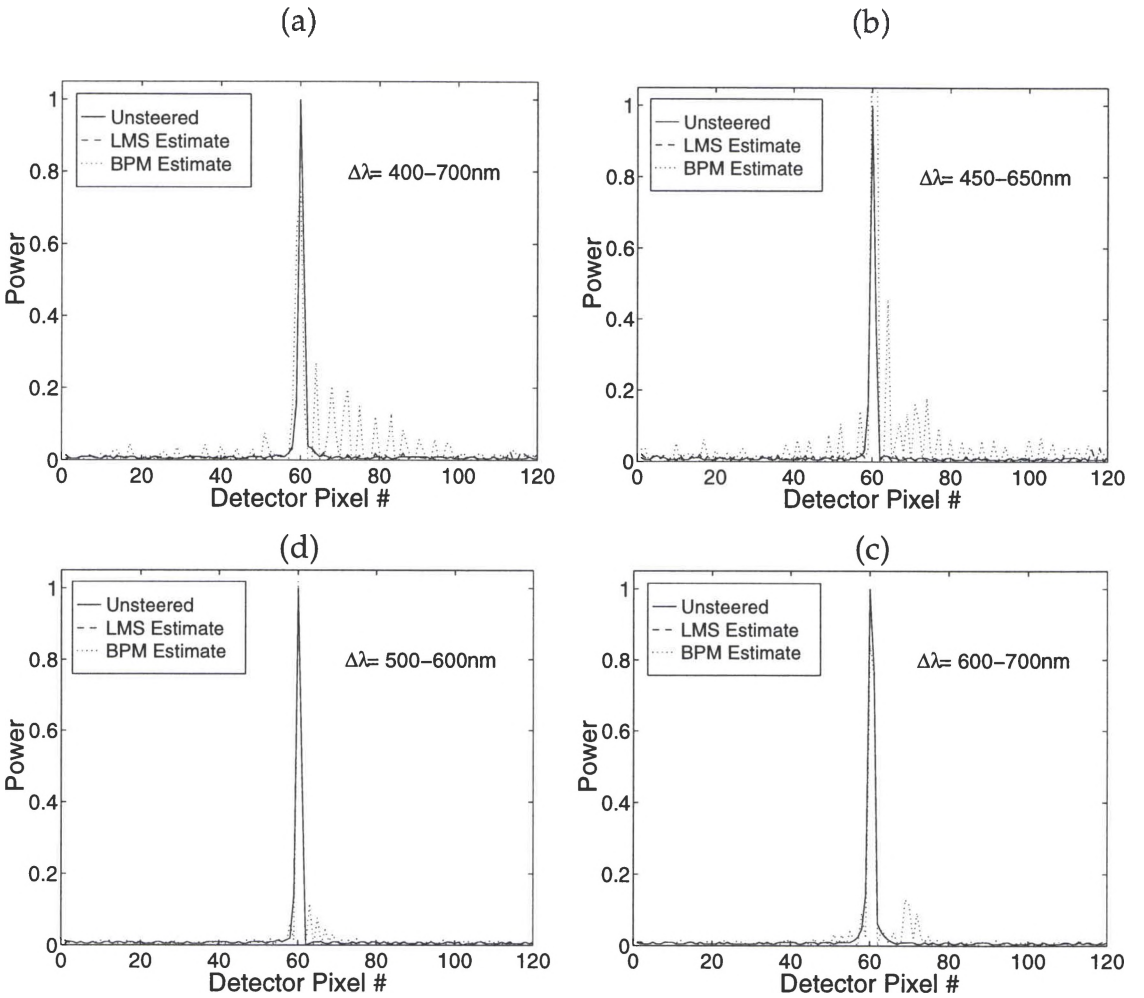

Figure 5.3) *Broad-band restorations of a steered 1-D single slit. Results are shown for both the experimental LMS filter and the BPM-derived LMS filter at four different bandwidths. Restorations are shown for bandwidths of (a) 400-700 nm, (b) 450-650 nm, (c) 500-600 nm, (d) 600-700 nm. The original slit was steered to 0.024° for each case. Measurements of MSE are given in Table 5.1.*

Table 5.1) *Filter restoration (Improvement) measurements for the broad-band single slit image restorations shown in Figure 5.3. The* Improvement Ratio *is a ratio of the baseline mean square error (MSE) to the MSE of the filter estimate. A value greater than one indicates improvement.*

		Improvement Ratio	
Δλ (nm)	θ_{steer} (°)	LMS Filter	BPM Filter
400-700	0.024	157.7	0.9
450-650	0.024	46.3	0.2
500-600	0.024	1086.0	3.8
600-700	0.024	3057.0	8.2

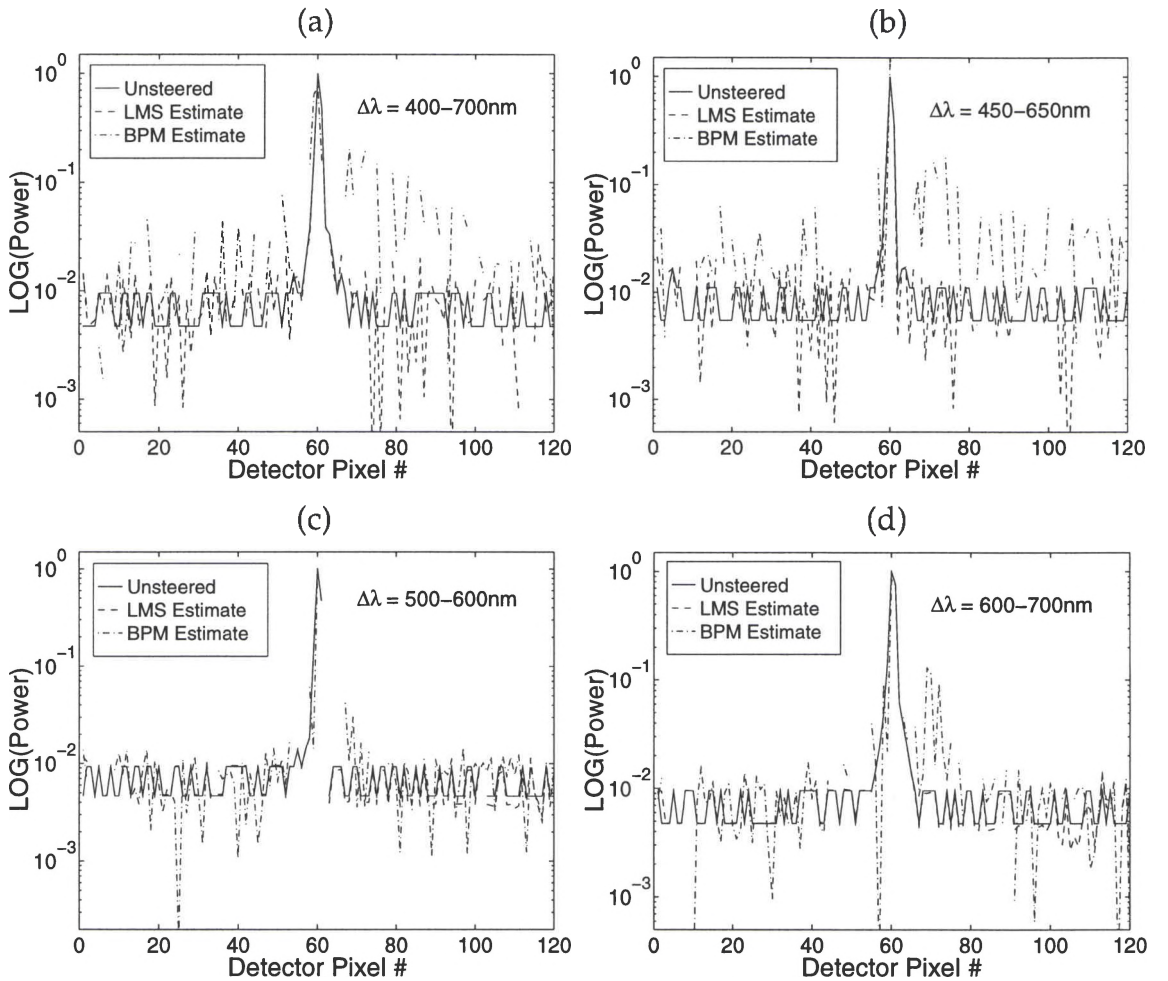

Figure 5.4) *Broad-band restorations of a steered 1-D single slit. Results are plotted using a logarithmic scale to show greater detail in the lower magnitudes. Results are shown for both the experimental LMS filter and the BPM-derived LMS filter at four different bandwidths. Restorations are shown for bandwidths of (a) 400-700 nm, (b) 450-650 nm, (c) 500-600 nm, (d) 600-700 nm. The original slit was steered to 0.024° for each case.*

restorations on a logarithmic scale to increase detail in the lower magnitudes. The result labeled "LMS Estimate" is the filter estimate determined by the experimental *LMS* filter coefficients. As in the narrow-band case, these *LMS* coefficients were trained on data consisting of multiple 1-D slices of the experimental steered and unsteered images. These 1-D vectors represent a larger sample from which the filter coefficients can adapt in the presence of statistical

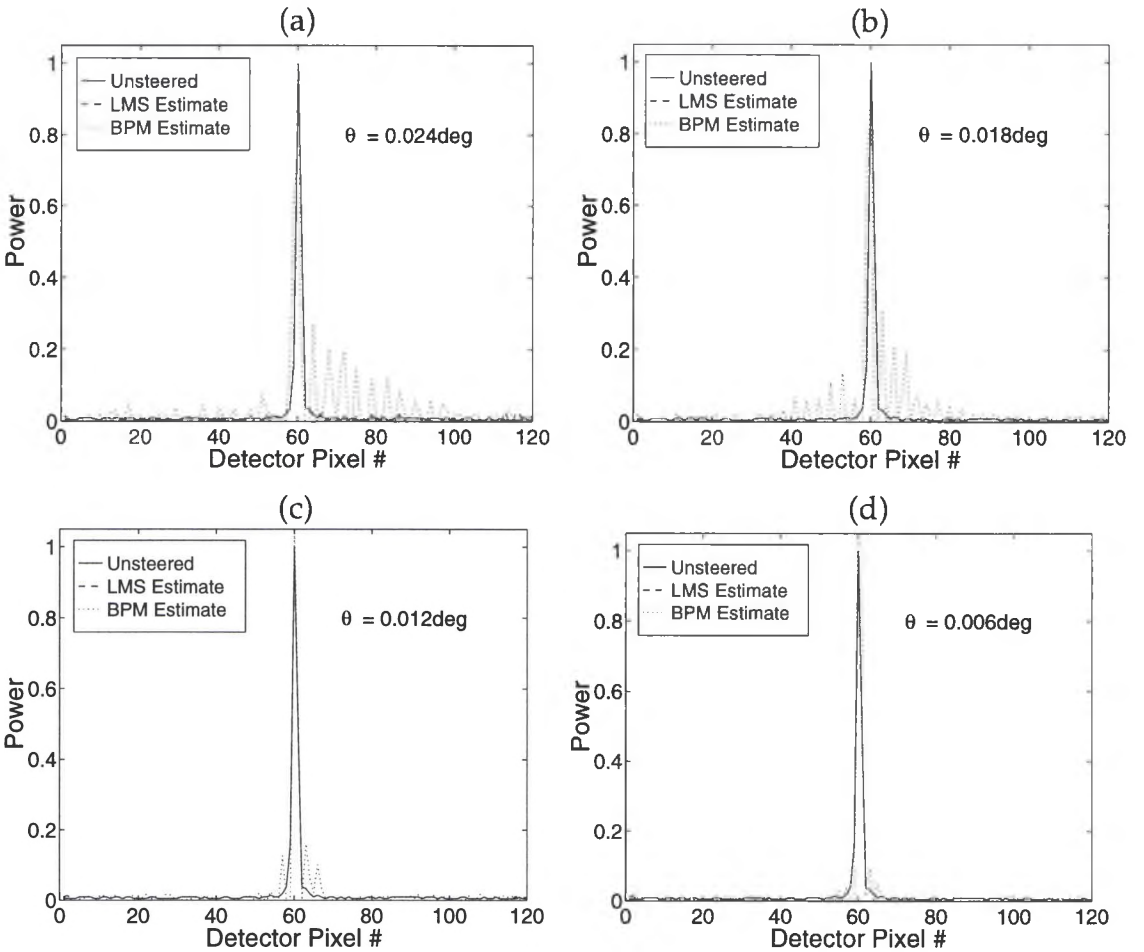

Figure 5.5) *Broad-band restorations of a steered 1-D single slit. Results are shown for both the experimental LMS filter and the BPM-derived LMS filter on a bandwidth of 400-700 nm, steered to four different steer angles. Restorations are shown for steer angles of (a) 0.024°, (b) 0.018°, (c) 0.012°, (d) 0.006°. Measurements of MSE are given in Table 5.2.*

Table 5.2) *Filter restoration (Improvement) measurements for the broad-band single slit image restorations shown in Figure 5.5. The* Improvement Ratio *is a ratio of the baseline mean square error (MSE) to the MSE of the filter estimate. A value greater than one indicates improvement.*

		Improvement Ratio	
$\Delta\lambda$ (nm)	θ_{steer} (°)	LMS Filter	BPM Filter
400-700	0.024	157.7	0.9
400-700	0.018	1251.0	0.6
400-700	0.012	1380.0	4.2
400-700	0.006	1291.0	0.9

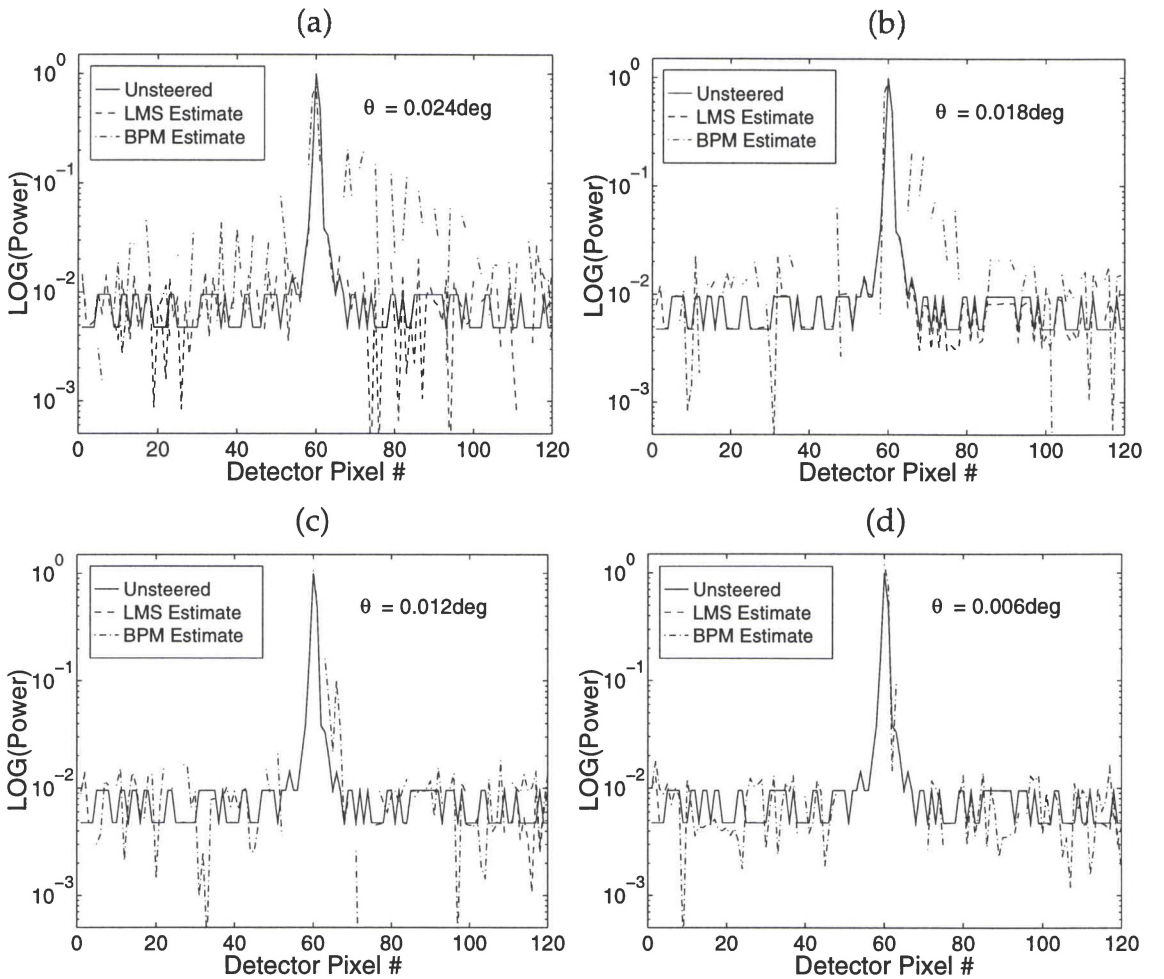

Figure 5.6) *Broad-band restorations of a steered 1-D single slit. Results are plotted using a logarithmic scale to show greater detail in the lower magnitudes. Results are shown for both the experimental LMS filter and the BPM-derived LMS filter on a bandwidth of 400-700 nm, steered to four different steer angles. Restorations are shown for steer angles of (a) 0.024°, (b) 0.018°, (c) 0.012°, and (d) 0.006°.*

variations such as noise and detector nonlinearities. The "BPM Estimate" is a result of the *BPM*-derived *LMS* coefficients derived from broad-band steered and unsteered data created by the *BPM* model. Measurements of the filter restoration results are presented in Tables 5.1 and 5.2 for both variable bandwidth and steer angle, respectively. These tables make use of the *Improvement Ratio* defined in Chapter 4. By examining the improvement ratios in

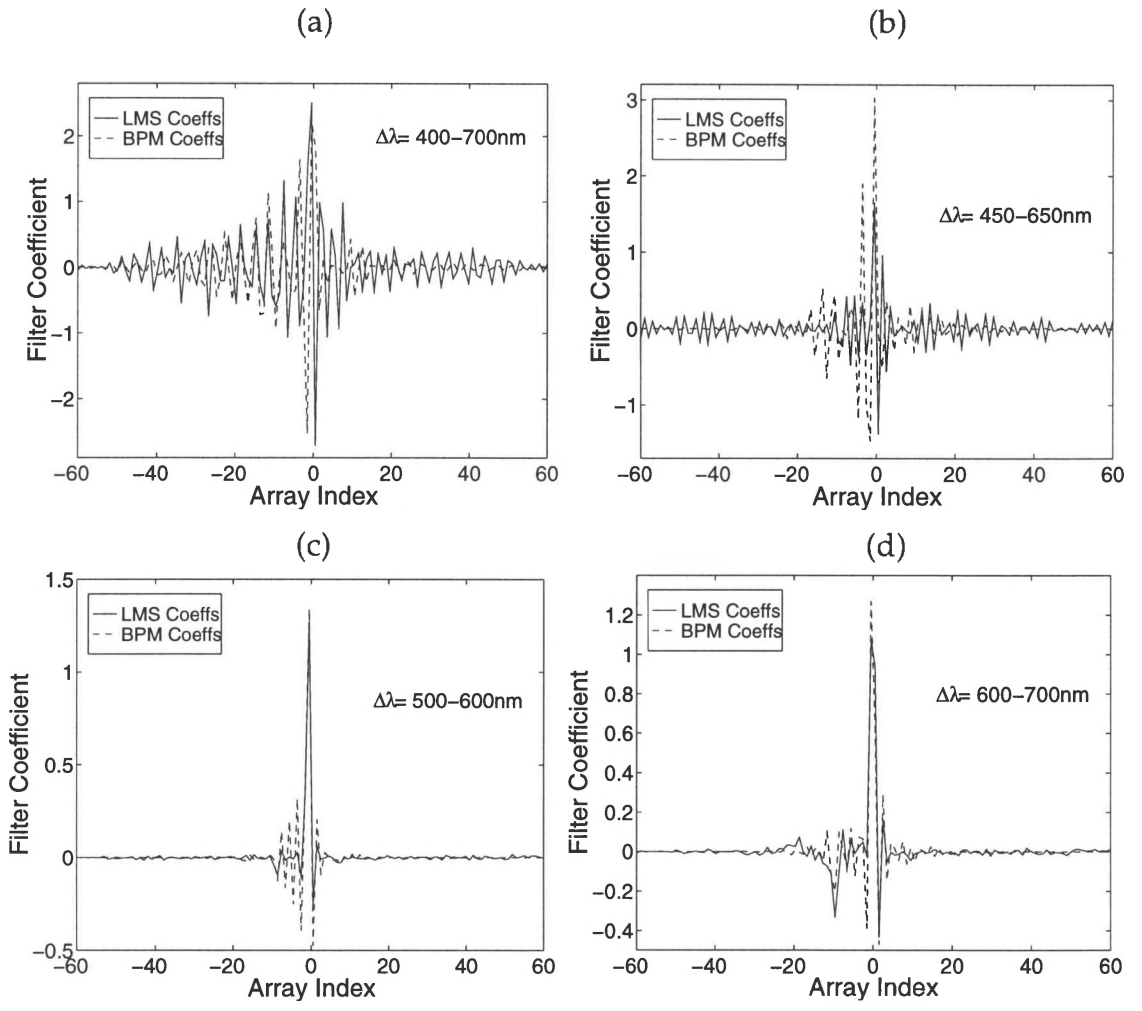

Figure 5.7) *Each plot shows the optimized LMS filter coefficients and theoretical (BPM) filter coefficients for one of four bandwidths: (a) 400-700 nm, (b) 450-650 nm, (c) 500-600 nm, (d) 600-700 nm. The LMS coefficients are derived from the experimental data. The BPM-derived filter coefficients are derived from BPM model data also using the LMS. The filter coefficients are computed for data originally steered to 0.024°.*

Table 5.1, it is observed that the filter estimates, both experimental and *BPM*-derived, obtain greater improvement on the steered images with smaller bandwidths. This is due to the less severe degradations present in the smaller bandwidth images. There is also less image degradation as the steer angle is decreased. The images will typically show less of a smearing effect as the steer

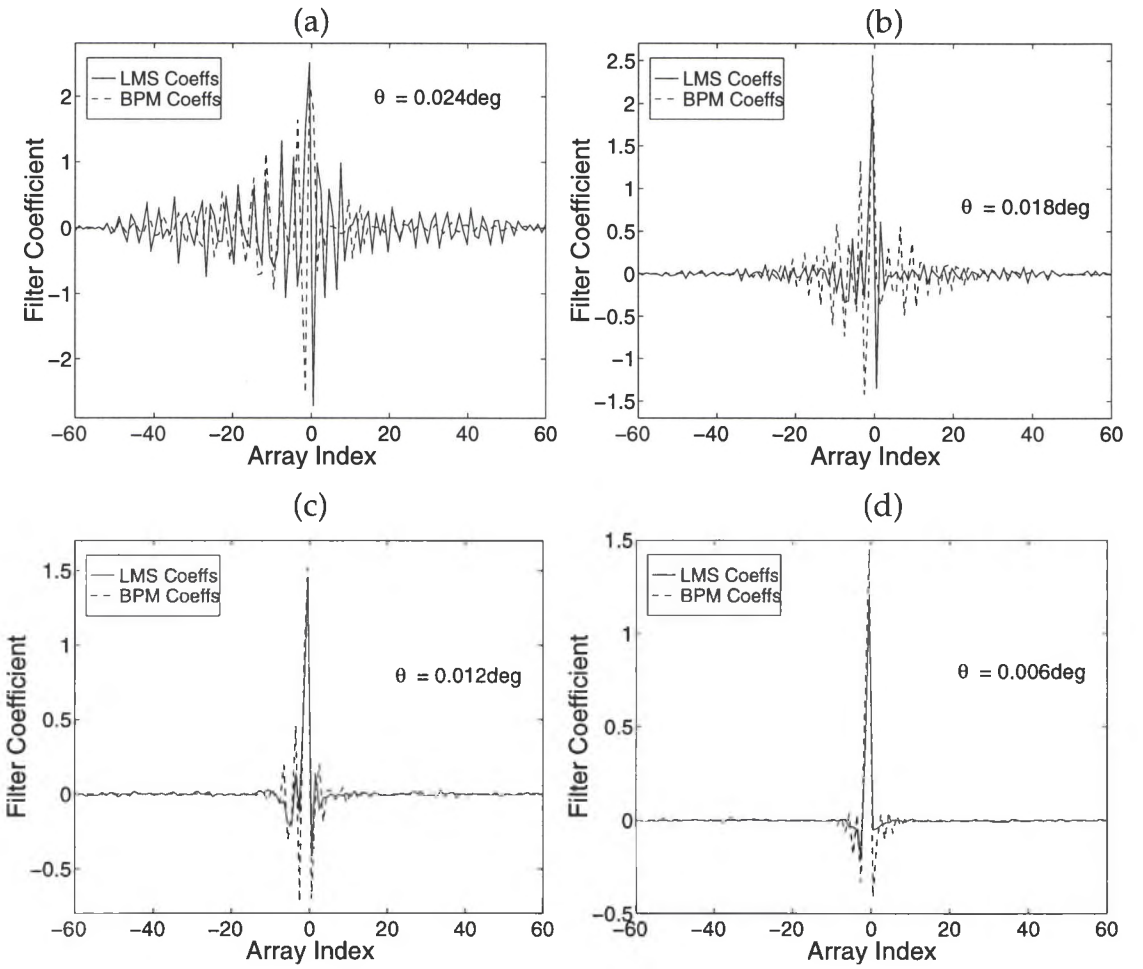

Figure 5.8) *Each plot shows the optimized LMS filter coefficients and theoretical (BPM) filter coefficients for a bandwidth of 400-700 nm steered to four different angles: (a) 0.024°, (b) 0.018°, (c) 0.012°, (d) 0.006°. The LMS coefficients are derived from the experimental data. The BPM-derived filter coefficients are derived from BPM model data also using the LMS.*

angle is decreased making it easier for the filter coefficients to perform accurate image restoration. The inferior performance of the *BPM*-derived *LMS* filter coefficients (trained on *BPM* predicted data) is again a result of the inaccuracies in the phase profile and the noise statistics which are not present in the *BPM* data. As a result these coefficients do not take into account any noise in the images. If the experimental and theoretical filter coefficients are compared it can

be seen that there are drastic differences between them, especially at the larger bandwidths where the degradations are more severe. On average, however, the filters derived from the *BPM* data will provide an improved starting point for the experimental *LMS* algorithm.

Due to the lack of experimental data, the remainder of the broad-band filter characterizations will be performed using filters derived from the *BPM* model. The steered and unsteered data used by the *LMS* algorithm will not contain any of the statistical noise commonly found in experimental images. However, this data will offer a substantial amount of insight into broad-band filter robustness testing.

5.2 Broad-band Filter Robustness: Bandwidth Dependence

In the next two sections, one of the most important broad-band filter characteristics is measured: robustness. These tests, which examine filter performance against a variable bandwidth or emission spectrum (Section 5.3), are analogous to the robustness measurements in Chapter 4 performed against a variable wavelength. The importance of this measurement is realized when attempting to restore a steered broad-band image without specific training data. If a theoretically derived filter is to be successfully used in restoration, it must contain information about the original object, including bandwidth and spectral emission. Measuring broad-band filter robustness will indicate how well this information must be known for successful restoration. Bandwidth robustness is

tested by creating steered and unsteered data of varying bandwidths and computing the corresponding *LMS* filter coefficients for each bandwidth. The filter coefficients derived for a given bandwidth are then used to compute restored estimates of itself and the other bandwidths. Spectral emission robustness is tested by creating steered and unsteered data in a given bandwidth and then weighting each of the wavelengths using a blackbody emission curve. By changing the temperature of the blackbody curve the spectral emission characteristics are changed thus affecting the weights within the bandwidth.

To begin the characterization of bandwidth robustness, the *BPM* model was used to generate data of varying bandwidths within the range of 500-900 nm. Each of the bandwidths is steered using a device with the 2π phase resets designed for λ = 700 nm. The first analysis involves measuring filter robustness as the bandwidth is altered but reamins centered about the design wavelength. Starting with a minimum bandwidth of 680-720 nm (± 2.9% of 700 nm), the bandwidth is increased in ±20 nm increments to the maximum bandwidth of 500-900 nm (± 28.5% of 700 nm). A flat spectral emission curve was used to weight the steered and unsteered model predictions so that each wavelength sample contained an equal amount of energy. The steered and unsteered model predictions for six of the bandwidths is presented in Figure 5.9 to show the behavior of the steered results as the bandwidth changes. Note the increase in the amount of diffraction energy (smearing and sidelobes) as the bandwidth is

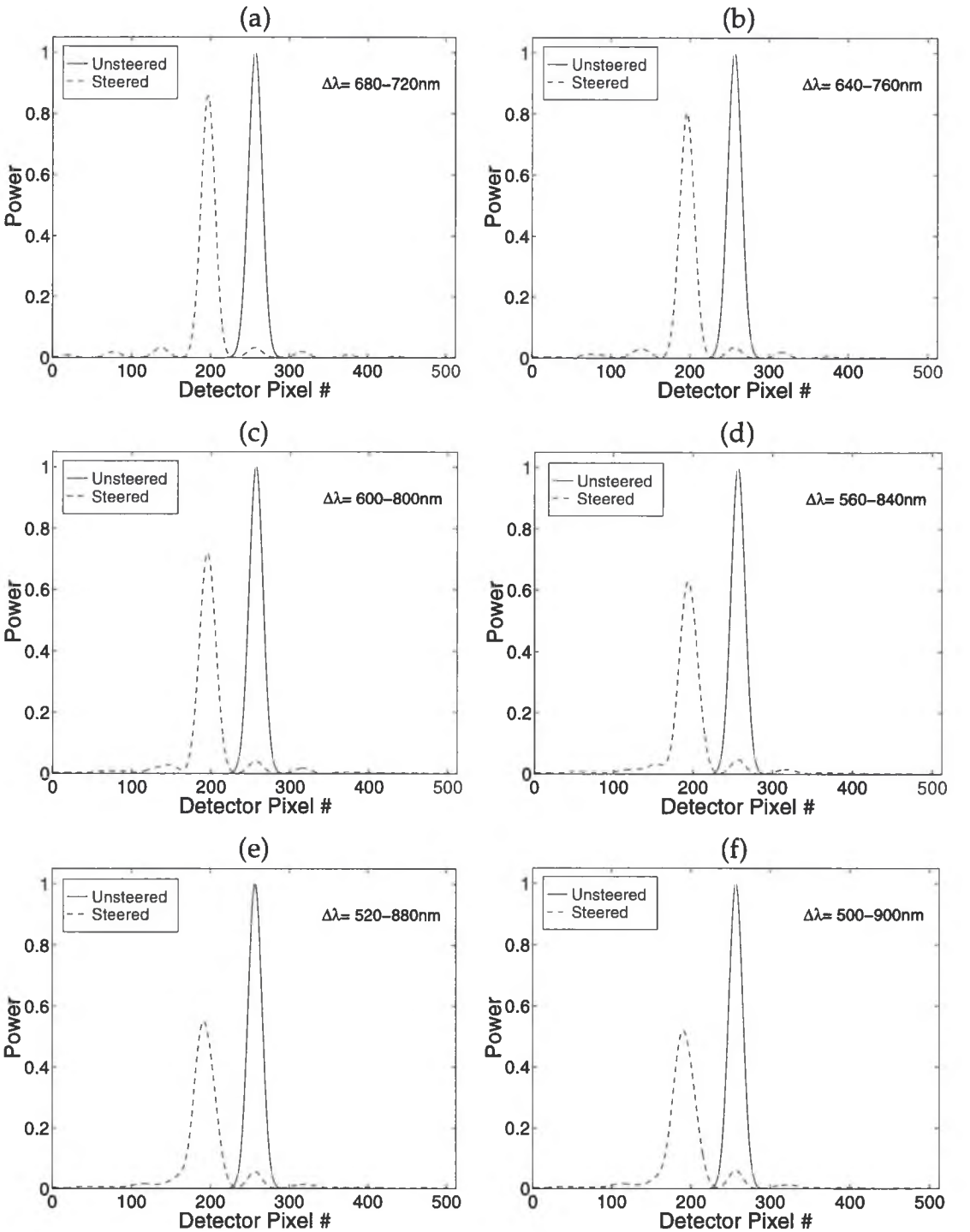

Figure 5.9) *Comparison of broad-band steered and unsteered 1-D single slits predicted by the BPM model with an angular FWHM of 0.05°. Results are shown for six different bandwidths steered to 0.024°. Bandwidths of (a) 680-720 nm, (b) 640-760 nm, (c) 600-800 nm, (d) 560-840 nm, (e) 520-880 nm, (f) 500-900 nm, are steered with a device design wavelength of 700 nm.*

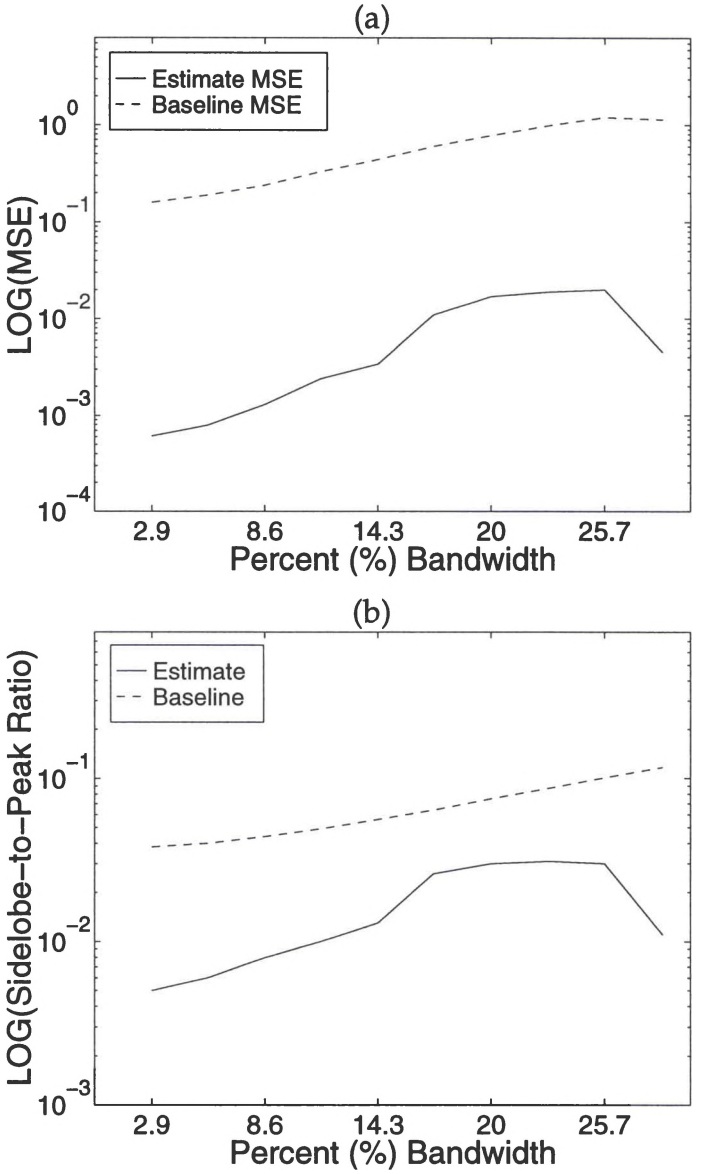

Figure 5.10) *(a) Comparison of the MSE of the filter estimate to the baseline MSE between the steered and unsteered at the ten possible bandwidths. (b) Comparison of the sidelobe to peak ratio of the filter estimate to that of the original steered peak at the ten possible bandwidths. Each filter was used to restore its own data.*

increased. *LMS* filter coefficients are then calculated for the steered images at each of these bandwidths and used to restore the images at the other bandwidths. It is here that the ratio of the largest sidelobe to the peak in the filter estimate becomes an important characteristic measurement.

By examining the *MSE* between the unsteered (desired) and the filter estimate, it is observed that each filter has excellent restoration ability when restoring its original bandwidth. The *MSE* for each bandwidth, compared to the baseline *MSE* between the steered and unsteered, is presented in Figure 5.10(a). The ability of the filter coefficients to place the diffraction order energy back to the main peak position is presented in Figure 5.10(b). The data labeled "Estimate" represents the sidelobe to peak ratio of the filter estimate and the data labeled "Baseline" represents the sidelobe to peak ratio in the original steered image. The "Estimate" curves in Fig. 5.10 do not appear parallel with the "Baseline" curves because of the different window sizes and number of interations used to compute each set of filter coefficients. Each filter was derived using a given number of iterations until the restoration it produced was visibly excellent. This figure shows the sidelobe to peak ratio in the estimate is always less than that of the original steered image which indicates there is less energy in the sidelobes of the restored image. The question remains, however, about the possibility of using a filter derived on one bandwidth to restore the steered image of a different bandwidth.

To answer this question, each filter was used to restore each of the other nine bandwidths. It was discovered that the middle bandwidth (8% - 17%) filters performed the best over the range of bandwidths (2.9% - 28.5%). The larger bandwidth filters attempt to shift *more* diffraction order energy in the smaller

(a)

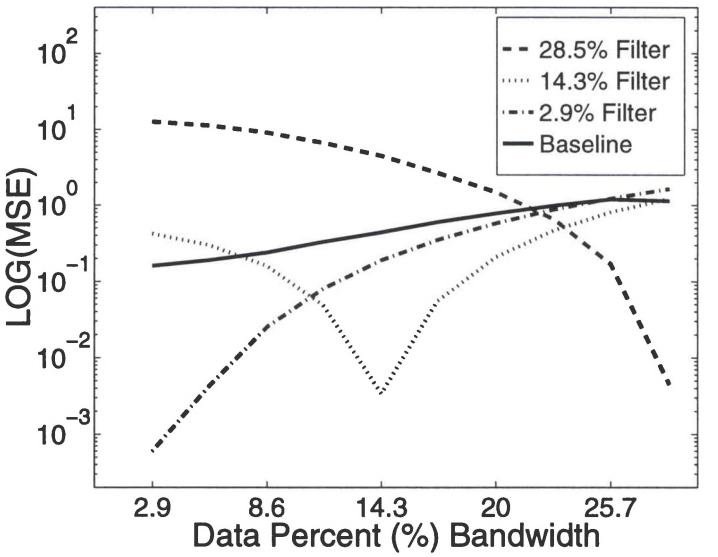

(b)

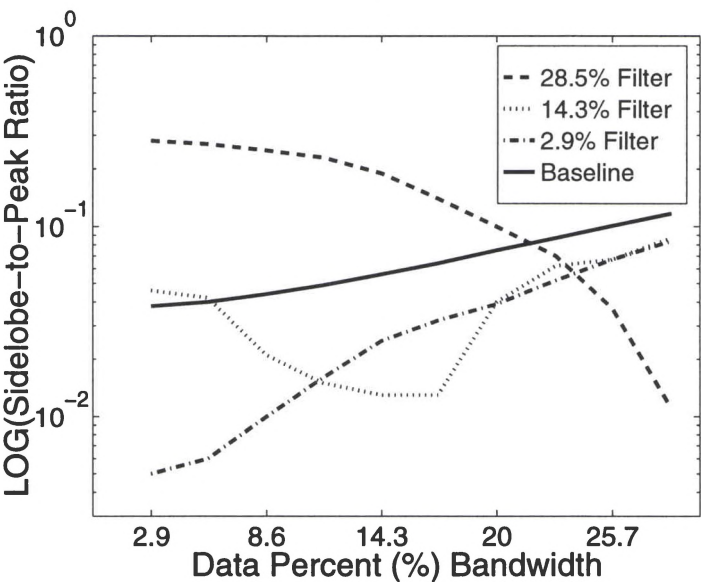

Figure 5.11) *Examples of filter performance as each of the indicated filters is used to restore the steered results at each of the ten bandwidths used in the BPM model. (a) Comparison of the MSE of the filter estimates to the baseline MSE between the steered and unsteered at the ten possible bandwidths. (b) Comparison of the sidelobe to peak ratio of the filter estimates to that of the original steered peak at the ten possible bandwidths.*

bandwidth data than exists, resulting in a large *MSE*. These filters will tend to insert more diffraction order echoes than originally existed, allowing

improvement on steered data only starting above 75% of the original bandwidth. The smaller bandwidth filters attempt to shift *less* diffraction order energy in the larger bandwidth data than what exists, resulting in a *MSE* comparable to the baseline *MSE*. This makes the smaller bandwidth filters ineffective by the time the bandwidth of the steered test data is doubled. The filter estimate *MSE* for three different bandwidth filters is shown in Figure 5.11(a) as a function of the different bandwidth data. The baseline *MSE* is also given as a reference to show whether or not the filter estimate at each bandwidth is an improvement compared to the steered original. Sidelobe to peak measurements for the same filters and bandwidths are presented in Figure 5.11(b). These results indicate that the filter coefficients derived on broad-band data have a greater degree of robustness versus a varying bandwidth than the narrow-band filters versus a varying wavelength. It was also shown that filters can perform at least a small amount of improvement on data with a bandwidth up to two-times, or starting above three-quarters, the size of the original data. The results indicate that, on average, the filter derived from the 14.3% bandwidth data performed the best restorations on the various bandwidths.

Next we would like to make the same meaurements with steered (degraded) and unsteered (desired) with a smaller spot size. This is done by reducing the angular FWHM of each superimposed narrow-band wavelength to 0.001°, which is a reduction in angular FWHM by a factor of 50 from the data

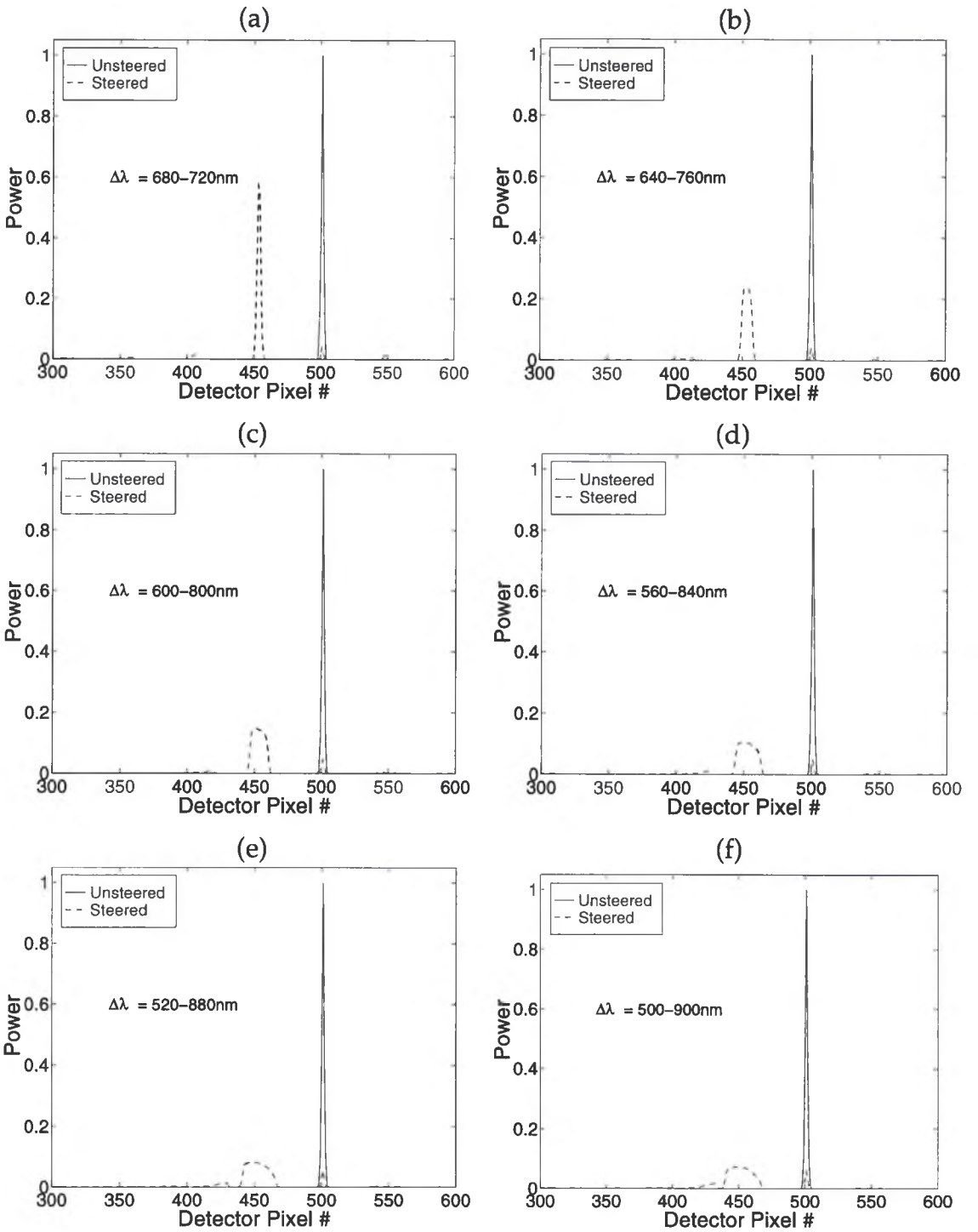

Figure 5.12) *Comparison of broad-band steered and unsteered 1-D single slits predicted by the BPM model with a NARROW FWHM of 0.001°. Results are shown for six different bandwidths steered to 0.024°. Bandwidths of (a) 680-720 nm, (b) 640-760 nm, (c) 600-800 nm, (d) 560-840 nm, (e) 520-880 nm, (f) 500-900 nm, are steered with a device design wavelength of 700 nm.*

examined in Figs. 5.9 - 5.11. The reduction in angular FWHM results in intensity patterns that are approximately impulses. Several steered and unsteered *BPM* calculated bandwidths are shown in Figure 5.12. The smearing effects, which

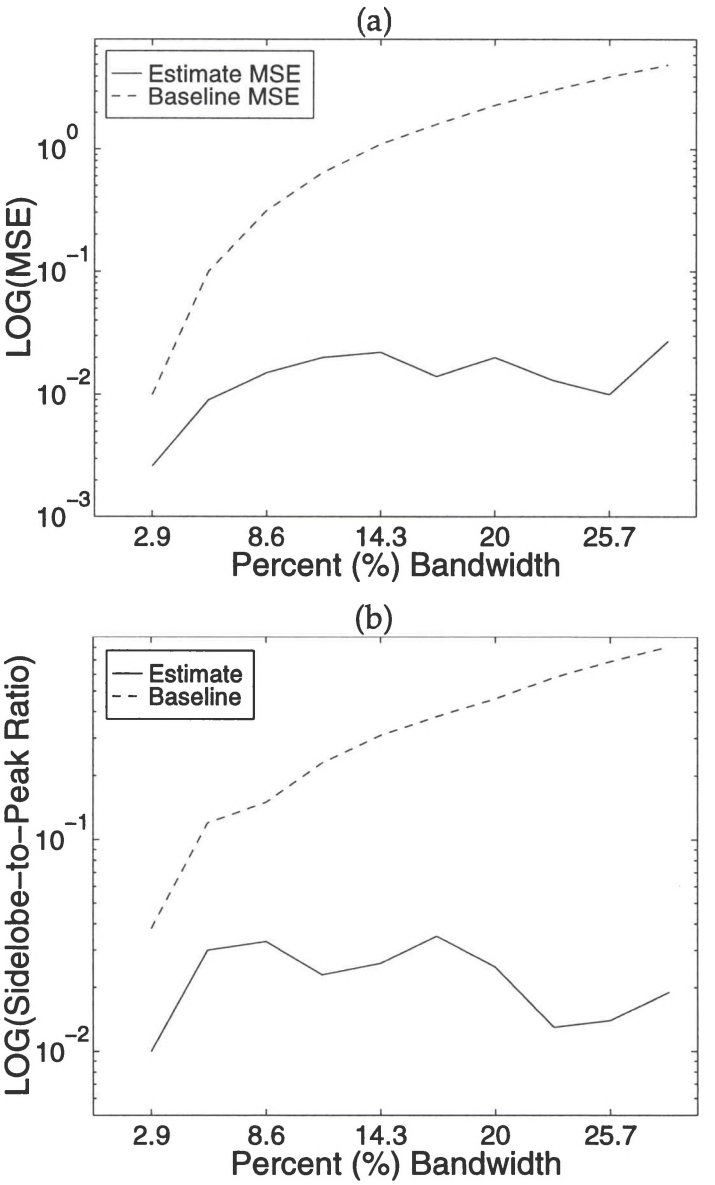

Figure 5.13) *(a) Comparison of the MSE of the filter estimate to the baseline MSE between the steered and unsteered at the ten possible bandwidths for the NARROW FWHM data (angular FWHM = 0.001°. (b) Comparison of the sidelobe to peak ratio of the filter estimate to that of the original steered peak at the ten possible bandwidths. Each filter was used to restore its own data.*

appear less severe in the previous data (Fig. 5.9), can immediately be seen as the bandwidth is widened. After *LMS* filter coefficients are derived for the degraded and desired images, the restoration ability of each set of filter coefficients is again

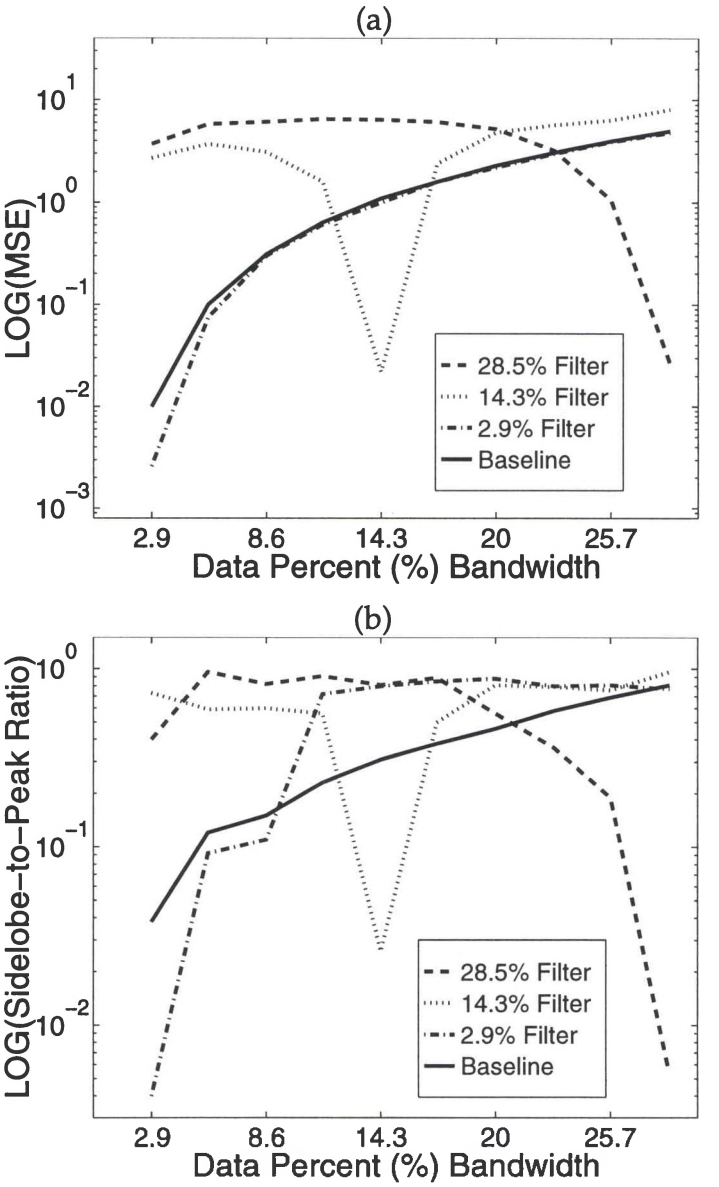

Figure 5.14) *Examples of filter performance as each of the indicated filters is used to restore the steered results at each of the ten bandwidths predicted by the BPM model for the NARROW FWHM (angular FWHM = 0.001°). (a) Comparison of the MSE of the filter estimates to the baseline MSE between the steered and unsteered at the ten possible bandwidths. (b) Comparison of the sidelobe to peak ratio of the filter estimates to that of the original steered peak at the ten possible bandwidths.*

tested over the range of data bandwidths. The performance of each set of filter coefficients on it's training data is first compared to the baseline error between the degraded and desired images. The results shown in Figure 5.13 indicate that each set of filter coefficients does perform an excellent job of restoring the original training data. However, if the restoration ability of a given filter tested versus the other bandwidth data, it can be seen (Figure 5.14) that the different sets of bandwidth filter coefficients do not perform as well as those derived from the wider angular FWHM data (Fig. 5.11). These results indicate that broad-band filters are not as robust versus a changing bandwidth when the steered and unsteered images predicted by the *BPM* are approximately impulse responses.

Broad-band steered data was also created for non-centered bandwidths with a wider angular FWHM (0.05°). The device design wavelength remains at 700 nm while the bandwidth size and position is varied within the 500-900 nm range. The data is then weighted using a blackbody curve for the white light source temperature of 2880 K. For example, data is derived by the *BPM* for bandwidths of 500-600 nm, 500-650 nm, 500-700 nm, 500-750 nm, 500-800 nm, and 500-900 nm which are referred to as the "500-end" bandwidths. Data is also derived by the BPM for bandwidths of 800-900 nm, 750-900 nm, 700-900 nm, 650-900 nm, and 600-900 nm which are referred to as the "900-end" bandwidths. This data is used to measure bandwidth robustness as a function of non-centered bandwidths.

Bandwidth measurements begin by examining the behavior of the filter coefficients derived from the "500-end" bandwidths. Each filter is tested, like those derived on the centered bandwidths, to see how well it can restore a bandwidth which is either smaller or larger than the original bandwidth. It is in these measurements that the shifted, mean square error (*SMSE*) and the pixel shift between the peaks of the filter estimate and the unsteered image become very important. Recall that the *SMSE* is the mean square measured between the filter estimate, after it is shifted to the position of the unsteered peak, and the unsteered peak. As the bandwidth is enlarged, each additional wavelength will be steered to a slightly different angle and thus contribute to the smearing or spreading effect at the detector plane. The wavelength with the strongest intensity establishes the approximate position of the steered peak. As the "500-end" bandwidths are increased, the position of the main steered peak will shift according to the position of the longest wavelength in the bandwidth due to the increasing energy in the longer wavelengths. Resulting filter coefficients must adapt to different amounts of steering (far field pixel shift) as the bandwidth changes. For this reason, the peak of a given filter estimate may be shifted away from the position of the unsteered peak giving large values of *MSE* for visually good estimates. The effect is not as severe upon examining the "900-end" bandwidths due to the maximum energy wavelengths already being contained in the smallest bandwidth (800-900 nm). Robustness tests for both sets of bandwidth data will include visual comparisons and numerical measurements of

MSE, *SMSE*, pixel shift, and largest sidelobe to peak ratio. Baseline measurements between the original steered and unsteered data will also be presented as a reference for improvement. Note that for the baseline measurements *MSE* = *SMSE* and the pixel shift is zero.

Figures 5.15 and 5.16 show each filter restoration result for the "500-end" filters 500-600 nm and 500-900 nm, respectively, as a function of bandwidth. Notice how the peak of the filter estimate is shifted with respect to the unsteered peak as the bandwidth changes. Since each set of filter coefficients is derived on data steered (shifted) to slightly different positions, the coefficients will often place the restored image of a different bandwidth in the wrong position. Tables 5.3, 5.4, and 5.5 show the numerical performance measurements of each filter on each bandwidth. It can be seen in Table 5.3 that the filters do not appear robust as the improvement ratios indicate poor restoration with little change in bandwidth. These results show that filter improvement is strictly limited to the

Table 5.3) *Improvement ratio measurements from the MSE for the broad-band single slit image restorations of non-centered "500-end" bandwidth data. Examples of restoration results are found in Figures 5.15 and 5.16. The* Improvement Ratio *is a ratio of the baseline MSE to the MSE of the filter estimate. A value greater than one indicates improvement.*

	Filter Bandwidth (nm)					
Data Bandwidth (nm)	500-600	500-650	500-700	500-750	500-800	500-900
500-600	1540.0	2.2	0.7	0.4	0.3	0.3
500-650	2.8	1143.0	2.5	0.7	0.4	0.2
500-700	0.5	2.5	530	2.5	0.7	0.2
500-750	0.2	0.6	2.3	358.0	2.3	0.3
500-800	0.1	0.3	0.6	2.1	288.0	0.5
500-900	0.08	0.1	0.2	0.2	0.5	2522.0

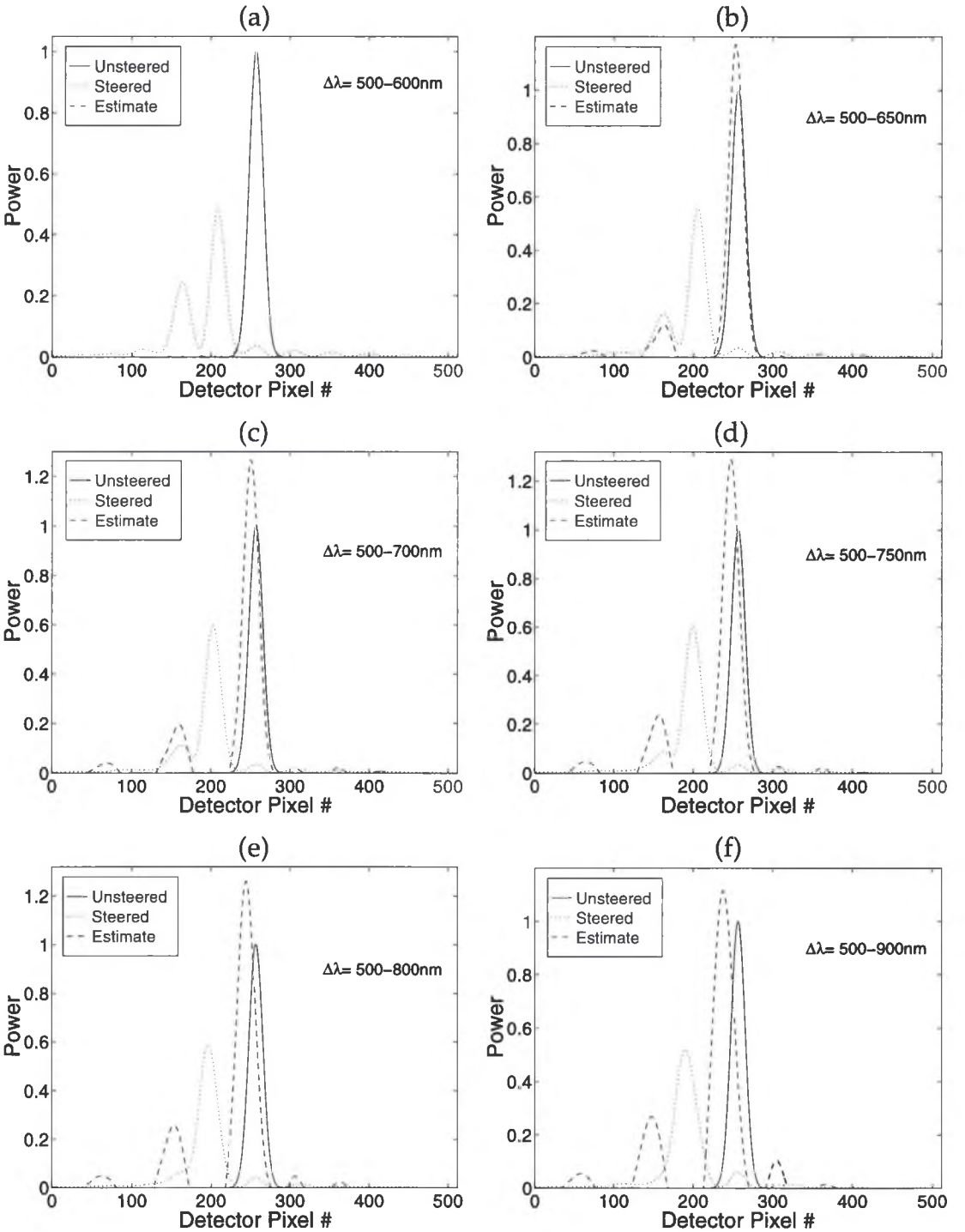

Figure 5.15) *Filter restorations using filter coefficients derived on data of bandwidth* ***500-600 nm*** *with an angular FWHM of 0.05°. The same filter coefficients are then used to restore data of six different bandwidths: (a) 500-600 nm, (b) 500-650 nm, (c) 500-700 nm, (d) 500-750 nm, (e) 500-800 nm, and (f) 500-900 nm. The data examined was originally steered to an angle of 0.024° using a device design wavelength of 700 nm.*

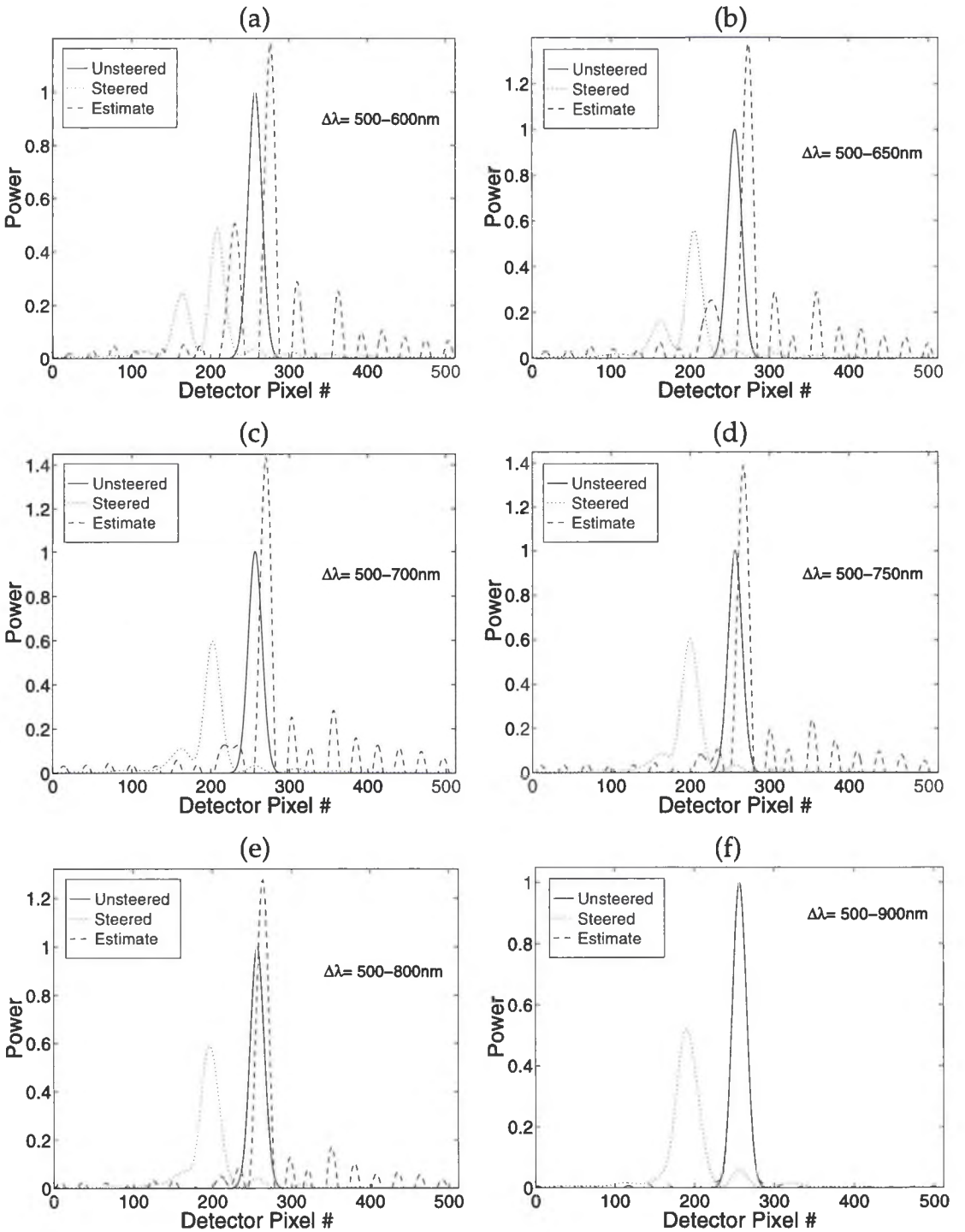

Figure 5.16) *Filter restorations using filter coefficients derived on data of bandwidth* ***500-900 nm*** *with an angular FWHM of 0.05°. The same filter coefficients are then used to restore data of six different bandwidths: (a) 500-600 nm, (b) 500-650 nm, (c) 500-700 nm, (d) 500-750 nm, (e) 500-800 nm, and (f) 500-900 nm. The data examined was originally steered to an angle of 0.024° using a device design wavelength of 700 nm.*

Table 5.4) *Improvement ratio measurements from the shifted, mean square error SMSE and the corresponding pixel shift for the broad-band single slit image restorations of non-centered "500-end" bandwidth data. Examples of restoration results are found in Figures 5.15 and 5.16. The* Improvement Ratio *is a ratio of the baseline MSE to the SMSE of the filter estimate. A value greater than one indicates improvement.*

	Filter Bandwidth (nm)											
Data Bandwidth (nm)	500-600		500-650		500-700		500-750		500-800		500-900	
500-600	1540.0	(0)	3.8	(2)	1.5	(5)	0.8	(9)	0.5	(12)	0.3	(19)
500-650	4.7	(4)	1143.0	(0)	8.4	(2)	2.6	(6)	0.9	(9)	0.3	(16)
500-700	1.2	(6)	13.1	(3)	530.0	(0)	17.4	(4)	3.2	(7)	0.4	(14)
500-750	0.5	(9)	2.52	(6)	2.5	(3)	358.0	(0)	19.0	(4)	0.5	(11)
500-800	0.2	(13)	0.7	(10)	3.0	(7)	20.8	(4)	288.0	(0)	1.4	(7)
500-900	0.1	(19)	0.2	(16)	0.3	(14)	0.6	(11)	1.7	(8)	2522.0	(0)

data from which it was derived. However, if the improvement ratio is measured as a result of the shifted, mean square error (*SMSE*), the filter coefficients show greater ability to restore the other bandwidths. Table 5.4 gives the improvement ratio calculated with *SMSE* and the detector pixel shift between the estimate and the unsteered. The results show that the filter coefficients can give a significant amount of improvement on image bandwidths out to approximately two-times, or down to three-quarters, of the original bandwidth. The same phenomena can be seen in the *centered*-bandwidth analysis. The results in Table 5.4 also show that the improvement ratio can be increased by as much as a factor of ten by measuring the *SMSE* of the filter estimate. If the improvement ratio is measured using the normalized, shifted, mean square error (*NSMSE*) of the filter estimate,the wider bandwidth filters are found to give improvement down to about one-half of the original bandwidth. This is due to the larger peaks,

compared to the unsteered image, found in some the estimates filtered with different bandwidth filters (see Fig. 5.16). Normalization has the effect of decreasing the effective magnitude of the estimate peak *and* the magnitudes of the diffraction echoes with respect to the unsteered image, thus providing an increased improvement measurement. Normalization has the opposite effect on estimates which have smaller peaks compared to the unsteered image. The peak of the estimate is increased to that of the unsteered image, however, the diffraction echoes are also increased resulting in little overall change in the improvement ratio compared to *SMSE*. Notice that the middle size bandwidth filters appear to perform the best over the range of test bandwidths. The largest sidelobe to peak ratios are given in Table 5.5. Notice that the middle bandwidth filters give improvement and sidelobe-to-peak ratio results which are consistently better than the steered data.

Next, the "900-end" filter performance is measured using the same analysis used for the "500-end" filters. Figures 5.17 and 5.18 show each filter restoration

Table 5.5) *Ratio of the largest sidelobe magnitude to that of the steered peak. The baseline ratio is a measure of the peak of the largest diffraction order to the steered peak. Ratios are measured from the "500-end" data.*

	Filter Bandwidth (nm)						
Data Bandwidth (nm)	500-600	500-650	500-700	500-750	500-800	500-900	Baseline
500-600	0.09	0.24	0.36	0.42	0.45	0.43	0.5
500-650	0.10	0.006	0.13	0.19	0.22	0.21	0.3
500-700	0.15	0.02	0.008	0.07	0.11	0.20	0.19
500-750	0.18	0.04	0.02	0.009	0.04	0.17	0.14
500-800	0.20	0.05	0.04	0.03	0.01	0.14	0.07
500-900	0.24	0.10	0.10	0.10	0.1	0.01	0.12

result for the "900-end" filters 800-900 nm and 500-900 nm, respectively, as a function of bandwidth. Each of these filters is tested in the same way as the "500-end" filter previously tested. The results will be similar to those found in the previous analysis with the exception that there will be less detector pixel shift between the filter estimate and the unsteered image versus bandwidth. Initial improvement ratio measurements are given in Table 5.6. The results in this table show that the filters offer image improvement out to approximately two-times, or down to three-quarters, of the original bandwidth. It appears that these filters are more robust when compared to the performance of the "500-end" filters.

Table 5.6) *Improvement ratio measurements from the mean square error (MSE) for the broad-band single slit image restorations of non-centered "900-end" bandwidth data. Examples of restoration results are found in Figures 5.17 and 5.18. The* Improvement Ratio *is a ratio of the baseline MSE to the MSE of the filter estimate. A value greater than one indicates improvement.*

	Filter Bandwidth: MSE (nm)					
Data Bandwidth (nm)	800-900	750-900	700-900	650-900	600-900	500-900
800-900	1513.0	1.9	0.5	0.2	0.1	0.1
750-900	2.8	1685.0	2.1	0.6	0.2	0.2
700-900	0.9	3.2	1098.0	2.7	0.6	0.3
650-900	0.6	1.1	4.1	990.0	3.1	0.9
600-900	0.5	0.7	1.6	6.1	945.0	3.0
500-900	0.5	0.7	1.0	2.0	4.4	2522.0

This is due in part to the smaller pixel shifts experienced by the filter estimates and the fact that the longer wavelengths, which carry more of the blackbody spectral power, are contained in all of the variable test bandwidths. Table 5.7 shows the result of measuring the filter *SMSE* and the corresponding detector pixel shift for each filter estimate. Notice the smaller amount of pixel shift

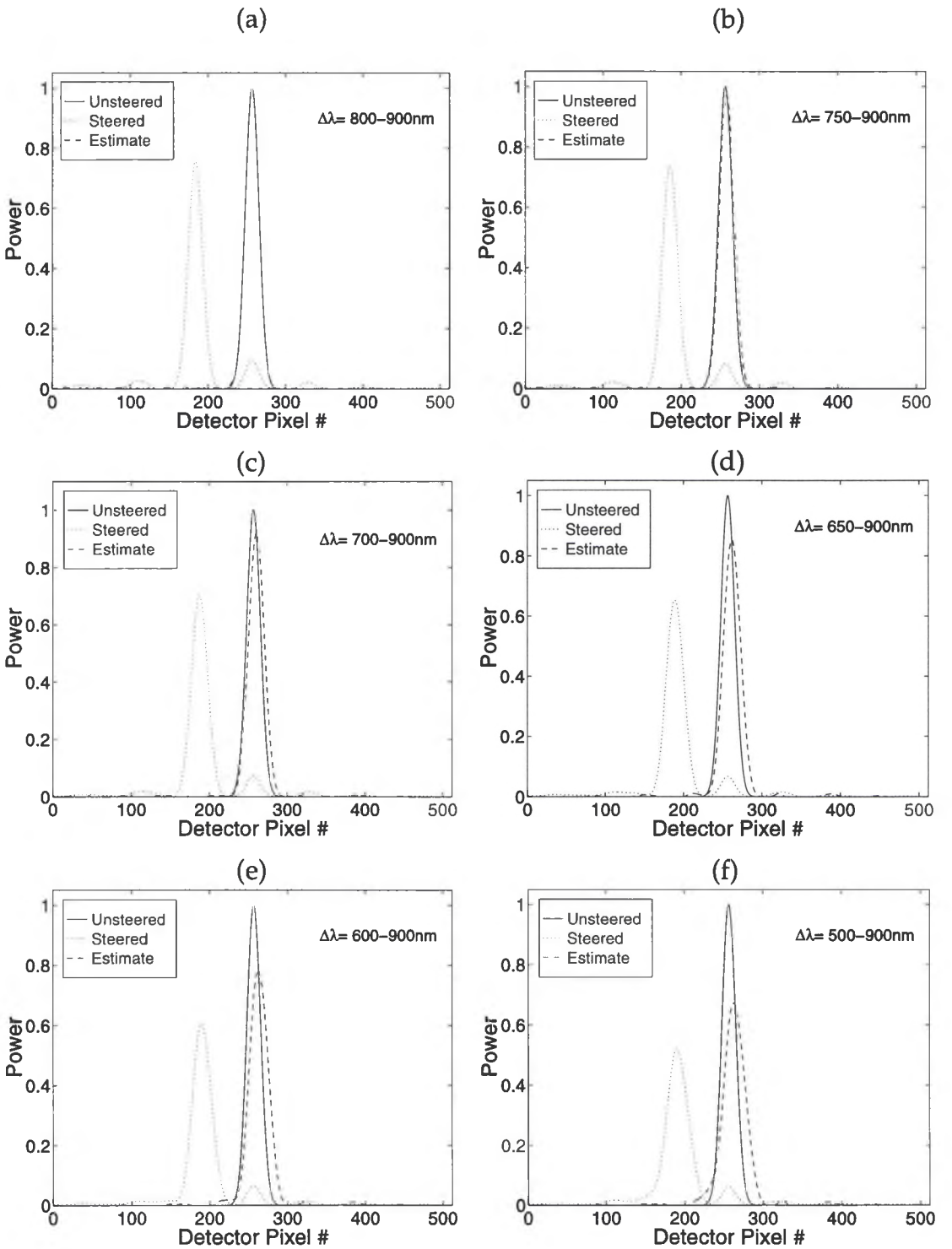

Figure 5.17) *Filter restorations using filter coefficients derived on data of bandwidth* ***800-900 nm*** *with an angular FWHM of 0.05°. The same filter coefficients are then used to restore data of six different bandwidths: (a) 800-900 nm, (b) 750-900 nm, (c) 700-900 nm, (d) 650-900 nm, (e) 600-900 nm, and (f) 500-900 nm. The data examined was originally steered to an angle of 0.024° using a device design wavelength of 700 nm.*

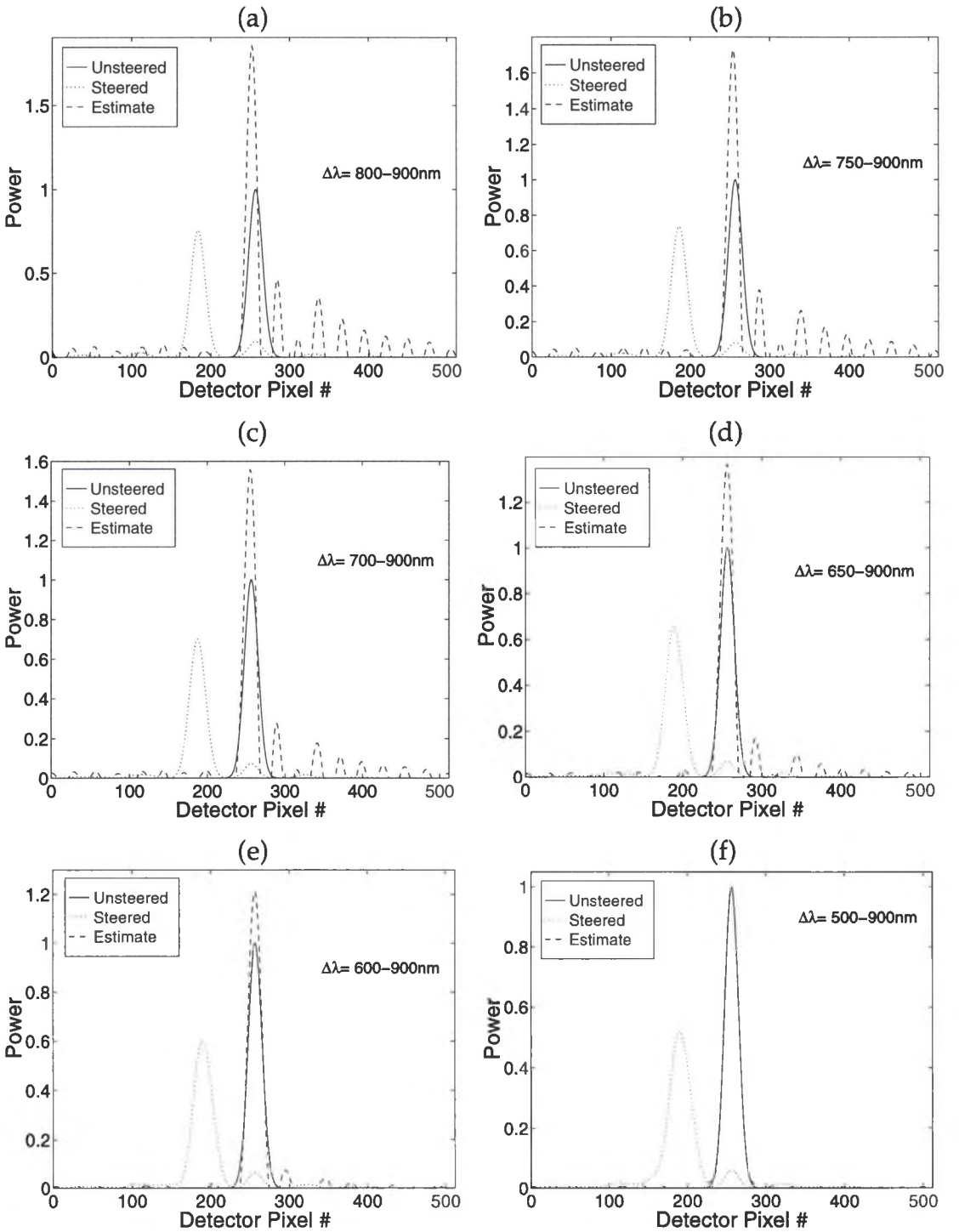

Figure 5.18) *Filter restorations using filter coefficients derived on data of bandwidth* ***500-900 nm*** *with an angular FWHM of 0.05°. The same filter coefficients are then used to restore data of six different bandwidths: (a) 800-900 nm, (b) 750-900 nm, (c) 700-900 nm, (d) 650-900 nm, (e) 600-900 nm, and (f) 500-900 nm. The data examined was originally steered to an angle of 0.024° using a device design wavelength of 700 nm.*

Table 5.7) *Improvement ratio measurements from the shifted, mean square error SMSE and the corresponding pixel shift for the broad-band single slit image restorations of non-centered "900-end" bandwidth data. Examples of restoration results are found in Figures 5.17 and 5.18. The* Improvement Ratio *is a ratio of the baseline MSE to the SMSE of the filter estimate. A value greater than one indicates improvement.*

	Filter Bandwidth: SMSE (nm)											
Data Bandwidth (nm)	800-900		750-900		700-900		650-900		600-900		500-900	
800-900	1513.0	(0)	18.0	(3)	2.6	(4)	0.6	(5)	0.2	(5)	0.1	(5)
750-900	41.0	(1)	1685.0	(0)	8.3	(2)	1.3	(3)	0.3	(3)	0.2	(3)
700-900	9.6	(3)	18.4	(1)	1098.0	(0)	4.7	(2)	0.7	(2)	0.4	(2)
650-900	2.9	(5)	4.8	(3)	96.5	(1)	990.0	(0)	3.6	(1)	1.0	(1)
600-900	1.4	(6)	2.3	(4)	3.3	(2)	89.5	(1)	945.0	(0)	3.0	(1)
500-900	1.0	(6)	1.2	(4)	1.5	(1)	2.2	(1)	4.4	(0)	2522.0	(0)

between the restored and desired in these images and the increased amount of improvement performed as the bandwidth becomes smaller. Smaller bandwidth filters have a tendency to 'not filter enough' as they operate on larger bandwidths, however, Table 5.7 and Fig. 5.17 show that these filters do offer some improvement over the steered image. This is further evident in Table 5.8

Table 5.8) *Ratio of the largest sidelobe magnitude to that of the steered peak. The baseline ratio is a measure of the peak of the largest diffraction order to the steered peak. Ratios are measured from the "900-end" filter results.*

	Filter Bandwidth (nm)						
Data Bandwidth (nm)	800-900	750-900	700-900	650-900	600-900	500-900	Baseline
800-900	0.01	0.03	0.06	0.11	0.23	0.25	0.12
750-900	0.009	0.009	0.03	0.07	0.19	0.22	0.11
700-900	0.01	0.008	0.02	0.04	0.14	0.18	0.10
650-900	0.01	0.01	0.007	0.02	0.07	0.12	0.10
600-900	0.03	0.03	0.03	0.02	0.02	0.06	0.11
500-900	0.02	0.03	0.03	0.04	0.03	0.01	0.12

where the largest sidelobe-to-peak ratio is measured and compared to the baseline. Notice again how the smaller bandwidth filters give results which are better than the baseline over the entire range of bandwidths.

5.3 Broad-band Filter Robustness: Spectral Emission Dependence

Spectral robustness is tested in this section by creating steered and unsteered data in the 500-900 nm bandwidth and then weighting each of the computed wavelengths using a blackbody emission curve. An initial temperature range of 2250 - 3150 K is chosen about a center temperature of 2880 K which closely approximates the blackbody curve of the white light source used in the experiments reported at the beginning of this chapter. Eleven temperature curves were computed within this range at 90 K increments. This corresponds to a range in peak wavelength of 1.28 - 0.92 μm. The spectral emission characteristics of these curves give a relatively flat spectrum at 2250 K and a weighted spectrum for the longer wavelengths at 3150 K (Figure 5.19). Figure 5.20 shows how the diffraction orders change versus blackbody temperature. Filters are calculated for each weighted bandwidth and tested on the other weighted bandwidths. Each filter was found to give a result which is an improvement compared to each steered image. It was also discovered that

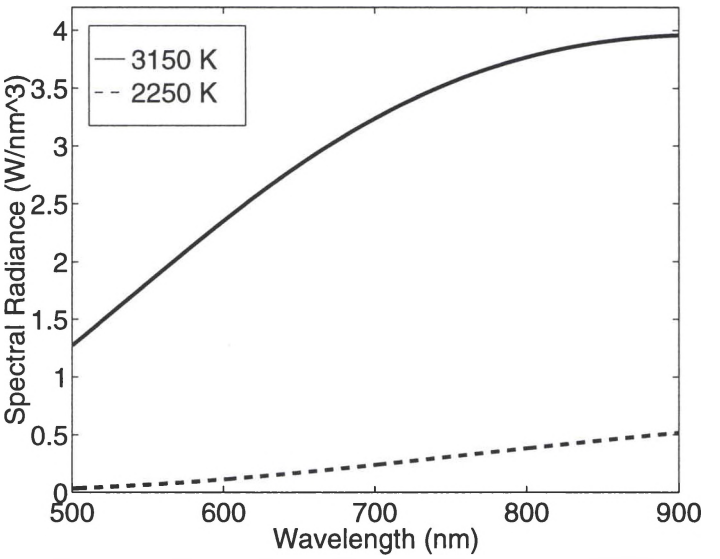

Figure 5.19) *Plot of the highest and lowest temperature blackbody curves used for weighting the 500-900 nm bandwidths.*

the filter estimates where all placed at the correct position of the desired, unsteered image due to the small range of temperatures examined. Filter results for the six temperatures examined Fig. 5.20 are given in Table 5.9. Notice that each filter will perform a significant degree of improvement as compared to the original, steered image. Excellent restoration ability is also shown in the largest sidelobe-to-peak ratios measured in Table 5.10. The largest sidelobe in the

Table 5.9) *Filter restoration (Improvement) measurements for the broad-band single slit image restorations of 500-900 nm bandwidth data weighted with variable blackbody curves. The data has an angular FWHM of 0.05°. The* Improvement Ratio *is a ratio of the baseline MSE to the MSE of the filter estimate. A value greater than one indicates improvement.*

	Filter Temperature K					
Data Temperature	2250 K	2430 K	2610 K	2790 K	2970 K	3150 K
2250 K	98.0	100.0	83.0	63.0	48.0	36.0
2430 K	59.0	135.0	134.0	107.0	79.0	57.0
2610 K	26.0	69.0	183.0	178.0	137.0	96.0
2790 K	14.0	28.0	82.0	247.0	234.0	171.0
2970 K	9.0	16.0	32.0	98.0	325.0	301.0
3150 K	7.0	10.0	18.0	37.0	117.0	416.0

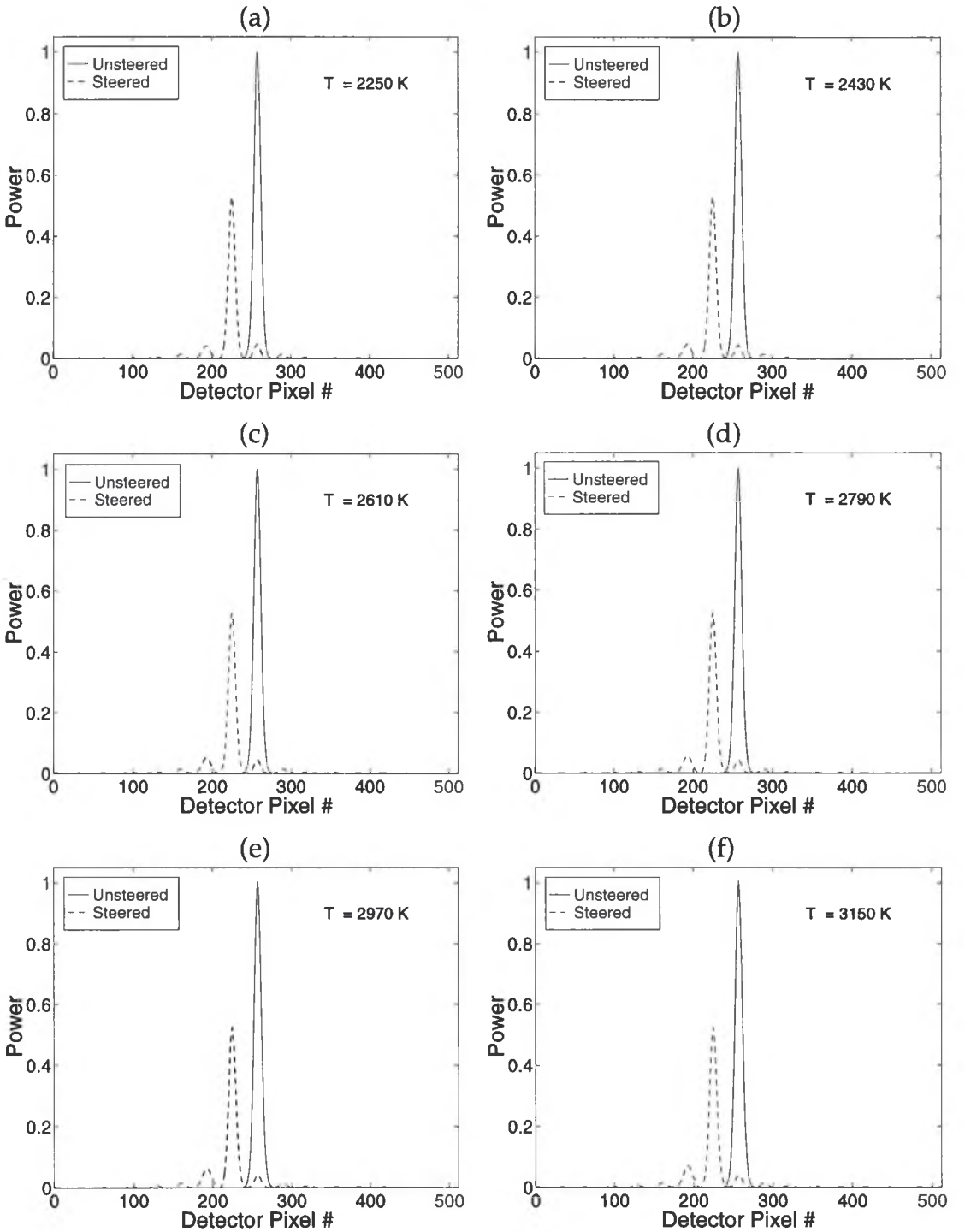

Figure 5.20) *Comparison of broad-band steered and unsteered 1-D single slits produced by BPM data weighted with a blackbody spectral emission curve with an angular FWHM of 0.05°. Results are shown for a bandwidth of 500-900 nm steered to 0.024°. Blackbody temperatures of (a) 2250 K, (b) 2430 K, (c) 2610 K, (d) 2790 K, (e) 2970 K, (f) 3150 K, are used to weight 40 evenly sampled wavelengths within the 500-900 nm bandwidth. The device design wavelength was 700 nm.*

Table 5.10) *Ratio of the largest sidelobe magnitude to that of the steered peak. The data has an angular FWHM of 0.05°. The baseline ratio is a measure of the peak of the largest diffraction order to the steered peak.*

	Filter Temperature K						
Data Temperature	2250 K	2430 K	2610 K	2790 K	2970 K	3150 K	Baseline
2250 K	0.003	0.004	0.006	0.008	0.01	0.011	0.087
2430 K	0.012	0.003	0.003	0.006	0.007	0.009	0.088
2610 K	0.023	0.012	0.003	0.003	0.005	0.006	0.10
2790 K	0.034	0.024	0.013	0.002	0.003	0.004	0.11
2970 K	0.046	0.035	0.024	0.013	0.003	0.0024	0.12
3150 K	0.057	0.047	0.036	0.024	0.013	0.003	0.13

steered image of *any* of the bandwidths is found to be reduced by *at least* a factor of two. This indicates that each filter performs some degree of improvement, even when filtering the 3150 K bandwidth data with the 2250 K filter and vice versa. To demonstrate the extent of improvement, filter restorations are shown in Figure 5.21 for the 2250 K and 3150 K steered data using the 3150 K and 2250 K

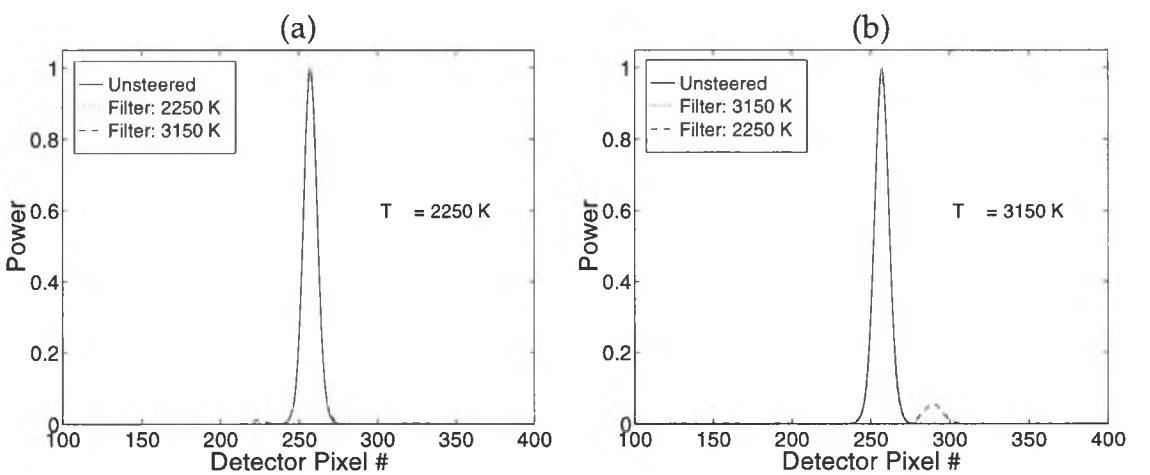

Figure 5.21) *Filter restorations using filter coefficients derived on data of bandwidth 500-900 nm with an angular FWHM of 0.05°. The data was weighted with a blackbody emission curve. The restoration in (a) is the result of using filter coefficients derived on 3150 K weighted data to restore 2250 K weighted data. The restoration in (b) is the result of using filter coefficients derived on 2250 K weighted data to restore 3150 K weighted data.*

filter coefficients, respectively. Notice the improvement compared to the steered results in Figure 5.20 in both the peak and sidelobe magnitudes.

Next we would like to repeat the blackbody emission robustness meaurements with steered (degraded) and unsteered (desired) with the spot size reduced to 0.001°. Steered and unsteered results at several of the various temperatures are presented in Figure 5.22. Filters are again calculated for each weighted bandwidth and tested on the other weighted bandwidths. Each filter was found to give a result which is an improvement compared to each steered, degraded image. The results are similar to those measured using the larger spot size data. Improvement ratios are given in Table 5.11. Notice the consistent restoration improvement as each filter is used to restore each of the other bandwidths regardless of spot size. Consistent improvement can also be seen by

Table 5.11) *Filter restoration (Improvement) measurements for the broad-band single slit image restorations of 500-900 nm bandwidth data weighted with variable blackbody curves. The data has an angular FWHM of 0.001°. The* Improvement Ratio *is a ratio of the baseline MSE to the MSE of the filter estimate. A value greater than one indicates improvement.*

	Filter Temperature K					
Data Temperature	2250 K	2430 K	2610 K	2790 K	2970 K	3150 K
2250 K	69000.0	112.0	30.0	14.0	7.0	5.0
2430 K	106.0	158000.0	152.0	41.0	16.0	9.0
2610 K	32.0	126.0	6160.0	221.0	44.0	19.0
2790 K	17.0	37.0	131.0	1010.0	218.0	52.0
2970 K	11.0	20.0	41.0	115.0	2014.0	253.0
3150 K	8.0	13.0	22.0	42.0	157.0	1911.0

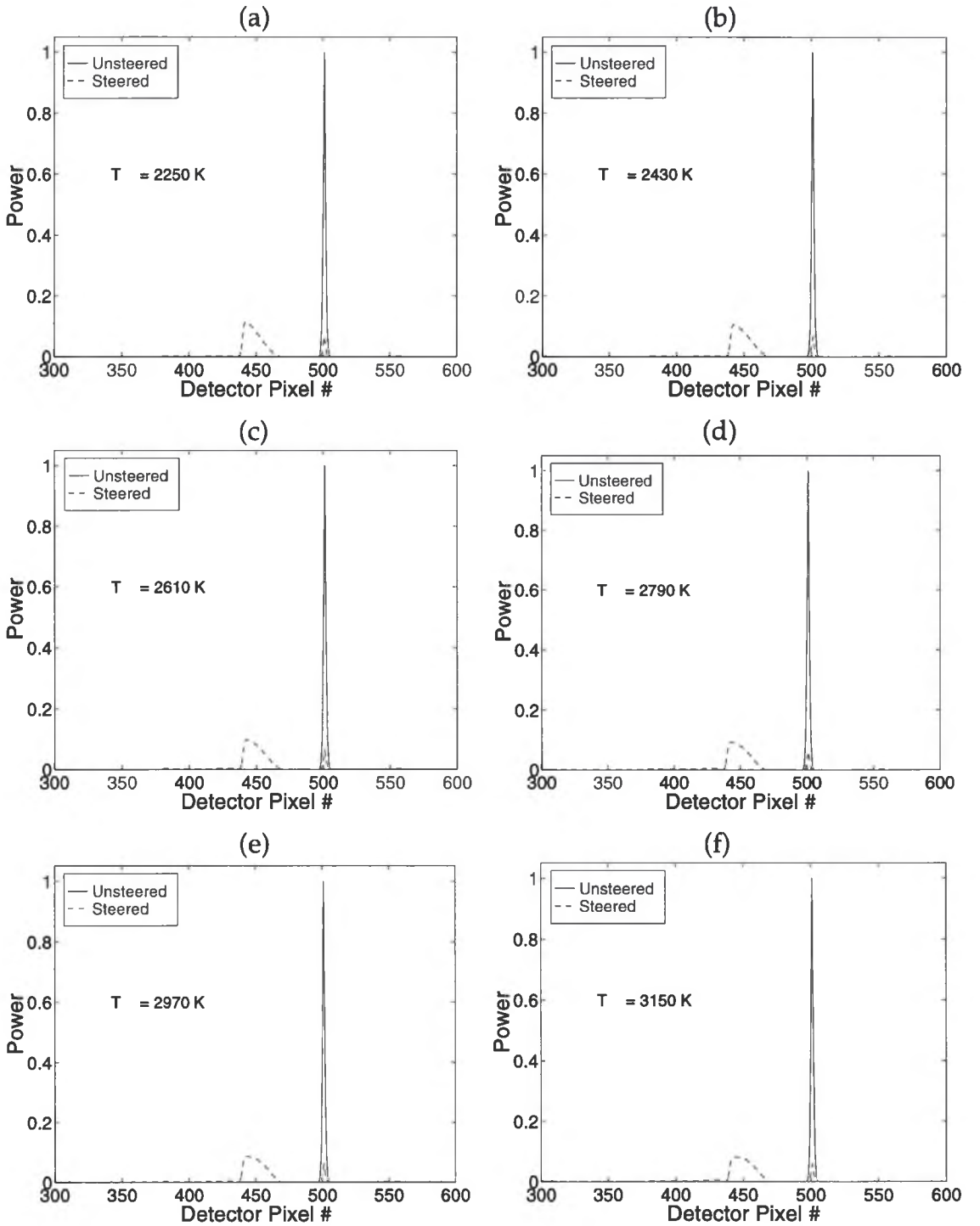

Figure 5.22) *Comparison of broad-band steered and unsteered 1-D single slits produced by BPM data weighted with a blackbody spectral emission curve with an angular FWHM of 0.001°. Results are shown for a bandwidth of 500-900 nm steered to 0.024°. Blackbody temperatures of (a) 2250 K, (b) 2430 K, (c) 2610 K, (d) 2790 K, (e) 2970 K, (f) 3150 K, are used to weight 401 evenly sampled wavelengths within the 500-900 nm bandwidth. The device design wavelength was 700 nm.*

examining the sidelobe to peak ratios of the filter restorations for each weighting temperature. These results are given in Table 5.12.

Table 5.12) *Ratio of the largest sidelobe magnitude to that of the steered peak. The data has an angular FWHM of 0.001°. The baseline ratio is a measure of the peak of the largest diffraction order to the steered peak.*

	Filter Temperature K						
Data Temperature	2250 K	2430 K	2610 K	2790 K	2970 K	3150 K	Baseline
2250 K	0.00064	0.017	0.032	0.044	0.060	0.073	0.57
2430 K	0.023	0.00006	0.014	0.027	0.042	0.056	0.62
2610 K	0.043	0.021	0.0028	0.012	0.026	0.039	0.61
2790 K	0.059	0.040	0.021	0.0076	0.012	0.024	0.67
2970 K	0.061	0.058	0.039	0.022	0.0044	0.012	0.66
3150 K	0.09	0.072	0.054	0.037	0.019	0.005	0.70

To demonstrate the extent of improvement, filter restorations are again shown for the extreme ends of the temperature range, 2250 K and 3150 K, restored using filter coefficients derived on the opposing steered data.

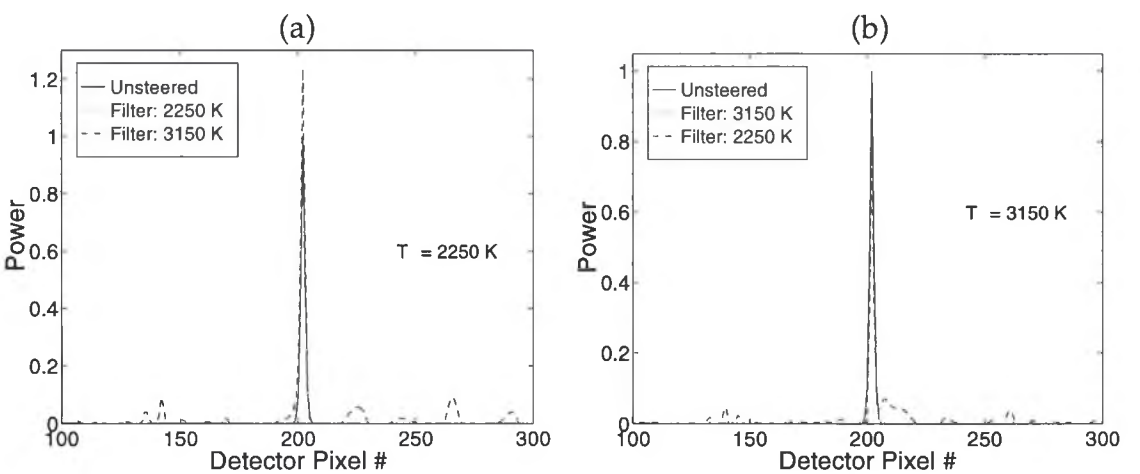

Figure 5.23) *Filter restorations using filter coefficients derived on data of bandwidth 500-900 nm with an angular FWHM of 0.001°. The data was weighted with a blackbody emission curve. The restoration in (a) is the result of using filter coefficients derived on 3150 K weighted data to restore 2250 K weighted data. The restoration in (b) is the result of using filter coefficients derived on 2250 K weighted data to restore 3150 K weighted data.*

5.4 Filter Generalizability

What will happen when a restoration filter is optimized with an impulse response measured in the lab and then applied to an image acquired in the real world? To test the generalizability of the image restoration filter images, both a single slit and a military bar target were illuminated with a broad-band (400–700 nm) white light source. Since the design wavelength was 543 nm, this pass band represents ≅ 20% bandwidth. An optimal filter was calculated from the steered

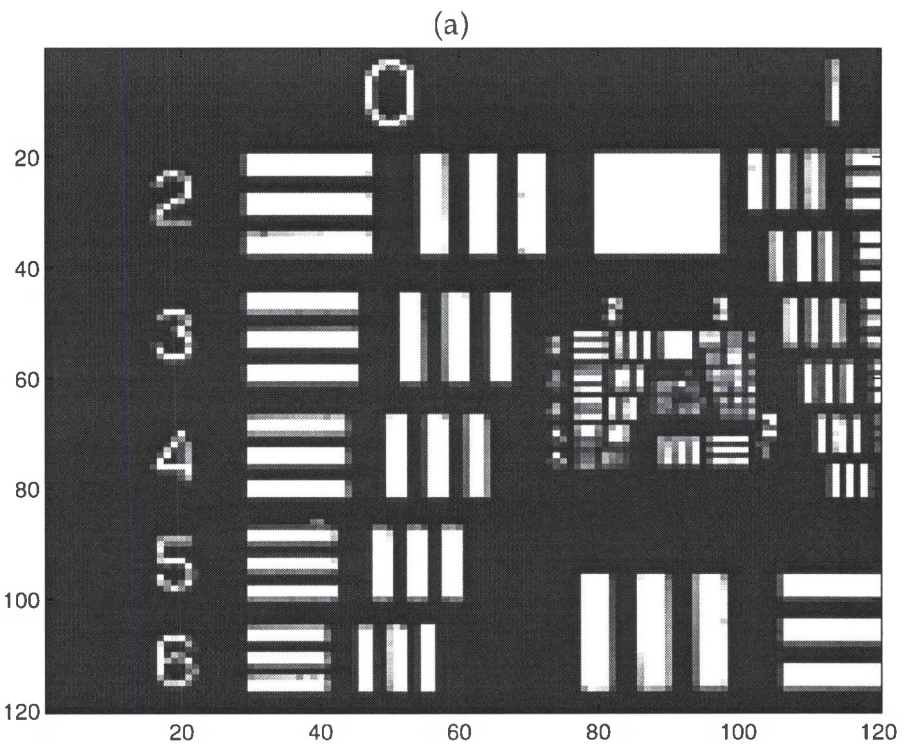

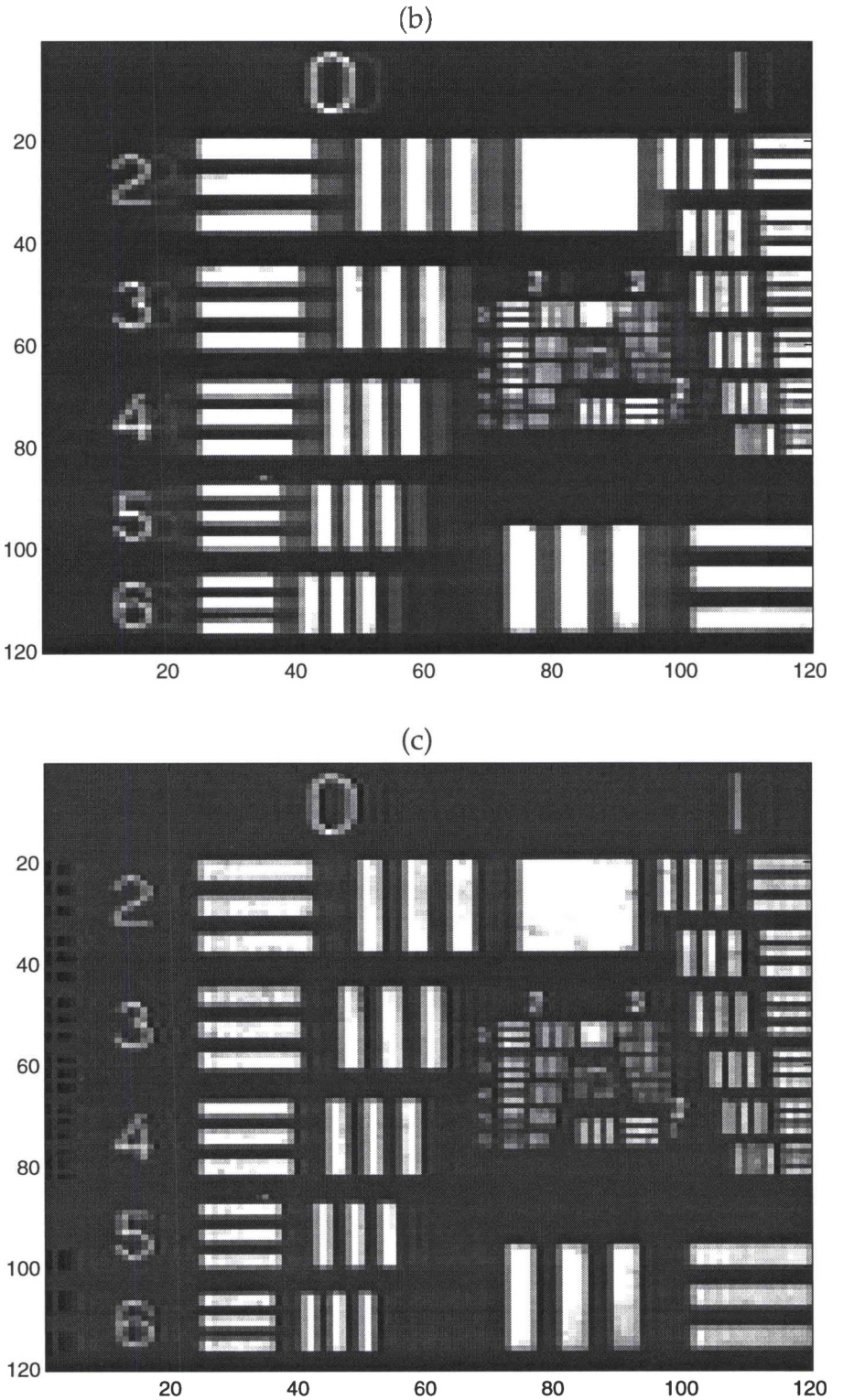

Figure 5.24) *(a) Unsteered, (b) steered, and (c) restored broad-band image of a military bar target. The restoration filter was derived from previously measured single slit images (not shown). The echoing seen in (b) is significantly reduced in (c).*

and unsteered images of the single slit and this filter was then applied to the steered image of a military bar target. The unsteered, steered, and restored image of the bar target are shown in Figure 5.24. By creating an optimal filter using an approximate impulse response, complicated images can be successfully restored with limited prior knowledge of the original scene. The importance of this discovery becomes obvious when considering the use of the liquid crystal steering device in a real world application, where it may be difficult to measure an impulse response in the field or calculate an optimal restoration filter for any given field of view.

As a final demonstration, a steered spoke target image was restored using *LMS* filter coefficients derived directly from steered and unsteered image data. Filter coefficients were calculated for two different spoke target images captured under the same conditions (one as in Fig. 5.26 and one with lower spoke density). The coefficients for each target were found to be nearly identical, thus presenting another example of filter generalizability. This indicates that an experimentally trained *LMS* filter should work well on data with the same spectral structure. A visual comparison of the two sets of filter coefficients is made in Figure 5.25. The unsteered, steered, and restored images of one spoke target are shown in Figure 5.26. The restored image represents a reduction in the *MSE* from 1.56×10^{-2} to 1.60×10^{-3}.

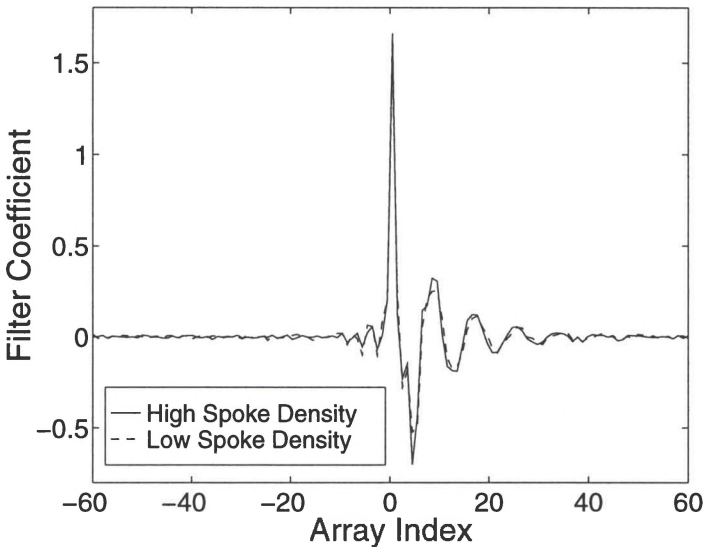

Figure 5.25) *Experimental LMS filter coefficients derived using two different spoke targets as training data. The high spoke density filter was derived using the steered and unsteered results in Figure 5.26. The low spoke density filter was derived using steered and unsteered results of a spoke target with one-half the number of spokes as that in Fig. 5.26.*

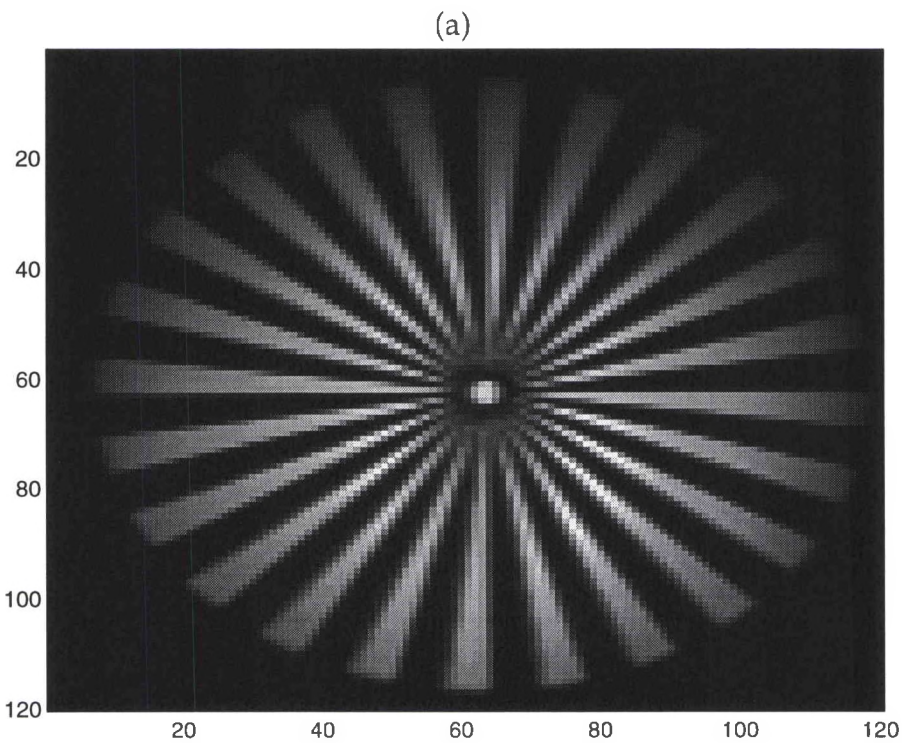

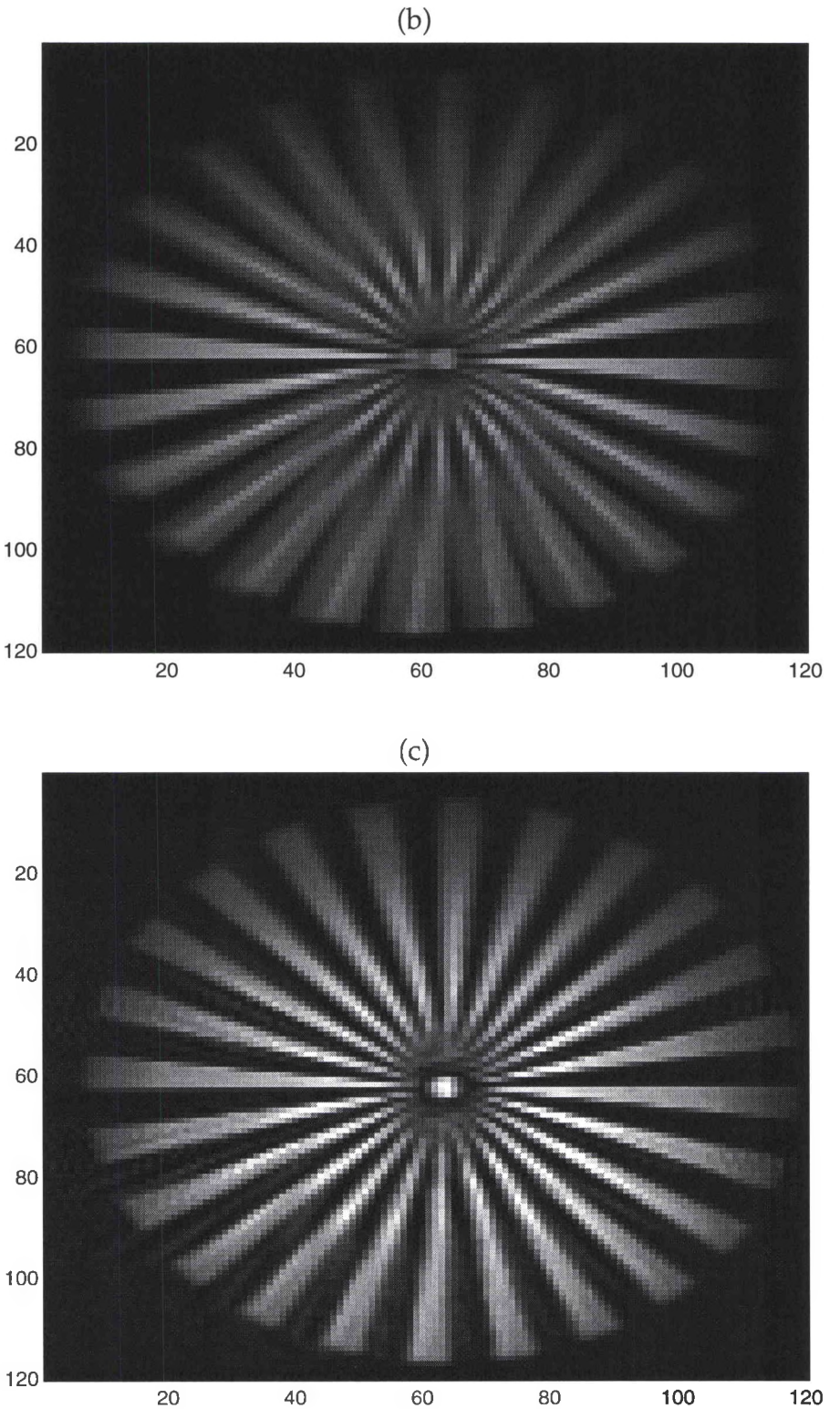

Figure 5.26) *(a) Unsteered, (b) steered, and (c) restored broad-band image of a spoke target. The restoration filter was derived solely from the LMS algorithm.*

5.5 Conclusion

This chapter demonstrates the image restoration ability of the *LMS* adaptive filtering algorithm on broad spectral band data. The filtering algorithm was found to effectively remove much of the material and grating dispersion introduced when steering a broad-band field of view with a liquid crystal beam steering device. Results show that *LMS* filter coefficients derived from experimental images can remove a large portion of the dispersion energy (smearing and echoing) introduced by the broad-band radiation. The filter estimates (restorations) were able to improve upon the original steered images by up to a factor of 10^3 in *MSE* as compared to the unsteered. The theoretical filter coefficients derived from the *BPM* model did not perform significant amounts of improvement, however, but did offer excellent starting points for the experimental *LMS* coefficients at small bandwidths and steer angles.

Broad-band filter robustness was tested using various bandwidths centered and de-centered about a device design wavelength. The results show that for broad-band data with an angular *FWHM* of 0.05°, filter estimates will only offer significant improvement to steered bandwidth data of up to two-times or down to one-half of the original filter bandwidth. For this reason it is best to choose a filter based on about one-half of the known bandwidth of the image so that the widest range of objects within the field of view can be successfully restored. For broad-band data with an angular *FWHM* of 0.001°, the filter coefficients are not

as robust and offer very little improvement with even a small (2-3%) change in bandwidth.

Robustness was also measured as a function of the spectral emission of the images. By modeling the BPM images as blackbody radiation sources, it was discovered that a filter can offer significant improvement on steered data weighted with a 40% difference in blackbody temperature, regardless of spot size.

The generalizability of the image restoration algorithm was also confirmed with filters derived from impulse-like images applied to bar targets. In the ideal case, Wiener filter coefficients derived from the BPM model can be computed which partially restore any image with the corresponding steer angle and wavelength (pass band). When experimental training data exists, further refinement of the filter coefficients is possible with the *LMS* algorithm. For an operational system, the *LMS* filter coefficients can be trained with impulse responses measured beforehand and then applied to newly acquired images. A new filter can be readily calculated with *BPM*, but knowledge of the spectral structure of the image is required. The spectral sensitivity of the restoration process is especially disturbing since the spectral characteristics of the imaged object may be unknown. Continued testing of broad-band filter generalizability will be necessary to determine the viability of these filtering algorithms in restoring real-world degraded images.

CHAPTER 6

Summary and Recommendations

The work performed in this thesis demonstrates the image restoration ability of the *BPM*, Wiener filter, and *LMS* filter algorithms on images degraded by the diffraction grating nature of a liquid crystal beam steering device. The *BPM* has proven to be an accurate predictor of liquid crystal cell response to incident radiation (Chapter 2), however, prediction accuracy is limited by the approximation to the phase profile of an actual device. Increased accuracy may be possible by using phase imaging techniques or other methods to precisely measure the phase profile of a real liquid crystal cell.

The Wiener filtering algorithm, which utilizes the response predicted by the *BPM*, has been used to derive filter coefficients which provide limited image restoration ability (Chapter 4). The sub-optimal performance of these filter coefficients is a result of both the inaccuracies in the BPM model and the approximation to the noise and signal statistics used in coefficient calculation (Equation 3.7). The restoration ability of the Wiener filter coefficients can likely

be improved by increasing the *BPM* model prediction accuracy and by measuring or modeling the actual noise and signal statistics in the images.

The *LMS* algorithm has been found to provide excellent restoration ability on the degraded images (Chapters 4 and 5). This algorithm, however, can only be utilized when a desired image is available so that filter coefficients can be trained using both the steered, degraded image and the desired image. We have demonstrated, however, that we can train the *LMS* filter coefficients on impulse response (slit-like) images and then accurately restore more visually complex images acquired under the same bandwidth and steer angle conditions.

Restoration of degraded narrow spectral band images has been accomplished with the filtering algorithms for a wide range of wavelengths and steer angles (Chapter 4). It was discovered that a different set of filter coefficients must be derived for each individual wavelength and steer angle due to the relative positions of the diffraction order echoes in the far-field. A change in wavelength as small as 5 nm or a change in steer angle as small as 0.001° will require an entirely new set of filter coefficients.

Restoration of degraded broad spectral band images has been accomplished with the *LMS* filtering algorithm for a wide range of bandwidths and steer angles (Chapter 5). Filter coefficients derived on broad-band data with an angular *FWHM* (of the unsteered beam) of 0.05° are shown to provide at least a small

degree of restoration when attempting to restore steered data of bandwidths other than those upon which the *LMS* filter was derived. When the angular *FWHM* of the unsteered beam is decreased to 0.001°, which is an approximate impulse response, it was found that the filter coefficients again worked well on the bandwidth upon which they were derived, but provided very little improvement for even a small change in bandwidth (2-3%). Restoration of degraded broad-band images of varying blackbody emission characteristics has also been accomplished with the *LMS* filtering algorithm for the range of blackbody temperatures(2250 - 3150 K). Over the range of blackbody temperatures examined each set of filter coefficients, derived from either the 0.05° or 0.001° angular *FWHM* data, was found to give at least a small degree of improvement for all other temperatures.

The ability of a set of filter coefficients derived from an experimental slit response to restore a more spatially complex image, or filter generalizability, was demonstrated and also presents an area which should be vigorously investigated in the future. Filter generalizability may provide a method for computing near-optimal filter coefficients for data taken in the field by modeling field conditions in the lab such as black-body emission characteristics and noise (turbulence). In future tests, it will also be important to test the restoration ability of the filtering algorithms in this thesis on images in which the spectral content varies across the spatial extent of the image. It will be possible to derive an optimal filter for a

given blackbody source but the question remains how well this filter will restore an image consisting of various random emission sources, such as those in a broad-band field of view. It may also be possible for the Air Force to fly with a beam steering device and a scanning mirror at the same time so that training data can be obtained. A steered image can be measured using the liquid crystal device and the scanning mirror can then be used to capture an unsteered image of the same field of view. This training data could then be used to develop the required filter coefficients.

The results obtained in this thesis demonstrate the ability of several image restoration algorithms to correct for the dispersion introduced by a liquid crystal beam steering device. The quality of image restoration makes it quite possible for an actual working beam steering system to be implemented by the Air Force for broad-band field of view steering. The biggest test will be the restoration of an image where the spectral content varies across the image. Continued advances in liquid crystal technology, such as the ferro-electric liquid crystals examined briefly in Appendix C, may eventually allow for the complete dismissal of gimbaled mirror systems.

APPENDIX A

```
% This MATLAB code is the main BPM function used to theoretically propagate a
% 1-D optical beam through a nematic liquid crystal beam steering device.
% The function call to DeltaN computes the wavelength dependent birefringence.
% The function call to Propagate computes the angular spectrum as it is
% propagated through a given slice.
% Author: Dr. Vince Dominic, University of Dayton.
%**********************************************
%**********************************  Steer *
%**********************************  Steer *
%**********************************************
function [AngOut,Spectrum] = Steer ( Thickness, ResetSpacing, NumofResets, DesignLambda,
ProbeLambda, BeamFWHM, Iflag )
% Steer - BPM model of the beamsteering device
% Inputs: Thickness, ResetSpacing, NumofResets, DesignLambda, ProbeLambda, BeamFWHM
%         (microns)  (microns)              (microns)   (microns)   (degrees)
% Output: AngOut, Spectrum
%****************************************

LambdaD = DesignLambda;          % Device design wavelength
LambdaP = ProbeLambda;           % Probe wavelength
DNSave  = DeltaN(LambdaD*1000);  % Birefringence due to design wavelength

% Xwindow = # of periods * period length = total number of phase steps
Xwindow = NumofResets*ResetSpacing;

delX    = ResetSpacing;          % Period length = # of steps per ramp

Slope   = LambdaD/(Thickness*delX)*DeltaN(LambdaP*1000)/DNSave;

%**********Wavelength dependent phase slope for a 4pi phase ramp *********
%-4pi  Slope   = 2*LambdaD/(Thickness*delX)*DeltaN(LambdaP*1000)/DNSave;
%*********************************************************************

if ( Iflag == 1 )   % If Iflag = 1 there is zero slope in the phase ramp: no steering
  Slope   = 0.;
end

Index0  = 1.7;                   % Average index of refraction
NX      = 512;                   % Number of points used to compute field
```

```
NZ     = 16;                          % Number of slices of LC cell
DZ     = Thickness / NZ;              % Thickness of each slice
coef   = 2*pi*Slope*DZ/LambdaP;
X2     = Xwindow/2;
k      = 2*pi*Index0/LambdaP;         % Magnitude of wave vector in Index0

AngIncr = 180/pi*acos(sqrt(1-(LambdaP/Xwindow)^2)); % Angular extent of each spatial point

Field  = (1+eps*i)*ones(1,NX);        % Initializing field as a complex array
Spectrum= Field;
AngOut  = linspace(-NX/2*AngIncr,(NX/2-1)*AngIncr,NX);
PosArg  = linspace(-X2,X2,NX) + X2;
fprintf(1,'Wavelength ..: %4.1f\n',1000*LambdaP);

% Calculation of Gassian beam over the angular FOV
Field = 0;
thet = -0.012;
while ( thet <= 0.012 )
  Field = Field + exp(-4*log(2)*(thet/BeamFWHM)^2).*exp(i.*k.*sin(thet*pi/180).*linspace(-
Xwindow/2,Xwindow/2,NX));
  thet = thet + 0.0005;
end

xx = rem(PosArg,delX);
 dnProfile = coef.*xx;  % Linear phase ramps

%*******Phase ramps altered from linear to best fit experimental data *******
%dnProfile = coef.*(xx+0.316*(2*((xx-delX/2).^8-(delX/2)^8)/(delX/2)^7));
%************************************************************************

% Propagation and Modulation processes performed on the complex field
Z      = 0;
while ( Z < Thickness )
  [Field,Z] = Propagate(Z,LambdaP,DZ,Index0,Xwindow,Field);  % PROPAGATION
   Field   = Field .*exp(-i.*dnProfile);                    % MODULATION
end

% Output beam as a result of the propagation and modulation processes
Spectrum=fftshift(fft(Field).*conj(fft(Field)))/(NX*NX);
```

```
% This function is uses FFT to propagate angular spectrum of optical wave
% ************************************ **********
% ************************************ **Propagate*
% ************************************ **Propagate*
% ************************************ **********
% Author: Dr. Vince Dominic, University of Dayton.

function [NField,newpos] = Propagate ( Z, LambdaP, DZ, Index0, Xwindow, Field )
%          Inputs:  Z, LambdaP, DZ, Index0, Xwindow, Field
%
%         Used in BPM algorithm.  See also Modulate and dn

NField = Field;
p     = 0:1:length(Field)-1;
ind    = min(p,(length(Field)-p));
arg    = pi*LambdaP*DZ/(Index0*Xwindow*Xwindow);

% Output:  new angular spectrum at the position of the next slice
NField = ifft(fft(Field).*exp(i.*(arg.*ind.*ind)));
newpos = Z+DZ;            % spatial position of next slice in the cell
```

```
% This function computes the dispersion of the birefringence for E7.
% ************************************ **********
% ************************************ *** DeltaN *
% ************************************ *** DeltaN *
% ************************************ **********
% Author: Dr. Vince Dominic, University of Dayton.

function DN = DeltaN ( lam )
% returns:  DN = dispersion
% takes:    lam = wavelength in nm

G=3.06e-6;        % Constants computed specifically for E7 liquid crystal material
lam0 = 250;       %

% Output:  probe wavelength dependent birefringence
DN = G*lam0*lam0.*lam.*lam/(lam.*lam-lam0*lam0);
```

```
% This function uses superimposed narrowband results calculated by the BPM
% to predict a broadband response. The steered and unsteered spectrum computed
% for each wavelength are then interpolated so that each spectrum extends over
% the same angular FOV.
% Authors: Dr. Vince Dominic and Ron Broessel, University of Dayton
num=1001;
NumOfLams = 401;       % Number of wavelengths to be added together
steer  =zeros(NumOfLams,num);
unsteer=zeros(NumOfLams,num);


for i=1:NumOfLams

 Lambda    = 0.5+(i-1)*0.4/(NumOfLams-1);  % wavelength
 AngOut    = 0*linspace(1,num,num);
 d         = 80*16; % Spatial extent of phase ramp = # of electrodes *
                    % electrode width
 fwhm      = 0.001; % Angular FWHM of each narrowband wavelength
 AngIncr   = 180/pi*Lambda/(32*d);
 Spectrum  = AngOut;
 [AngOut,Spectrum] = Steer(5,d,32,0.7,Lambda,fwhm,1);
 UnSteered = Spectrum;
 [AngOut,Spectrum] = Steer(5,d,32,0.7,Lambda,fwhm,0);
 Steered   = Spectrum;

 AngBeg         =-0.33;  % Angular extent of new, interpolated field
 AngEnd         = 0.33;
 AngIncr        = AngOut(2) - AngOut(1); % Angular increment in original field

 Steered(length(Steered)+1)=Steered(1); % Making the Steered image symetric (odd)

 UnSteered(length(UnSteered)+1)=UnSteered(1); % Making the Unsteered image
                                              % symetric (odd)

 AngOut(length(AngOut)+1) = abs(AngOut(1)); % Making the original angle array
                                            % symetric (odd)

 NewSize=2*floor(AngEnd/AngIncr)+3;  % Size of new field to be interpolated to

 % Starting position of original steered or unsteered in zero padded array
 BegPos=(NewSize-1)/2 - (length(Steered)-1)/2+1;   %which is to be interpolated

 NewSArr=zeros(1,NewSize);

 % Placing steered original into new zero padded array
 NewSArr(BegPos:(BegPos+length(Steered)-1))=Steered;

 NewUArr=zeros(1,NewSize);

 % Placing unsteered original into new zero padded array
 NewUArr(BegPos:(BegPos+length(UnSteered)-1))=UnSteered;
```

```
 % New Angular extent of zero padded steered and unsteered
 NewTheta = linspace(-(NewSize-1)/2*AngIncr,(NewSize-1)/2*AngIncr,NewSize);

 NewAng = linspace(AngBeg,AngEnd,num);  % Interpolated (new) angular extent

 NewSteer = interp1(NewTheta,NewSArr,NewAng)';  % Interpolated Steered result
 NewUn    = interp1(NewTheta,NewUArr,NewAng)';  % Interpolated Unsteered result

 steer(i,:)   = (NewSteer)/max(NewUn);
 unsteer(i,:) = (NewUn)/max(NewUn);
end

st_result=zeros(1,num);
unst_result=zeros(1,num);
for i=1:NumOfLams
        st_result=st_result + steer(i,:);
        unst_result=unst_result + unsteer(i,:);
end

des=unst_result;  % 1-D superposition of unsteered result
obs=st_result;    % 1-D superposition of steered result
```

APPENDIX B

```
% This function calculates the optimal restoration coefficients
% from a degraded and desired image.
% Author: Dr. Russell Hardie, University of Dayton.
function [w,mse,pass] = lms_simple(des,obs,ws,ss,pass,w)
%     [w,mse] = lms_create(des,obs,ws,ss,pass,w)
%
%     find optimal linear filter using lms method
%
%     des    - desired signal
%     obs    - observed signal
%     ws     - window size
%     ss     - step size
%     pass   - number of passes, optional, default=1
%     w      - starting weight matrix, optional

mse=zeros(1,pass);

mid=(ws-1)/2;
ul=length(obs)-mid;
est=des;            % Insure that the estimate is the same size
                    % as the observed and desired images.

%*************START OF FILTER CALCULATION*****************************
for m=0:pass-1,
  for n=1+mid:ul
    endp=n+mid;                    % End position of observation window
    beg=n-mid;             % Start position of obs. window
    est(n)=obs(beg:endp)*w';       % Multiplying the observed image by
                                   % latest set of filter coeffs, w.
    w=w+ss*obs(beg:endp)*(des(n)-est(n)); % Updating the filter coeffs
  end

  %***********Error Calculation*****************
   diff=abs(des-est);
   error=(diff).*(diff);
   mse(m+1)=sum(error)/(length(des)); % Mean Squared Error.)
```

```
   fprintf(1,'%3d  %e\n',m,mse(m+1));
   diff=0.;
   error=0.;
  %**********End of Error Calculation**********

  ss=ss/1.;                % Decrease the step size each pass.
end
%************End of Filter Calculation*********************************
```

```
% This function applies the calculated optimal filter coeffs
% to the input degraded image.
% Author:  Dr. Russell Hardie, University of Dayton

function [est] = lms_filt(noisy,w)
% [est] = lmsf(noisy,w)
%
%      noisy - input degraded signal
%      w     - optimal weight vector
%
%      est   - lms filter estimate


N=length(w);
est=noisy;
r=(N-1)/2;
ul=length(noisy)-r;

      for n=1+r:ul,
            est(n)=noisy(n-r:n+r)*w';
      end
```

```
% This function calculates the Weiner Filter impulse response
% from a system impulse response.
% Author: Ron Broessel, University of Dayton, WPAFB.
function [w] = wiener(imp_res,th,gamma,winsize)
%
%      [w] = wiener(imp_res,th,gamma,winsize)
%
%      This function creates a Wiener filter from an input I.R.
%
%      w       - output, initial estimate for filter coeffs
%        winsize  -  pre-determined number (length) of filter coeffs
%      gamma    -  Wiener filter offset constant, noise/signal ratio
%        th      -  Pseudo inverse filter threshold
%        steered  -  Steered image data, the impulse response
%
%      Written 2-27-95 RJB.
%***************************************************************

n=length(imp_res);
imp=fliplr(imp_res);

%**********Inverse Filtering*********************************

impfft=fft(imp,winsize);% FFT of impulse response

H=zeros(1,winsize);                % Initializing filter coeffs

ratio=0.;
ratio2=0.;

%********Calculation of Wiener filter coefficients*****************
for i=1:winsize
 ratio = impfft(i);          % Normal Inverse Filter
 ratio2 = (ratio)*conj(ratio);
 if abs(ratio) < th  H(i)=0.;end;
 if abs(ratio) >= th  H(i)=((1/ratio)*((ratio2)/(ratio2+gamma)));end;
end
%***************************************************************

h=ifft(H);                         % IFFT to obtain spatial
                                   % domain filter coeffs

w=real(h);                 % Filter Coeffs in spatial domain
%***************************************************************
```

APPENDIX C

This appendix presents a short discussion concerning an alternative to the nematic liquid crystal (*NLC*) phase-shifting material presently used in non-mechanical beam steering devices: ferro-electric liquid crystals (*FLC*).[26-28] *FLC*-controlled phase modulators promise to give much faster switching speeds than the current generation of nematic devices: 10's of microseconds for *FLC*'s compared to 10's of milliseconds for nematics.[26-27] The design of a *FLC*-controlled phase modulator[28] utilizes two fixed, achromatic quarter-wave plates (*Q*) and a *FLC* half-wave plate (*H*) in the sequence *QHQ*. The phase introduced by such a modulator is essentially independent of wavelength and this offers several advantages over nematic-based modulators. One important advantage of a *FLC* phase-shifting cell is the improved fidelity of broad-band field of view steering due to the elimination of diffraction-grating echoing and material-dispersion induced smearing in the acquired images. Unfortunately, the broad band images will still be degraded by diffraction grating smearing since the steering angle will vary linearly with the wavelength for any periodic structure. However, since

two of the three image degradation mechanisms specific to *NLC* devices are eliminated, the restoration algorithms discussed in this thesis are expected to be simpler to implement and will probably be more robust in the *FLC*.

The difference between the two liquid crystal materials lies in the methods of phase shifting from one cell to the next. The phase introduced by one *NLC* cell differs from the next by a change in retardance (refractive index) that is experienced by an optical beam traversing the cells. In a *FLC* cell, the retardance remains constant for each cell but the orientation of the optical axes are electrically controllable and so vary from one cell to the next. One can show by simple Jone's calculus that controlling the orientation of the half-wave plate in a *QHQ* stack controls the phase shift introduced by the modulator cells.[28]

To demonstrate the effect of this type of liquid crystal cell, we use the *BPM* to calculate a steered broad-band response through a *FLC* device. It is assumed that the cell width, cell spacing, and number of cells remain the same as that of the *NLC* device. The modeled *FLC* device doesn't currently exist, however, we can readily demonstrate the behavior of such a device to show the differences between it and the *NLC* device. Figure A1(a) shows the steered broad-band (500-900 nm, flat-topped spectral profile) image of a narrow single slit of angular *FWHM* of 0.001°. Part (b) of the figure gives the steered image utilizing a *NLC* structure for comparison. Notice that the diffraction order echoes present in the *NLC* steered image are not present in the steered result for the *FLC* device,

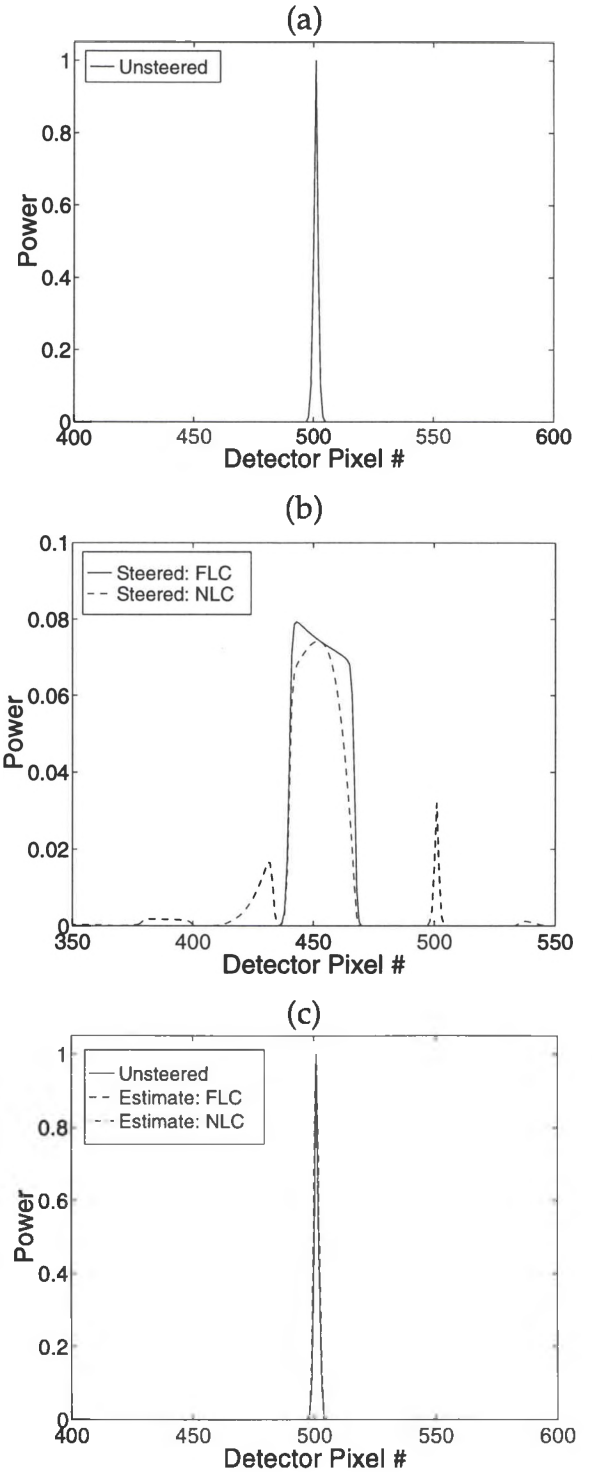

Figure A1) *(a) Unsteered 500-900 nm bandwidth, flat spectrum of FWHM = 0.001°. Steered bandwidth prediction for a (b) ferro-electric liquid crystal beam steering device and a nematic liquid crystal beam steering device. (c) Restoration of each steered prediction using optimal LMS coefficients trained on the predicted data.*

however, smearing due to the grating dispersion remains. If optimal *LMS* filter coefficients are derived for both steered results we can see that excellent restoration is attainable Fig. A1(c). It is obvious from the figure that a ferro-electric liquid crystal device would provide an improved way to steer a broad-band field of view not only be eliminating material dispersion smearing and grating order echoing but will also greatly reduce switching speeds. Further examination of this type of liquid crystal will be important to determine its viability as a non-mechanical beam steering medium.

BIBLIOGRAPHY

1. P. F. McManamon, E. A. Watson, T. A. Dorschner, and L. J. Barnes, "Applications look at the use of liquid crystal writable gratings for steering passive radiation," *Opt. Eng.* **32** (11), 2657-2664 (1993).

2. E. A. Watson, P. F. McManamon, L. J. Barnes and A. Carney, "Application of Dynamic Gratings to Broad Spectral Band Beam Steering," *Proc. of the SPIE* **2120**, 178-185 (1994).

3. P. F. McManamon, E. A. Watson, T. A. Dorschner, and L. J. Barnes, "Nonmechanical Beam Steering for Active and Passive Sensors," *Proc. of the SPIE* **1969**, 2-10 (1993).

4. K. J. Barnard, E. A. Watson, and P. F. McManamon, "Nonmechanical microscanning using optical space-fed phased arrays," *Opt. Eng.* **33** (9), 3063-3071 (1994).

5 E.A. Watson, L.J. Barnes, "Optical Design Considerations for Agile Beam Steering," *Proc. of the SPIE* **2120**, 186-193 (1994).

6 R.M. Matic, "Blazed Phase Liquid Crystal Beam Steering," *Proc. of the* SPIE **2120**, 194-205 (1994).

7 T.A. Dorscher, R.C. Sharp, D.P. Resler, L.J. Friedman, D.C. Hobbs, R.L. Chandler, and A. Legere, Basic Laser Beam Agility Techniques (BATS), final report by Raytheon Co., prepared for Wright Laboratory, WL-TR-93-1020 (1993).

8. T. C. Cheston and J. Frank, "Phased Array Radar Antennas," Chapt. 7 in *Radar Handbook*, M.I. Skolnik, ed., McGraw-Hill, New York, (1990).

9 S.T. Wu, U. Efron, and L.D. Hess, "Birefringence Measurements of Liquid Crystals," *Applied Optics*, **23** (21), 3911-3915 (1 November 1984).

10. S.-T. Wu, "Birefringence Dispersions of Liquid Crystals," *Phys. Rev. A* **33** (2), 1270-1274 (1986).

11 E. Jakeman and E.P. Raynes, "Electro-Optic Response Times in Liquid Crystals," *Physics Letters* **31A** (1), 69-70 (10 April 1972).

12. J. Goodman, *Fourier Optics*, McGraw-Hill, Inc., San Francisco, 30-74, (1968).

13 M. Born and E. Wolf, *Principles of Optics*, Pergamon Press, New York, Chapter 8, (1959).

14. A. K. Jain, *Fundamentals of Digital Image Processing*, Prentice Hall Inc., Englewood Cliffs, New Jersey, pp. 267-284, (1989).

15. B. Widrow and S. D. Stearns, *Adaptive Signal Processing*, Prentice Hall Inc., Englewood Cliffs, New Jersey, pp. 99-114, (1985)

16. M. D. Feit and J. A. Fleck, Jr., "Light Propagation in Graded-Index Optical Fibers," *Appl. Opt.* **17** (24), 3990 - 3998 (15 Dec. 1978).

17. J. A. Fleck, J. R. Morris, and M. D. Feit, "Time-dependent Propagation of High Energy Laser Beams Through the Atmosphere," *Appl. Phys.* **10** , 129 - 160 (1976).

18. R. Johnson and A. R. Tanguay, Jr., "Optical Beam Propagation Method for Birefringent Phase Grating Diffraction," *Opt. Eng.* **25** (2), 235 - 249 (1986).

19 D. Yevick and L. Thylen, "Analysis of Grating by the Beam-Propagation Method," *J.O.S.A.* **72** (8), 1084-1089.

20 J. E. Stockley, G. D. Sharp, D. Doroski, and K. M. Johnson, "High-speed Analog Achromatic Intensity Modulator," *Optics Letters* **19** (10), 758-760 (1994).

21 V. Dominic, A. Carney, and E. A. Watson, unpublished.

22. S. J. Orfanidis, *Optimum Signal Processing: An Introduction*, Macmillan Publishing Co., New York, pp. 278-324, (1985).

23. B. Widrow, J. M. McCool, M. G. Larimore, and C. R. Johnson, Jr, "Stationary and Nonstationary Learning Characteristics of the *LMS* Adaptive Filter," *Proc. of the IEEE* **64** (8), 1151-1162 (Aug 1976).

24 B. Widrow and J.M. McCool, "A Comparison of Adaptive Algorithms Based on the Methods of Steepest Descent and Random Search," *IEEE Trans. on Antennas and Propagation* **AP-24** (5), 615-637 (1976).

25 G.A. Clark, S.K. Mitra, and S.R. Parker, "Block Implementation of Adaptive Digital Filters," *IEEE Trans. on Circuits and Systems* **CAS-28** (6), 584-592 (1981).

26 G. D. Sharp and K. M. Johnson, "High-speed Analog Complex-amplitude Liquid Crystal Light Modulator," *Optics Letters* **19** (16), 1228-1230 (1994).

27 J. E. Stockley, G. D. Sharp, D. Doroski, and K. M. Johnson, "High-speed Analog Achromatic Intensity Modulator," *Optics Letters* **19** (10), 758-760 (1994).

28 G. D. Sharp, *Ph.D.* Dissertation, University of Colorado, Boulder CO.